LUMINESCENCE-BASED CHARACTERIZATION OF CRYSTALLINE SILICON SOLAR CELLS

Von der Fakultät für Mathematik und Physik
der Gottfried Wilhelm Leibniz Universität Hannover
zur Erlangung des Grades
Doktor der Naturwissenschaften
Dr. rer. nat.
genehmigte Dissertation
von

Dipl.-Phys. David Hinken
geboren am 27.11.1981 in Hannover

2012

Referent:	Prof. Dr. Rolf Brendel
Korreferent:	Prof. Dr. Jörg Osten
Tag der Promotion:	03.05.2012

Abstract

Camera-based luminescence imaging for the characterization of silicon solar cells was introduced into photovoltaics in 2005 by a Japanese research group. For this characterization technique, excess charge carriers in the solar cell bulk are either injected using a current source or optically generated by illumination. Luminescence imaging is fast and the resulting images contain abundant information about the solar cell device because the detected luminescence signal depends on properties like the charge carrier recombination, the optical confinement as well as on the series- and shunt resistance. However, at that time, measured luminescence images were interpreted qualitatively only and it was not demonstrated, how luminescence imaging can be used to extract quantitative images of a specific solar cell parameter. Therefore, this thesis presents a comprehensive description and understanding of luminescence images of wafer-based crystalline silicon solar cells. It aims at the determination of local solar cell parameters and its relation to the global solar cell energy conversion efficiency.

Luminescence photons are generated inside the solar cell by radiative recombination of excess charge carriers. Since this process is directly related to the minority charge carrier density, the absorption of illuminating photons and the injection of minority charge carriers is explicitly analyzed in this thesis. Due to reabsorption of luminescence photons inside the solar cell, the photon emission probability depends on its depth of generation. Consequently, not only the minority charge carrier density is required but also its distribution inside the solar cell. Various distributions for different solar-cell working points are explicitely modeled in this work by analyzing the minority charge carrier diffusion inside the solar cell base.

The luminescence photons, generated within the solar cell, need to be emitted from the solar cell surface to finally be counted within the camera. To describe this emission process an optical model is required. This thesis shows that the description of the emission of photons is directly related to the reverse process, the absorption of photons. Thus, previously developed models for the absorption of photons can be used for luminescence imaging. As a result, the optical resolution of luminescence imaging is calculated.

The electrical and optical modelling yields analytical equations for the detected luminescence emission of the solar cell. The derived equations reveal explicitly the dependence of the emitted luminescence spectrum on certain electrical and optical solar cell properties. Luminescence emission spectra are analyzed for different working points and are compared to experiment.

This thesis calculates the impact of local parameters on the global energy conversion efficiency. Therefore, the solar cell is split into many small local elements, whereas each local element is described with the electrical and optical modelling of the previous chapters. The local elements are then interconnected using equivalent circuit models. Thus, local parameters are related to meaningful global properties like the energy conversion efficiency. As a possible application of this analysis a local impact analysis is presented, which determines the impact of increased local series resistances onto the global energy conversion efficiency.

Keywords: Solar cell characterization, luminescence imaging, two-dimensional equivalent circuits

Kurzzusammenfassung

Kamerabasierte Lumineszenzmessungen für die Charakterisierung von Silizium-Solarzellen wurden im Jahr 2005 von einer japanischen Forschungsgruppe vorgestellt. Für diese Charakterisierungsmethode werden Überschussladungsträger in der Solarzelle entweder elektrisch mittels einer Strom-Spannungs-Quelle injiziert oder optisch durch Beleuchtung erzeugt. Die Messdauer für die Aufnahme eines Lumineszenzbildes ist sehr kurz. Das Ergebnis sind Bilddaten, welche eine Vielzahl an Informationen über die Solarzelle enthalten. Das gemessen Lumineszenzsignal wird nämlich neben den Rekombinationseigenschaften der Ladungsträger und optischen Eigenschaften auch von Serien- und Shuntwiderständen der Solarzelle bestimmt. Trotzdem wurden anfangs die Bilddaten nur qualitativ interpretiert. Es war noch nicht vollständig verstanden, wie die kamerabasierte Lumineszenz genutzt werden kann, um quantitative Informationen über einen bestimmten Parameter der Solarzelle zu erhalten.

Lumineszenz-Photonen werden in der Solarzelle durch die strahlende Rekombination von Überschussladungsträgern erzeugt. Da dieser Prozess direkt mit der Überschussladungsträgerdichte zusammenhängt, wird die Absorption von Photonen der Beleuchtung bzw. die Injektion von Minoritätsladungsträgern in dieser Arbeit untersucht. Aufgrund von Reabsorption der Lumineszenzphotonen innerhalb der Solarzelle ist die Emissionswahrscheinlichkeit der erzeugten Photonen von dem Ort abhängig, an dem sie erzeugt wurden. Folglich ist nicht nur die überschussladungsträgerdichte wichtig, sondern auch ihre Verteilung innerhalb der Solarzelle. In dieser Arbeit modelliere ich verschiedene Verteilungen für unterschiedliche Arbeitspunkte der Solarzelle mittels der Ladungsträgerdiffusionsgleichung.

Die Lumineszenz-Photonen, welche innerhalb der Solarzelle erzeugt werden, müssen aus der Solarzelle austreten, um von der Kamera detektiert werden zu können. Zur Beschreibung dieses Emissions-Prozesses ist ein optisches Modell der Solarzelle notwendig. Es wird in dieser Arbeit gezeigt, dass die Beschreibung der Photonen-Emission direkt invers zum reziproken Prozess der Absorption von Photonen ist. Damit können weit fortgeschrittene Modelle für die Absorption von Photonen auch für die Lumineszenzemission genutzt werden. Als ein Ergebnis dieser optischen Modellierung bestimme ich die optische Auflösung von Lumineszenzbildern.

Die elektrische und optische Modellierung liefert analytische Gleichungen für die detektierte Lumineszenzemission der Solarzelle. Diese Gleichungen zeigen explizit die Abhängigkeiten des emittierte Lumineszenz-Spektrum auf bestimmte elektrische und optische Parameter der Solarzelle. Lumineszenz-Spektren werden an unterschiedlichen Arbeitspunkten der Solarzelle analysiert und mit Experimenten verglichen.

Im letzten Teil dieser Arbeit wird gezeigt, wie der Einfluss lokaler Parameter auf den Gesamt-Wirkungsgrad der Solarzelle berechnet werden kann. Dafür wird die Solarzelle in viele kleine Elemente aufgeteilt, wobei jedes lokale Element mit den elektrischen und optischen Modellen der vorherigen Kapitel beschrieben wird. Dadurch werden die lokalen Parameter mit aussagekräftigen globalen Parametern wie dem Gesamt-Wirkungsgrad der Solarzelle verknüpft. Als eine mögliche Anwendung dieser Analyse wird der Einfluss des lokalen Serienwiderstandes auf den Gesamt-Wirkungsgrad demonstriert.

Schlagwörter: Charakterisierung von Solarzellen, ortsaufgelöste Lumineszenz, zweidimensionale Ersatzschaltbilder

Contents

1 Introduction **1**
- 1.1 Short review of luminescence imaging . . . 1
- 1.2 Short overview of this thesis . . . 2

2 Camera-based setup for luminescence measurements **5**
- 2.1 Detailed setup description . . . 5
  - 2.1.1 Housing . . . 6
  - 2.1.2 Sample mounting and contacting . . . 6
  - 2.1.3 Electrical and optical stimulation of luminescence . . . 7
  - 2.1.4 Camera . . . 7
  - 2.1.5 Filters . . . 10
- 2.2 Data acquisition process of luminescence imaging . . . 12
- 2.3 Exemplary luminescence images . . . 14
  - 2.3.1 Silicon solar cells . . . 14
  - 2.3.2 Silicon wafers . . . 14
- 2.4 Camera noise analysis . . . 17
  - 2.4.1 Different noise sources of luminescence measurements . . . 17
  - 2.4.2 Noise modeling . . . 18
  - 2.4.3 Calculations and measurements . . . 19
- 2.5 Short summary . . . 22

3 Physical background of luminescence photon generation and emission **23**
- 3.1 Detection geometry . . . 23
- 3.2 Luminescence photon generation inside the solar cell . . . 25
  - 3.2.1 Radiative recombination . . . 25
  - 3.2.2 Spectral coefficient of radiative recombination . . . 27
  - 3.2.3 Integral coefficient of radiative recombination . . . 27
  - 3.2.4 Coulomb enhancement of the coefficient of radiative recombination . . . 29
- 3.3 Luminescence photon emission from the solar cell surface . . . 30
- 3.4 Solar cell structure analyzed in this work . . . 30
- 3.5 Camera signal . . . 31
- 3.6 Solving the luminescence integral . . . 32

4 Charge carrier distributions within the solar cell base **33**

4.1 Diffusion equation of charge carriers . . . 33
4.1.1 Three dimensions . . . 33
4.1.2 One dimension . . . 34
4.2 Boundary conditions of the diffusion equation . . . 35
4.2.1 Photoluminescence at open-circuit conditions . . . 36
4.3 Generation profile of charge carriers for optical excitation . . . 38
4.3.1 Literature solution . . . 38
4.3.2 Simplification of the generation profile for the used experimental setup 40
4.4 Solutions for the diffusion equation . . . 41
4.4.1 Electroluminescence . . . 41
4.4.2 Photoluminescence at short-circuit conditions . . . 41
4.4.3 Photoluminescence at working-point conditions . . . 42
4.4.4 Photoluminescence at open-circuit conditions . . . 42
4.4.5 Transformation PL-oc to PL-sc . . . 42
4.5 Calculations and simulations of charge carrier distributions . . . 43
4.5.1 Simulation of charge carrier distributions . . . 43
4.5.2 Comparison of PL-oc and PL-sc to numerical device simulator . . . 44
4.6 Short summary . . . 46

5 Luminescence photon emission probability **47**
5.1 Deriving the luminescence photon emission probability . . . 47
5.1.1 Detection geometry . . . 47
5.1.2 Summation of all involved volumes . . . 48
5.1.3 Conservation of Etendue . . . 49
5.1.4 One-dimensional luminescence photon emission probability . . . 50
5.2 Transmittances . . . 50
5.2.1 Reversibility of light rays . . . 51
5.2.2 Equality of transmittances . . . 51
5.3 Relating the emission probability to the generation profile . . . 53
5.3.1 Research context of the result . . . 54
5.4 Resulting one-dimensional emission probability . . . 56
5.5 Optical lateral resolution of luminescence imaging . . . 58
5.6 Short summary . . . 59

6 Spectral and integral analysis of the luminescence emission **61**
6.1 Luminescence emission integral . . . 61
6.2 Excess charge carrier distributions . . . 62
6.2.1 Electroluminescence . . . 62
6.2.2 Photoluminescence at short-circuit conditions . . . 62
6.2.3 Photoluminescence at working-point conditions . . . 62
6.2.4 Photoluminescence at open-circuit conditions . . . 62
6.3 Luminescence photon emission probability . . . 63
6.4 Spectral (spectrometer-based) luminescence detection . . . 63
6.4.1 Luminescence spectra of different working points . . . 63

6.4.2 Experimental verification of caculated spectra . . . 64
6.4.3 Impact of optical properties on the luminescence spectrum . . . 66
6.4.4 Impact of base properties on the luminescence spectrum . . . 67
6.5 Integral solutions for the short- and long-wavelength range . . . 68
6.5.1 Detection in the long-wavelength range . . . 69
6.5.2 Detection in the short-wavelength range . . . 70
6.6 Integral (camera-based) luminescence detection . . . 72
6.6.1 Impact of solar cell parameters on the detected signal . . . 72
6.6.2 Rear surface reflectance of short- and long-wavelength range detection . 73
6.6.3 Dependence of the EL signal on the effective diffusion length . . . 73
6.6.4 Dependence of the EL signal on the collection length . . . 77
6.6.5 Superposition principle . . . 79
6.7 Short summary . . . 80

7 Solar cell equivalent circuit model and series resistance imaging 83
7.1 Determination of the local junction voltage . . . 83
7.1.1 Local voltage . . . 83
7.1.2 Local junction voltage . . . 84
7.1.3 Relative local junction voltage . . . 84
7.1.4 Absolute local junction voltage . . . 85
7.2 Two-dimensional equivalent circuit models of solar cells . . . 86
7.2.1 Local elements . . . 86
7.2.2 Model of interconnected diodes . . . 88
7.2.3 Model of independent diodes . . . 89
7.3 Linearization of the independent diode model . . . 91
7.3.1 Mathematical description . . . 91
7.3.2 Application of the linearized independent diode model . . . 92
7.4 Network simulations to verify the validity of the independent diode model . . . 93
7.4.1 Simulated symmetry element . . . 93
7.4.2 Voltage dependence of the local series resistance . . . 94
7.4.3 Results . . . 99
7.5 Series resistance imaging . . . 100
7.5.1 Discussions of different series resistance imaging methods . . . 100
7.5.2 Series resistance imaging of a multicrystalline silicon solar cell . . . 100
7.6 Short summary . . . 101

8 Local impact analysis (LIA) 103
8.1 Introduction . . . 103
8.1.1 Global solar cell characterization . . . 103
8.1.2 Spatially resolved characterization techniques . . . 104
8.2 Local impact analysis . . . 105
8.2.1 Mathematical description . . . 105
8.2.2 Application schema of LIA . . . 106
8.2.3 Parameter determination . . . 108

8.2.4 Physical validity . . . 108
8.3 Verifying the applicability of LIA . . . 109
8.3.1 Simulated symmetry element . . . 109
8.3.2 Network simulations with varying local series resistances . . . 109
8.4 Measurements . . . 111
8.4.1 LIA for monocrystalline silicon solar cells . . . 111
8.4.2 LIA applied to solar cell A . . . 111
8.5 Discussion . . . 114
8.5.1 Limitations . . . 114
8.5.2 Rule of thumb . . . 114
8.5.3 Outlook . . . 114
8.5.4 Median value of parameter mappings . . . 114
8.6 Short summary . . . 115

APPENDIXES

A Parameters of the used optical model **117**

B Optical reciprocity theorem **121**
B.1 Luminescence photon emission probability for EL . . . 121
B.2 Reciprocity of EL and QE: Experimental demonstration . . . 122

CHAPTER 1

Introduction

1.1 Short review of luminescence imaging

Luminescence imaging was first reported in 1963 by Uchida[1] who used an infrared-sensitive image converter tube to visualize the radiative recombination from forward biased silicon p-n junctions. An improved experimental setup was used by Penner[2] in 1988 connecting a computer-controlled video camera tube to the infrared image converter. His camera-based approach allowed for a quick and automatic inspection of large area semiconductor devices such as silicon solar cells. Only two years later, in 1990, Livescu et al.[3] reported on a real-time photoluminescence imaging system exemplarily used for the analysis of Gallium-Arsenide and Indium Phosphide substrates. In this setup, a video camera tube was used for visible light and a lead sulfide camera for infrared light.

For the analysis of large area crystalline silicon solar cells, electroluminescence imaging was brought to the attention of the photovoltaic community by Fuyuki et al. in 2005.[4] Fuyuki et al. demonstrated that the electroluminescence (EL) emission of silicon solar cells is directly detectable with commercially available silicon charge-coupled device (CCD) cameras without the need of infrared image converters. Using optical instead of electrical excitation Trupke et al.[5] utilized photoluminescence (PL) imaging as a versatile tool for solar cells and wafer characterization under realistic operating conditions comprising simultaneous optical and electrical excitation.

EL and PL images of solar cells and wafers contain extensive qualitative information about recombination properties,[6] local voltages,[7] minority carrier diffusion lengths,[8,9] microcracks,[10] surface passivation qualities[11] and shunt resistances.[12,13] Besides this qualitative information, numerous evaluation procedures for a quantitative analysis[14] have been introduced during the work at this thesis. For silicon solar cells, procedures for the local determination of voltages,[15] series resistances,[16–20] diffusion lengths,[21–25] saturation current densities,[20,26] and shunt resistances[27,28] are to be mentioned. All these techniques take advantage of measuring

the solar cell at different working points (voltage and/or illumination), by measuring specific spectral fractions of the emitted luminescence using optical filters or by analyzing the difference in luminescence emission between neighboring regions.

Regarding silicon wafers, images of the effective carrier lifetime were obtained by calibration with other lifetime measurement techniques such as infrared lifetime mapping/carrier density imaging (ILM/CDI),[29,30] quasi-steady-state photoluminescence (QSS-PL)[31,32] and by photoconductance measurements.[33–36] Without any external calibration the effective lifetime was determined with the knowledge of all relevant parameters of the used setup[24] and from the time dependent luminescence emission for a modulated optical excitation.[37–39] The fast and simple determination of the effective lifetime using PL imaging even allows for the determination of the interstitial iron concentration.[34]

1.2 Short overview of this thesis

This thesis is about luminescence-based characterization of wafer-based crystalline silicon solar cells and is divided into seven chapters:

"Camera-based setup for luminescence measurements" (Chapter 2)

For a quantitative analysis of the luminescence emission, a precise and detailed understanding of the experimental setup is essential. Chapter 2 introduces the experimental setup which I developed throughout my work at this thesis. The setup allows to capture EL and PL luminescence images at different working points. I report on the relevant equipment and analyze the components of the setup. For the first time, details about the filters and cameras used in a luminescence-imaging setup are given.

Even though the camera is the most important component, it has not been yet analyzed which camera type and sensor material is bestly suited for luminescence imaging. Therefore, I carry out a signal-to-noise analysis of different cameras used in our laboratory: Two silicon charged coupled device cameras with and without electron multiplier gain and a complementary metal oxide semiconductor indium gallium arsenide camera.

"Physical background of luminescence photon generation and emission" (Chapter 3)

A comprehensive model of the luminescence photon emission of a solar cell's surface is of mayor importance for all quantitative luminescence evaluation procedures.

Chapter 3 starts with a description of the radiative recombination process which leads to the generation of luminescence photons inside the solar cell. Consequently, an equation is derived which gives analytically the emitted luminescence photon flux of the solar cell's surface. This equation basically depends on the charge carrier distribution within the solar cell's base and a luminescence emission probability. Both quantities will be analyzed in detail in the following two chapters.

"Charge carrier distributions within the solar cell base" (Chapter 4)

Chapter 4 derives analytical charge carrier distributions required for the description of the luminescence photon flux emitted from the solar cell surface. This chapter investigates the diffusion equation of excess charge carriers within the solar cell base and gives boundary conditions for electroluminescence (EL), photoluminescence (PL) at an applied voltage (PL-wp), PL at short-circuit conditions (PL-sc) and PL at open-circuit conditions (PL-oc).

The solution of the diffusion equation leads in the case of EL to the simple and well-known charge carrier distribution in the dark. In contrast, existing descriptions for the illuminated case yield numerous terms and would not allow to study the dependences of specific solar cell parameters on the emitted luminescence photon flux. Thus, I introduce a simplification which holds for solar cells with a base thickness of more than $150\ \mu\mathrm{m}$. Consequently, I obtain compact analytical descriptions of the PL carrier distributions. All carrier distributions are visualized and compared to results from numerical device simulations at the end of this chapter.

"Luminescence photon emission probability" (Chapter 5)

Different optical models describing the photon emission probability have been published in the literature. However, most authors focused their analysis on electroluminescence imaging or on planar front and planar rear surfaces only, even though nearly all modern solar cells exhibit textured front and rough rear surfaces.

Chapter 5 derives the luminescence photon emission probability by using a volume-summation approach which sums up all volume elements leading to photon emission in direction to the detector. In contrast to similar approaches published in literature, this approach explicitly considers spherical angles of emission and detection and optical confinement of solar cells, which both are of major importance for the isotropically generated long-wavelength luminescence light.

As the result a relation is obtained which states that the luminescence photon emission probability directly follows from the generation profile of impinging photons. I can thus take advantage of previously published optical models developed for the absorption of light. I choose a generation profile which is especially well suited for long-wavelength light and describes planar and textured silicon solar cells with rough rear surfaces. Thus, a comprehensive luminescence photon emission probability which holds for electro- and photoluminescence imaging is obtained.

At the end of this chapter I show one application of the presented optical model and calculate the expected resolution of luminescence imaging for different wavelengths.

"Spectral and integral analysis of the luminescence emission" (Chapter 6)

Chapter 6 analyzes the spectral and integral (in terms of wavelengths) luminescence emission from silicon solar cells. Therefore, the luminescence emission integral is used to calculate luminescence emission spectra of silicon solar cells. These spectra are analyzed for different working points, different electrical and optical properties and are compared to experiment. Regarding the integral (camera-based) detection of luminescence photons, novel analytical solutions for EL, PL-wp, PL-

oc and PL-sc in the short- (< 920 nm) and long-wavelength (> 1100 nm) range are introduced in this work.

I make use of the resulting solutions by calculating the impact of various parameters of the solar cell device onto the luminescence signal detected with a camera. Experimentally, I show that the long-wavelength EL emission is proportional to the collection length L_{C}. In addition, an analysis by means of simulations and experiments reveals the dependence of the short-wavelength EL emission on the effective diffusion length L_{eff}.

"Solar cell equivalent circuit model and series resistance imaging" (Chapter 7)

While the previous chapters concentrated on the luminescence emission of one local region only, chapter 7 interconnects these regions using equivalent circuit models.

In general, the local regions are interconnected by the emitter, resulting in an extensive two-dimensional network where all regions are electrically interconnected. However, in most practical cases, the application of such a network is complicated and requires large computational power. For these reasons, I use a simplified model, the independent local diode model, which uses an effective local series resistance as a connection to the terminal. For the first time, I explain the transition from the interconnected to the independent local diode model. This transition then allows me to verify the independent model for certain parameter ranges by means of simulations. In addition, it allows me to explain the differences between the absolute and the differential local series resistance.

The independent local diode model in combination with luminescence imaging allows to determine images of the local series resistance. Exemplarily, a series resistance image of a multicrystalline silicon solar cell is given at the end of this chapter.

"Local impact analysis (LIA)" (Chapter 8)

Finally, in chapter 8, I introduce a novel application of luminescence imaging. Since the local series resistance analysis, presented in the previous chapter, allows to connect all local elements to the terminals, the solar cell can be consequently simulated as a whole. Parameter mappings obtained from different characterization methods are fed into the calculations and describe the recombination within each of the local elements. This so-called local-impact analysis (LIA) results in a new (calculated) global energy conversion efficiency. Global and local parameters may be virtually modified to determine the impact of certain regions onto the global energy conversion efficiency. I verify LIA by means of experiment and simulations and explicitly determine the impact of an increased local series resistance onto the global energy conversion efficiency. The connection of the local luminescence emission to the global energy conversion efficiency was demonstrated for the first time in this work.

CHAPTER 2

Camera-based setup for luminescence measurements

I present the luminescence imaging setup I developed throughout my work at this thesis. I do not only report on the relevant equipment[31,40,41] but also analyze the components of the setup in detail. For the first time, details about the filters and cameras used in a luminescence-imaging setup are given.

Even though for a quantitative analysis of the luminescence emission the camera is of specific importance it has not yet been analyzed which camera type and sensor material is bestly suited for luminescence imaging. For this reason, I compare a silicon charged coupled device (CCD) camera with a back-illuminated silicon CCD camera comprising an electron multiplier (EM) gain and a complementary metal oxide semiconductor (CMOS) indium gallium arsenide (InGaAs) camera.

The question arises which camera and which parameters like the exposure time lead to the best result in a given total measurement time. Therefore I analyze the dominant noise sources along with the signal-to-noise ratio for all three cameras. Moreover, for the detection of the luminescence emission of silicon solar cells and wafers, the signal-to-noise ratio of these cameras is calculated and experimentally confirmed with respect to the total measurement time and the total luminescence photon flux. Using these results, I demonstrate that the signal-to-noise ratio improves with the square-root of the total measurement time and that the choice of camera for the best results depends on the emitted luminescence photon flux of the sample.

2.1 Detailed setup description

The experimental setup shown in Fig. 2.1 comprises a housing, a measurement chuck, a solar cell contacting unit, a bipolar power supply, a semiconductor laser, a homogenization optics, a camera, various filters, two multimeter, a vacuum pump, a water thermostat, a linear unit and a computer.

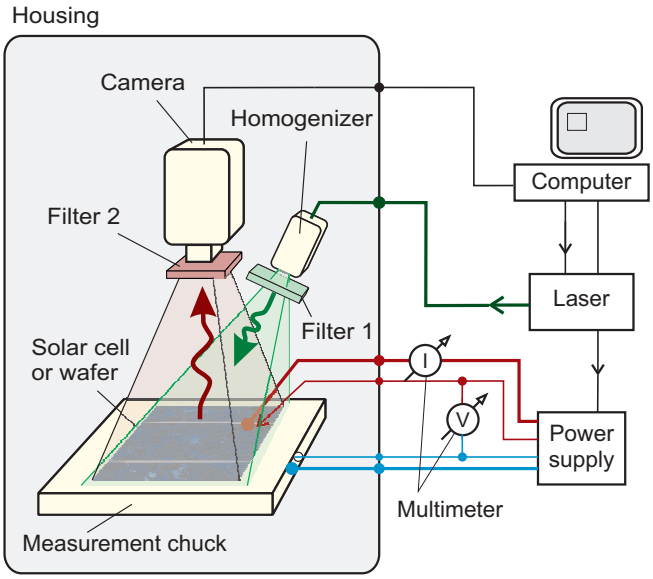

Figure 2.1: *Setup for spatially resolved luminescence measurements of silicon solar cells and wafers.*

2.1.1 Housing

To avoid the detection of ambient light, the camera, the measurement chuck, the solar cell contacting unit and the homogenization optics are mounted in a dark box ($1290\ \mathrm{cm} \times 700\ \mathrm{cm} \times 690\ \mathrm{cm}$). All metallic parts of this box are blackened to minimize interference due to multiple reflected light within the box. The side-walls of the box consists of black polyvinyl chloride (PVC) plastic.[a] Measurements show that the hemispherical reflectance of this material is below $6\ \%$ in the wavelength range of $400\ \mathrm{nm}$ to $1200\ \mathrm{nm}$. Any objects inside the box have to be carefully examined to not disturb the measured luminescence emission of the solar cell or the wafer. I measure (optically excited by the semiconductor laser) weak parasitic luminescence emission from sheets of paper, strong emission from pertinax that is used for the isolation of the sense and the current wires and strong emission from cables and connectors (particularly if coated with a red color).

2.1.2 Sample mounting and contacting

The silicon sample under test, a solar cell or a wafer, is mounted on a vacuum chuck[b] for samples of up to $20 \times 20\ \mathrm{cm}^2$. The chuck is temperature-controlled by a closed-loop water thermostat,[c] thus offering a temperature range from approximately $5\ ^\circ\mathrm{C}$ to $85\ ^\circ\mathrm{C}$. A small PT1000 temperature sensor is mounted within the chuck's surface. The temperature sensor is pressed to the rear of the sample by a small spring and has no direct contact with the measurement

[a] SIMONA Simocel-Color black $6\ \mathrm{mm}$
[b] ISFH, custom-made product
[c] Haake, DC30-K15

chuck. Thus, the measured temperature corresponds directly to the temperature of the sample's rear surface.

The chuck's surface exhibits small grooves connected to a vacuum pump to allow for a homogeneous suction of the sample onto the chuck. For silicon wafers, the grooves of the chuck may appear as a pattern in the captured luminescence image due to a laterally inhomogeneous reflectance. In such cases, the wafer is placed on a thin, blackened brass pad without any grooves, accepting the disadvantage of no suction and thus a reduced temperature stabilization.

2.1.3 Electrical and optical stimulation of luminescence

For solar cells, a four-quadrant voltage and current power supply[d] controls the applied voltage. Depending on the operating conditions electrical current is extracted from or fed into the solar cell. To eliminate errors due to lead resistances a four-point contacting scheme with remote sensing is used. The busbars of the solar cell under test are contacted by up to three bars containing spring loaded needles. The brass chuck itself is used as the rear contact. One needle in each bar and one in the chuck are isolated from the others to sense the voltage (sense contacts).

To determine the applied voltage V_{appl} at the solar cell a multimeter[e] connected to the sense wires is used. Regarding current measurements, one of the current carrying wires contains a small four-wire resistance

$$R_{\mathrm{m}} = 100\ \mathrm{m\Omega} \tag{2.1}$$

in series. The voltage drop ΔV at R_{m} is measured with a second multimeter.[f] The current fed into or extracted from the solar cell follows directly from Ohm's law.

For the monochromatic illumination a gallium arsenide (GaAs) diode laser[g] is used which exhibits a central wavelength (CWL) of $810\ \mathrm{nm}$. For silicon, this CWL corresponds to an absorption length of $\sim 13\ \mu\mathrm{m}$. The maximum continuous wave output power of the laser is $30\ \mathrm{W}$. A beam homogenizer[h] based on microlenses shapes the fiber output beam to a square flat-top. For the optimum working distance of $75\ \mathrm{cm}$ an area of $16 \times 16\ \mathrm{cm}^2$ is illuminated at an angle of $15°$ with an homogeneity of $\pm\ 10\ \%$. Considering the losses of the fiber and the optics ($\sim 40\ \%$), an equivalent photogeneration rate in silicon of up to two-thirds of a sun is reached.

2.1.4 Camera

The camera detecting the luminescence emission is mounted directly above the contacting unit. Three different cameras were used in this work: Two silicon (Si) charge-coupled device cameras[i]

[d] Kepco, BOP36-28MG
[e] Keithley, Model 2000
[f] Keithley, Model 2000
[g] Jenoptik unique-mode, JUM30k/400/20
[h] Bayerisches Laserzentrum GmbH, custom-made product
[i] PCO, sensicam qe; Hamamatsu, C9100-13

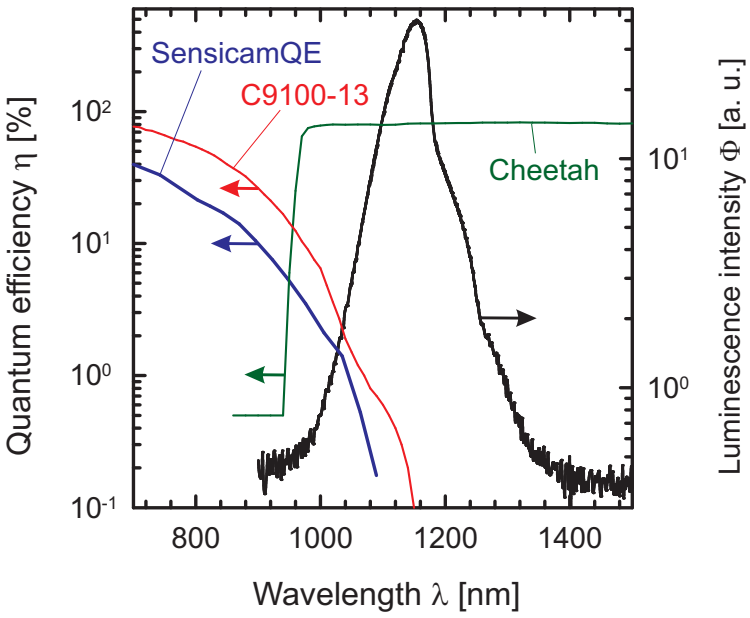

Figure 2.2: *Quantum efficiencies of the used cameras (manufacturer information) and an electroluminescence spectrum of a monocrystalline silicon solar cell.*

and one indium gallium arsenide (InGaAs) complementary metal-oxide semiconductor camera.[j] All relevant parameters of these cameras are listed in Tab. 2.1. The main difference between the Si and InGaAs camera is their sensitivity to different wavelength ranges. This demonstrates Fig. 2.2, which shows the quantum efficiencies of the used cameras and an electroluminescence spectrum of a monocrystalline silicon solar cell.[k]

InGaAs absorbs photons ranging from 900 to 1700 nm and thus covers the whole range of the luminescence emission from silicon. In contrast, Si is better suited for the visible range and its quantum efficiency reduces significantly for wavelengths larger than 1000 nm. Note that I focus in this paper on the detection of band-to-band luminescence emission only. Additional light emission (see for example Ref. 42 and papers cited in there) may be found in the sub-bandgap range between 1400 nm and 1700 nm for solar cells and wafers and in the visible range for reverse-biased solar cells. Figure 2.2 demonstrates that the sub-bandgap light detection requires an InGaAs detector and the visible light emission a Si detector.

All three cameras feature a C-mount as the lens mount, which corresponds to a flange focal distance of

$$b = 17.526\ \text{mm}. \tag{2.2}$$

The same lens[l] is used for all three cameras. The aperture of this lens is 1.4 and the focal

[j] Xenics, cheetah

[k] The quantum efficiency data was obtained from the manufacturer and the spectra was measured using a BWSpec BTC261E spectrometer.

[l] Pentax, C2514-M (KP)

Table 2.1: *Camera parameters.*

	sensicam qe (Si)	**C9100-13 (Si)**	**cheetah (InGaAs)**
Manufacturer	PCO	Hamamatsu	Xenics
Operation mode 1	Lowlight, High Gain	Normal-CCD (nrm)	Low Gain (LG)
Operation mode 2	–	EM-Gain 1200 (EM)	High Gain (HG)
Sensor	Sony ICX285-AL Interline CCD	E2V CCD97 Back-thinned frame transfer with on-chip amplification (EM-Gain)	XFPA-1.7-640-TE1-V4 Xenics-built
Sensor size $[\mathrm{mm}^2]$	6.6×8.8 (2/3")	8.2×8.2	12.8×10.2
Pitch size $[\mu\mathrm{m}]$	6.45	16	20
No. of pixels	$1\,376 \times 1\,040$	512×512	640×512
Sensor cooling $[^{\circ}\mathrm{C}]$	-12	-65	4
Full well capacity N_{FW} $[\mathrm{e}^-]$	18 000	370 000	1 250 000
A/D conversion $[\mathrm{bit}]$	12	16	14
Conversion factor $[\mathrm{e}^-/\mathrm{DU}]$	2	1.4 (nrm) and 5.8 (EM)	76.29 (LG) and 5.34 (HG)
Dark electron flux Φ_{drk} $[\mathrm{e}^-/\mathrm{s}/\mathrm{px}]$	0.64	0.01	280 000 (LG) and 220 000 (HG)
Signal electron flux[a] Φ_{s} $[\mathrm{e}^-/\mathrm{s}/\mathrm{px}]$	0.388×10^{-3}	1.833×10^{-3}	0.833 (LG) and 0.666 (HG)
Readout noise σ_{ro} $[\mathrm{e}^-/\mathrm{px}]$	4.8	16.8 (nrm) and 215 (EM)	122 (LG) and 104 (HG)
Temperature noise σ_{tmp} $[\mathrm{e}^-/\mathrm{px}]$	0	0	620 (LG) and 62 (HG)

[a] Signal electron flux for an electroluminescence spectrum emitted from a solar cell operating at an applied voltage of 521 mV. To be able to compare the signal electron flux for different cameras we maintained equal measurement conditions (same optics, same position of the solar cell's image within the sensor, same luminescence intensity). For the sensicam qe camera a 2×2 binning was used to account for the larger image sensor.

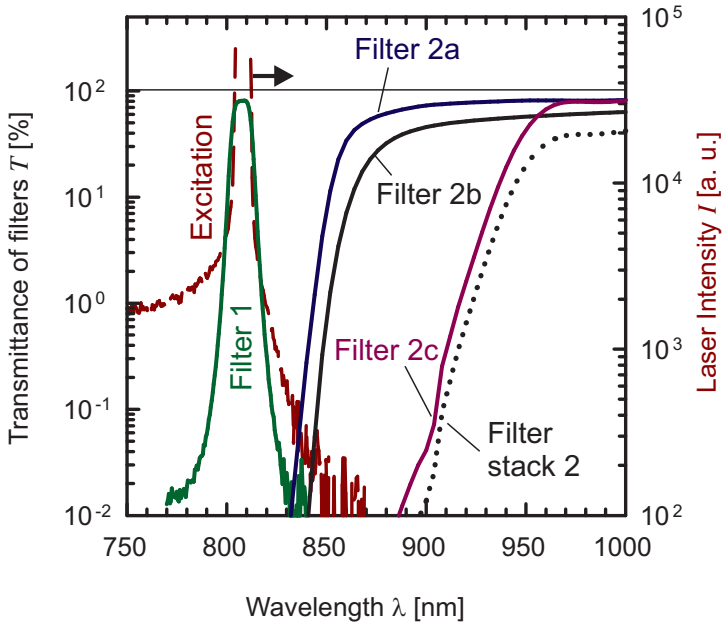

Figure 2.3: *Laser spectrum and transmittances of the filters used for photoluminescence imaging.*

length $f = 25\ \mathrm{mm}$. To cover the whole area of the sensor (width B) with the image of the solar cell (width G) the distance g between the solar cell and the lens is adjustable. Therefore, the camera is mounted on a linear unit which changes g between $0\ \mathrm{cm}$ and $80\ \mathrm{cm}$. The minimum object distance (MOD) of this lens is $25\ \mathrm{cm}$, but using close-up lens rings smaller distances are achievable.

2.1.5 Filters

Optical filters are important for quantitative measurements of the luminescence emission. For EL measurements a longpass filter[m] is used to avoid the detection of stray light. Due to the box this longpass filter is not required during measurement but is useful when focusing the camera with the box open. The filter choice is much more important for PL measurements of silicon wafers or solar cells since reflected excitation light has to be suppressed. Figure 2.3 shows the spectra of the laser and the transmittances of the filters that are used in our PL setup.[n]

Filter 1 in Fig. 2.3 is a bandpass[o] which is positioned at the exit of the homogenizer (see Fig. 2.1) and blocks the emission of the laser at long wavelengths. This is necessary since the sharp laserline is weakly superimposed by a broad spectrum due to spontaneous emissions from the GaAs laser diode [the amplified spontaneous emission (ASE) spectra]. Thus, this filter has a transmittance larger than $70\ \%$ in the wavelength range from $805\ \mathrm{nm}$ to $815\ \mathrm{nm}$ and exhibits an

[m] Semrock, Razoredge 830
[n] The data was measured using a BWSpec BTC112E and a Cary 5000 spectrometer.
[o] bk-Interferenzoptik, custom-made product

optical density (I_0: Intensity of incident light, I: Intensity of light that has passed through the filter)

$$\mathrm{OD} = \log_{10}\left(\frac{I_0}{I}\right) \tag{2.3}$$

higher than 8 for wavelengths larger than $850\ \mathrm{nm}$. In order not to damage the filter, it is important to mount the filter at the exit of the homgenization optics where the laser output beam is already widened and the intensity is thus reduced.

The filter stack 2 in Fig. 2.3 consists of several longpass filters positioned in front of the camera (see Fig. 2.1). It blocks the reflected laser light while exhibiting a high transmission for the luminescence photons. For PL measurements with the InGaAs-camera the requirements for this stack are low since the InGaAs-camera has a small quantum efficiency at the central wavelength of the laser (see Fig. 2.2). Hence, a standard $1000\ \mathrm{nm}$ longpass filter[p] is sufficient in most cases. For PL measurements with Si-cameras, which feature a high quantum efficiency at the laser's central wavelength, a filter stack with an extremely high optical density to block the reflected laser light is crucial. A $20\ \mathrm{mm}$ thick absorbing glass filter[q] provides this optical density at $810\ \mathrm{nm}$ (Filter 2b in Fig. 2.3). However, due to the strong absorption of photons within the RG850 filter the filter itself emits light[43] because it contains nano-crystallites of II–IV semiconducting compounds.[44] Even though in most cases this parasitic light emission is negligibly small it may disturb the measurement significantly for PL measurements at solar cells or wafers with very low luminescence emission.

Two additional interference filters (Filter 2a and 2c) are therefore placed on both sides of the RG850 (Filter 2b). Filter 2a, positioned between the RG850 and the sample, reflects the vast majority of the laser light back into the setup and thus decreases the light intensity entering into the RG850. Filter 2c, positioned between the RG850 and the camera, blocks the parasitic light generated within the RG850. Filter 2a and 2c are custom-made longpass filters[r] (2a: $856\ \mathrm{nm}$, 2c: $930\ \mathrm{nm}$) which exhibit a high blocking (2a: OD9, 2c: OD5) for short wavelengths and a high transmission ($90\ \%$) for longer wavelengths. The transmittances of these filters are shown in Fig. 2.3 together with the resulting transmittance of the filter stack 2 (comprising filter 2a, 2b and 2c).

[p] Thorlabs, FEL1000
[q] RG850, Schott-Glass
[r] bk-Interferenzoptik, custom-made products

2.2 Data acquisition process of luminescence imaging

The whole data acquisition process is controlled by a computer software. This software was developed at ISFH using the programming language Labview (National Instruments). The power supply and the multimeter are controlled via a General Purpose Interface Bus (GPIB) and the laser, the linear unit and the water thermostat via an RS232 interface. The two Si-cameras are connected to the computer using proper PCI-cards from the manufacturer and the Cheetah camera is connected via an Ethernet interface.

To prepare the setup for the capturing of luminescence images, the sample under test is firstly mounted on the measurement chuck. Then, the camera's height is adjusted to use the full sensor size for the image of the solar cell and camera is focused to the luminescence emission. Finally, the parameters characterizing the measurement conditions are set in the data acquisition program. A batch mode may be used to automatically measure luminescence images at a sequence of measurement conditions.

After this preparations the data acquisition is fully automatic. The data acquisition program first initializes all devices and, in case of a solar cell, performs a contact check. Then, the power supply and the laser are switched from standby to operating mode to stimulate the luminescence emission. While the camera is capturing the luminescence image the temperature of the sample is measured and in case of a solar cell additionally the applied voltage and current. After exposure, the resulting luminescence image is read out from the camera and the power supply and or the laser are put back into standby mode. This procedure is repeated with the laser and the power supply in standby mode (no luminescence stimulation) to measure the so-called dark image. The dark image is automatically subtracted from the luminescence image to account for remaining stray light and any camera offsets.

To improve the signal-to-noise ratio the data acquisition process is repeated as often as required. After averaging M-times, the signal for each pixel

$$N_\mathrm{s} = \frac{1}{M} \sum_{i}^{M} N_{\mathrm{s},i} \tag{2.4}$$

and the standard deviation

$$\sigma_\mathrm{s} = \sqrt{\frac{1}{M} \sum_{i}^{M} (N_\mathrm{s} - N_{\mathrm{s},i})^2} \tag{2.5}$$

is calculated. The signal-to-noise ratio becomes

$$\mathrm{SNR} = \frac{N_\mathrm{s}}{u} = \frac{N_\mathrm{s}}{\sigma_\mathrm{s}} \sqrt{M}, \tag{2.6}$$

where $u = \sigma_\mathrm{s}/\sqrt{M}$ is the standard deviation of the mean.

A non-uniformity correction (NUC) of the acquired images is necessary to correct for inhomogeneities of the lateral quantum efficiency of the camera sensor and inhomogeneous transmission of the lenses and filters. Therefore, the luminescence image is divided by the NUC

image which is captured using a homogeneous luminescence light source. My approach is to use the same focus settings as for the real measurement but with the camera as close as possible (typically $10\ \mathrm{cm}$) above a monocrystalline solar cell. In this position the solar cell is completely out of focus for the camera and illuminates the sensor homogeneously. The NUC image is captured with an exposure time corresponding to three-fourths full well capacity and repeat the measurement at least 100 times to lower the dark and photon noise.

Further correction of the images is required if defect pixels exist. Defect pixels on the sensor have no signal at all (dead pixel) or too much signal (hot pixel) due to a high dark current. These defect pixels have to be neglected in any quantitative analysis. Most of the defect pixels are at a fixed position and can thus be identified easily and corrected for by assigning the average value of the neighboring pixels.

2.3 Exemplary luminescence images

The presented experimental setup allows to measure the luminescence emission of solar cells and wafers at different operation conditions.

2.3.1 Silicon solar cells

Figure 2.4 shows three images of the luminescence emission of a poorly processed multicrystalline silicon solar cell. The total measurement time for all images is 20 s. In all images, the busbars and the fingers appear as dark lines because the luminescence photons cannot emerge at this regions from the solar cell. Fig. 2.4(a) shows an electroluminescence image at an applied voltage of 625 mV. In this image a dark pattern can be observed in the upper left side and some dark but non-symmetric regions in the lower right. Fig. 2.4(b) and (c) show photoluminescence images of the same solar cell. For this images, the laser illumination is set to 0.5 suns. While the solar cell in Fig.2.4(b) is held at a specific working point (PL-wp) all current is extracted from the solar cell in Fig. 2.4(c), which means short-circuit conditions (PL-sc). The dark pattern of the EL image appears bright in the PL-wp image and disappears in the PL-sc image. The dark non-symmetric regions on the lower right side appear are also observable in the PL-wp and PL-sc images.

The images in Fig. 2.4 demonstrate high-quality images that are full of information on the strengths and weaknesses of the investigated samples. In this work, I will only give a short qualitative interpretation of these images. Clearly visible in Fig. 2.4 is a locally increased series resistance probably induced by the transport band in the solar cell's firing process. While this series resistance appears as a decreased luminescence signal in the EL image [see Fig. 2.4(a)], it leads to an increased signal in the PL-WP image [see Fig. 2.4(b)].[5] In contrast, the PL-sc image [see Fig. 2.4(c)] does hardly show any pattern of the local series resistance. This becomes understandable if considering the shape of the light IV characteristics where a small or moderate series resistance does not have any impact on the short circuit current. The PL-sc image shows the diffusion-limited carriers,[16,45] as will be explained in section 7.1.4. The recombination properties of the multicrystalline material are visible in all three images shown in Fig. 2.4. Shunts would appear as a decreased luminescence signal in the EL and in the PL-wp image. Obvious shunts are not present. Unless the shunt resistance is very small it will not appear in the PL-sc image.

2.3.2 Silicon wafers

Figure 2.5 shows the effective lifetime image of a multicrystalline silicon wafer. The lifetime values were obtained by a PL measurement calibrated with steady-state photoconductance.[36] The PL image is captured with the Hamamatsu camera at an illumination intensity of 1.5 suns and a total measurement time of 3.5 s. The high illumination intensity could be achieved because only a region of 8×8 cm^2 was measured.

The image shown in Fig. 2.5 of a silicon wafer shows the local effective lifetime. Clearly visible are the grains and the grain boundaries of the multicrystalline material. The grains appear in Fig. 2.5 as quite homogeneous regions with lifetime values around 15 µs. These regions are separated by grain boundaries which correspond to dark lines with a high recombination

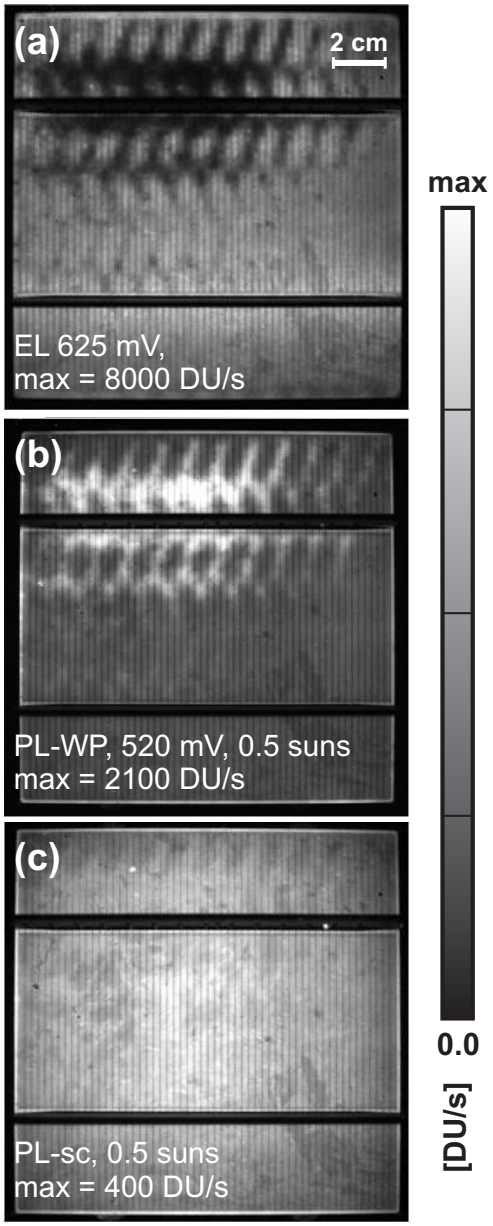

Figure 2.4: *Luminescence image of a poorly processed multicrystalline solar cell at different working points. The images are captured with the cheetah camera.*

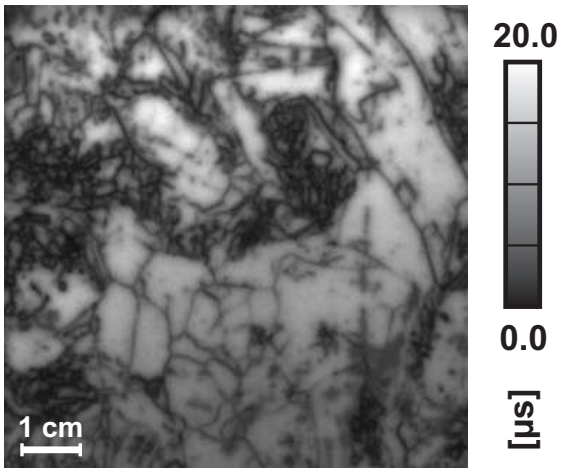

Figure 2.5: *Lifetime image of a multicrystalline wafer captured with the Hamamatsu camera. The effective lifetime was calibrated with steady-state photoconductance.*[36] *The total measurement time for the PL image is 3.5* s *and the spatial resolution 155* µm.

activity. In addition, areas with a high density of dendritic lines are found which originate from recombination active intragrain defects such as stacking faults and dislocations. These crystal irregularities are recombination active due to dangling bonds or decoration with recombination active impurities.[46]

2.4 Camera noise analysis

I carry out a detailed noise analysis for the different cameras used in the presented experimental setup. This noise analysis focuses on the analytical determination of the signal-to-noise ratio

$$\mathrm{SNR} = \frac{N_\mathrm{s}}{u} \tag{2.7}$$

which depends on the number of generated signal electrons N_s and its standard deviation of the mean u. Based on this noise analysis I deduce sets of camera parameters to obtain the highest signal-to-noise ratio.

In every camera system many noise sources exists,[47] but for luminescence measurements I identify photon noise, dark noise, readout noise and cooling fluctuations as the most dominant sources. In the following, I give a short review of the different noise sources. Note that the presented statistics of the noise sources are only valid if the analysis is carried out in signal electrons (and not in digital units).

2.4.1 Different noise sources of luminescence measurements

Signal electrons and noise

The photon noise is an elementary characteristic of the discrete nature of the light and is described as a variation of the emitted photons in time. It is described with the Poisson statistics and the variance of N_ph photons is N_ph. These photons are converted to signal electrons with the sensor's quantum efficiency $\eta(\lambda)$,

$$N_\mathrm{s} = \eta\, N_\mathrm{ph}. \tag{2.8}$$

Hence, the statistical noise of the photons is directly assigned to the signal electrons. Thus, the variance σ_s^2 of N_s signal electrons is

$$\sigma_\mathrm{s}^2 = N_\mathrm{s} = \Phi_\mathrm{s}\, t_\mathrm{exp}, \tag{2.9}$$

where I used the signal electron flux Φ_s, describing the generated signal electrons per time and per pixel, and the exposure time t_exp of the sensor.

Dark electrons and noise

Thermal stimulation within the sensor generates free electrons N_drk which are indistinguishable from the signal electrons and thus wrongly counted as signal. Besides, the same Poisson statistics applies to those thermally generated electrons and thus their variance using the dark electron flux Φ_drk is

$$\sigma_\mathrm{drk}^2 = N_\mathrm{drk} = \Phi_\mathrm{drk}\, t_\mathrm{exp}. \tag{2.10}$$

Readout noise

The readout noise σ_ro is added to each pixel due to the readout electronics. The readout electronics handles the amplification of the signal electrons, the conversion into a voltage and its digitization to digital units.

Cooling fluctuations

Fluctuations of the sensor's cooling cause an additional noise source σ_{tmp} because the amount of dark current mainly depends on the sensor's temperature. Temperature fluctuations vanish in the used Si cameras because of the very deep cooling and the large band gap. Instead, for the used InGaAs camera, σ_{tmp} is a quite substantial noise source. I estimate σ_{tmp} by measuring the temperature variance and the relation of temperature and dark signal.

2.4.2 Noise modeling

For a modeling of the signal-to-noise ratio the total noise of the image acquisition has to be determined from the presented parameters. Since the noise sources are not correlated, the variances simply add up to the total variance. For the total noise σ_{df} of the dark-frame subtracted image,

$$\sigma_{\mathrm{df}}^2 = \sigma_{\mathrm{s}}^2 + 2\sigma_{\mathrm{drk}}^2 + 2(\sigma_{\mathrm{ro}}^2 + \sigma_{\mathrm{tmp}}^2), \tag{2.11}$$

the dark noise and the readout noise have to be counted twice as these noise sources are contained in the illuminated as well as in the dark image. The noise of the dark-frame subtracted image is thus bigger than the noise of the single image. However, the subtraction of the dark frame is substantially necessary for the quantitative analysis of luminescence images since it removes the dark current and remaining stray light from the signal.

Equation (2.11) holds for sensors without amplifying gain. For electron multiplying (EM) CCD sensors, another noise source comes into play which is called excess noise F and is a result of fluctuations of the signal multiplying gain g.[48] This signal multiplying gain noise effects also other detected electron charges except the readout noise. Therefore, for EMCCD sensors Eq. (2.11) becomes[49]

$$\sigma_{\mathrm{df}}^2 = g^2\, F^2 \cdot (\sigma_{\mathrm{s}}^2 + 2\,\sigma_{\mathrm{drk}}^2 + 2\,\sigma_{\mathrm{tmp}}^2) + 2\,\sigma_{\mathrm{ro}}^2. \tag{2.12}$$

The excess noise F can be well estimated[49] with $\sqrt{2}$ and the gain g depends on the specific camera settings. In the following, Eq. (2.12) will be used for the total noise; the non-amplifying case is obtained using $g = 1$ and $F = 1$.

The presented setup allows to average multiple images M times. This results in a smaller standard deviation of the mean of

$$u = \frac{\sigma_{\mathrm{df}}}{\sqrt{M}}. \tag{2.13}$$

Putting the sum of variances [Eq. (2.12)] and the latter equation of the absolute error [Eq. (2.13)] into the definition of the signal-to-noise ratio [Eq. (2.7)] gives

$$\begin{aligned}\mathrm{SNR} = \sqrt{M}\,\Phi_{\mathrm{s}}\,g\,t_{\mathrm{exp}} \cdot \Big(F^2\,g^2\,(\Phi_{\mathrm{s}} + 2\,\Phi_{\mathrm{drk}})\,t_{\mathrm{exp}} + \\ + 2\,\sigma_{\mathrm{ro}}^2 + F^2\,g^2\,2\,\sigma_{\mathrm{tmp}}^2\Big)^{-1/2}.\end{aligned} \tag{2.14}$$

Maximum signal-to-noise ratio

The question arises which camera settings (long exposure time or often averaging) to choose to obtain the best signal-to-noise ratio in a total measurement time

$$T = 2\,M\,t_{\mathrm{exp}}. \tag{2.15}$$

Using the parametrized signal-to-noise ratio of Eq. (2.14) I deduce that due to the readout- and offset-noise a long exposure time always gives a higher SNR than averaging more often with a shorter exposure time. More generally, since the exposure time is limited by the full well capacity N_{FW}, I state that for a certain luminescence intensity and dark current the exposure time giving the highest SNR is

$$t_{\mathrm{exp}}^{\mathrm{max}} = \frac{h \cdot N_{\mathrm{FW}}}{\Phi_{\mathrm{s}} + \Phi_{\mathrm{drk}}}. \tag{2.16}$$

The factor h accounts for the optimum range of each camera to maintain a good linear relationship of impinging photons and resulting signal. Since it is recommended to not fully saturate the pixel usually $h \approx 0.75$ is used for the cameras used the presented experimental setup. Putting Eq. (2.16) into Eq. (2.14) I obtain

$$\mathrm{SNR}^{\mathrm{max}} = \sqrt{T}\,\Phi_{\mathrm{s}}\,g \cdot \cdot \sqrt{\frac{t_{\mathrm{exp}}^{\mathrm{max}}}{2\,F^2\,g^2\,(\Phi_{\mathrm{s}} + 2\,\Phi_{\mathrm{drk}}) \cdot t_{\mathrm{exp}}^{\mathrm{max}} + 4\,\sigma_{\mathrm{ro}}^2 + 4\,F^2\,g^2\,\sigma_{\mathrm{tmp}}^2}} \tag{2.17}$$

which holds if

$$M^{\mathrm{min}} = T/2/t_{\mathrm{exp}}^{\mathrm{max}} \geq 2 \tag{2.18}$$

is a whole number. The maximum possible SNR of the camera thus depends on the particular camera settings and the luminescence intensity. Different cameras can be better suited for low intensity than for high intensity and vice versa.

2.4.3 Calculations and measurements

Signal-to-noise ratio image examples

Figure 2.6 exemplary demonstrates that a long exposure time yields a higher signal-to-noise ratio than often averaging. Both images are taken for the same solar cell at the same operation conditions. The total measurement time $T = 200$ s was held fixed. The measurement parameters exposure time and number of averages are set for Fig. 2.6(a) to 1 s and 100 times and for (b) to 100 s and 1 time. It can be clearly seen that the image quality of Fig. 2.6(b) is better which corresponds to a higher signal-to-noise ratio of 12.0 [compare to 2.9 for (a)].

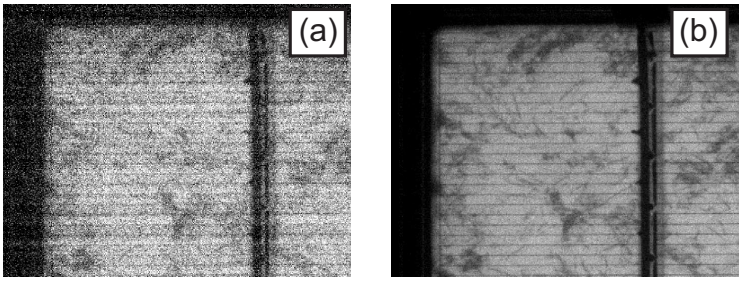

Figure 2.6: *Comparison of luminescence (EL) images of a silicon solar cell using a constant total measuring time. I measure for image (a) a SNR of 2.9 and for images (b) 12.0. The images are captured using the sensicam qe silicon CCD camera.*

Signal-to-noise ratio as a function of exposure time

For each camera type I experimentally determine the parameters σ_{ro}, σ_{tmp}, Φ_{drk} and Φ_{s} for the same source of luminescence. The results are listed in Tab. 2.1. Note that the InGaAs-Camera (cheetah) has a much higher dark electron flux than the Si-cameras. Using Eq. (2.14) I can thus calculate the expected SNR for each exposure time and luminescence intensity and compare the calculation with directly measured SNR values. Figure 2.7 shows the results for all three cameras. A good agreement over a wide range of exposure times demonstrates the validity of the presented model and of the determined parameters.

Maximum signal-to-noise ratio

For the cameras investigated in this work Fig. 2.8 shows the dependence of the SNR of each camera to a certain luminescence intensity. The lines in this figure correspond to calculated values while the points are measured values. For a better understanding and comparison, the luminescence intensities are expressed additionally as a local voltage. Note that the correlation to the local voltage does only hold for the specific setup used.

In Fig. 2.8 a good agreement between the measured and simulated data is obtained. As expected, the SNR of the InGaAs camera is about one magnitude higher than the SNR of the Si cameras investigated in. But looking at camera costs per SNR achievable I can't identify a clear winner. It also becomes clear in Fig. 2.8, that the suitability of the different cameras and different camera modes to measure a high-quality image of the luminescence emission depends on the amount of captured luminescence. The EM mode of the Hamamatsu C9100-13 is better suited to very low signal measurements while the normal camera mode gives a better SNR for high signals. This behavior is observed in Fig. 2.8 in the simulated as well as in the measured data.

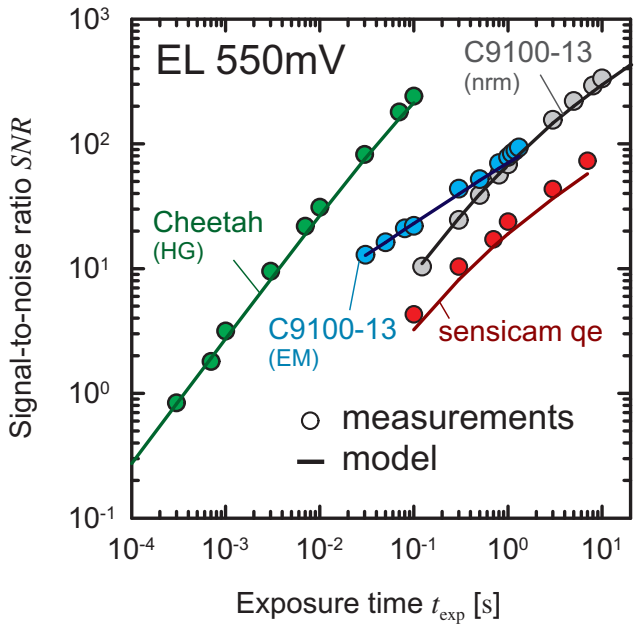

Figure 2.7: *Calculated (lines) and measured (points) SNR curves for the sensicam qe and the cheetah camera for the same luminescence intensity of a solar cell hold at 550* mV*. The resulting signals were averaged 20 times.*

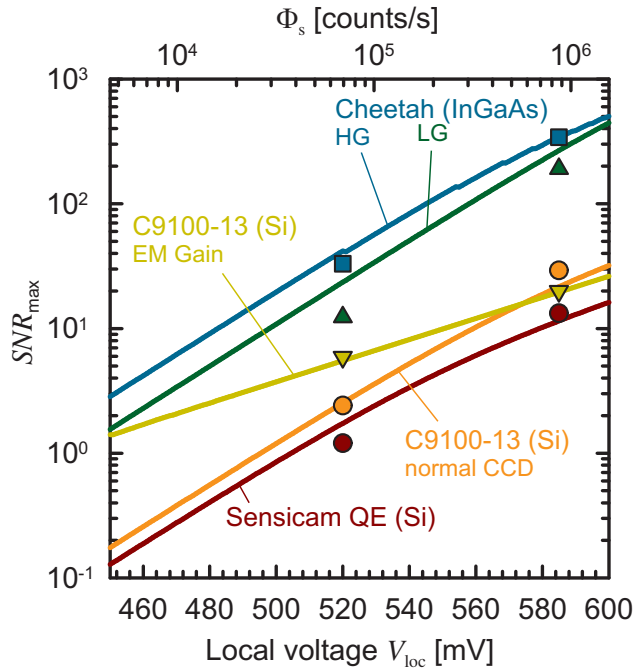

Figure 2.8: *Comparison of the maximum signal-to-noise ratio for different cameras. The total measurement time is $T = 1$* s*. The lines give the simulated signal-to-noise ratio and the points correspond to measured values.*

2.5 Short summary

I built and characterized a luminescence imaging setup allowing for a quantitative analysis of the luminescence emission of silicon solar cells and wafers. The main challenge of such a setup is the appropriate choice of the optical filters and of the camera.

Optical filters are required to protect the measurement of the excitation light. I found that two different types of filters are necessary. One bandpass filter is positioned at the exit of the homogenization optics and blocks the amplified spontaneous emission at wavelengths other than the central-wavelength. The second filter is positioned before the camera. It is a stack of two interference and one absorbing glass filter and exhibits a high optical density at the central-wavelength of the laser.

Regarding the choice of cameras, I compared three different types of cameras with respect to the resulting signal-to-noise ratio (SNR) for luminescence imaging. The SNR of the used indium gallium arsenide (InGaAs) camera is about one to two magnitudes higher than the SNR of the two silicon (Si) cameras under investigation. For the two silicon cameras, the electron multiplier gain is only an advantage for samples under low excitation conditions but suffers from a lower SNR under higher excitation conditions. But from an economically point of view, looking at camera costs per SNR achievable, no clear winner could be identified.

CHAPTER 3

Physical background of luminescence photon generation and emission

This chapter covers the luminescence photon generation inside the solar cell and the detection geometry. It describes in detail the radiative recombination process of charge carriers which generates the luminescence photons. These photons then travel through the semiconductor until they are absorbed again from the silicon or are emitted from the surfaces. By considering only the luminescence photons, which are finally sent in direction to the detector, I obtain in the present chapter an expression, which describes the luminescence photon emission detectable with a camera.

3.1 Detection geometry

Figure 3.1 introduces the detection geometry and the relevant physical parameters used throughout this work. The generation of luminescence photons (γ_{lum}) may be stimulated electrically (EL) or optically (PL). While a voltage V_{appl} is applied to the solar cell for the electrical stimulation, the optical stimulation is performed by illumination of the sample with monochromatic light (γ_{imp}). The electrical or optical stimulation of the semiconductor generates excess charge carriers (e^- and p^+), which may consequently recombine radiatively under the generation of a luminescence photon (γ_{lum}). Since the generated luminescence photons are send isotropically in all directions, only a small fraction reaches the front surface and is emitted from the surface element A_E [cm^{-2}] in direction to the detector. In a camera-based setup, as shown in Fig. 3.1, the size of A_E is determined by the used optics and the size of one pixel.

In this first section, I focus on the *generation* of luminescence photons within a small volume V of the semiconductor device. I discuss the refractive index and the absorption coefficient of silicon, relate the luminescence photon generation to the black body radiation and analyze the spectral coefficient of radiative recombination. Consequently, this allows me to derive an

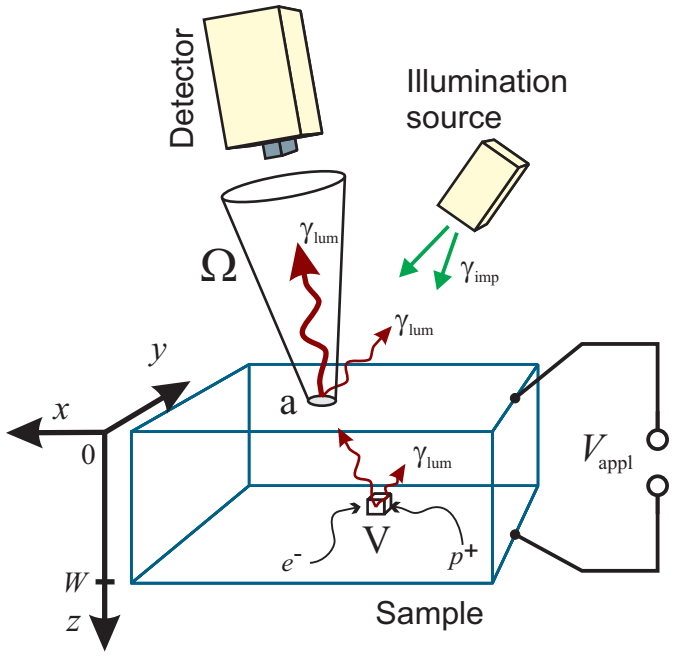

Figure 3.1: *Luminescence imaging detection geometry. Electrons (e^-) and holes (p^+) are generated electrically (V_{appl}) or optically (γ_{imp}). They may recombine radiatively under emission of a luminescence photon (γ_{lum}).*

expression of the luminescence photon *emission* from the sample's surface which depends on the excess charge carrier distribution within the solar cell's base and an emission probability for each generated luminescence photon.

3.2 Luminescence photon generation inside the solar cell

3.2.1 Radiative recombination

The radiative recombination of an electron (e^-) and a hole (p^+) results in the generation of a luminescence photon (γ_{lum}). Thus, the total generation rate G_{ph} [$\mathrm{cm^{-3}s^{-1}}$] of luminescence photons equals the rate R_{rad} [$\mathrm{cm^{-3}s^{-1}}$] of radiative recombination,

$$G_{\mathrm{ph}} = R_{\mathrm{rad}} = B_{\mathrm{rad}}\, n\, p. \tag{3.1}$$

Here B_{rad} [$\mathrm{cm^3s^{-1}}$] is the integral coefficient of radiative recombination and n [$\mathrm{cm^{-3}}$] and p [$\mathrm{cm^{-3}}$] are the electron and hole densities. B_{rad} is obtained by

$$B_{\mathrm{rad}} = C_{\mathrm{eh}}\, B_{\mathrm{low}}, \tag{3.2}$$

where B_{low} [$\mathrm{cm^3s^{-1}}$] is the integral coefficient of radiative recombination obtained at low carrier densities and C_{eh} is a factor which accounts for the enhanced probability of finding an electron and a hole in the immediate vicinity of each other.[50] B_{low} follows by integrating the spectral radiative recombination coefficient $b_{\mathrm{low}}(\lambda)$ [$\mathrm{cm^2s^{-1}}$] over the entire spectrum,

$$B_{\mathrm{low}} = \int_0^\infty d\lambda\, b_{\mathrm{low}}(\lambda). \tag{3.3}$$

b_{low} thus also defines the spectral luminescence photon generation rate g_{ph} [$\mathrm{cm^{-4}s^{-1}}$],

$$g_{\mathrm{ph}}(\lambda) = C_{\mathrm{eh}}\, b_{\mathrm{low}}(\lambda)\, n\, p, \tag{3.4}$$

which I will use in the next section to derive the spectral luminescence photon emission from the solar cell surface.

Van Roosbroeck[51] demonstrated that the rate of radiative recombination directly follows from the principle of detailed balance. This principle states that the spectral rate of radiative recombination at thermal equilibrium for an elementary wavelength interval $d\lambda$ at wavelength λ is equal to the corresponding rate of generation of electron-hole pairs by thermal radiation. Thus, van Roosbroeck obtained for the rate of radiative recombination for nondegenerate occupancies of the bands ($h\,\nu \gg k\,T$)

$$\begin{aligned} R_{\mathrm{rad}} &= \int_0^\infty d\nu\, \frac{32\pi^2\,\kappa\, n_{\mathrm{Si}}^2}{c_0^2} \cdot \nu^3\, \exp\left(-\frac{h\,\nu}{k\,T}\right) \\ &= \int_0^\infty d\lambda\, 4\pi\, \frac{2\,c_0\, n_{\mathrm{Si}}^2}{\lambda^4} \cdot \alpha\, \exp\left(-\frac{h\,c_0}{\lambda\, kT}\right), \end{aligned} \tag{3.5}$$

with the photon's frequency $\nu = c_0/\lambda$ (and thus $|d\nu| = |d\lambda|\, c_0/\lambda^2$) and the absorption index $\kappa = \alpha\,\lambda/(4\pi\, n_{\mathrm{Si}})$. n_{Si} is the refractive index of silicon, c_0 [$\mathrm{m/s}$] the speed of light in vacuum and α [$\mathrm{cm^{-1}}$] the absorption coefficient. With Eqs. (3.1) to (3.5) I determine the spectral coefficient of radiative recombination,

$$b_{\mathrm{low}}(\lambda)\, d\lambda = 4\pi\, \frac{2\,c_0}{\lambda^4}\, \frac{n_{\mathrm{Si}}^2}{n_{\mathrm{i}}^2}\, \alpha\, \exp\left(-\frac{h\,c_0}{\lambda\, kT}\right) d\lambda, \tag{3.6}$$

Table 3.1: *Overview of rates, photon fluxes and coefficients used in this section.*

	Unit	Description
R_{rad}	$[\mathrm{cm}^{-3}\mathrm{s}^{-1}]$	Rate of radiative recombination per volume and time.
G_{ph}	$[\mathrm{cm}^{-3}\mathrm{s}^{-1}]$	Generation rate of luminescence photons per volume and time.
g_{ph}	$[\mathrm{cm}^{-4}\mathrm{s}^{-1}]$	Spectral generation rate of luminescence photons per volume, time and wavelength interval.
B_{rad}	$[\mathrm{cm}^{3}\mathrm{s}^{-1}]$	Integral radiative recombination coefficient at arbitrary carrier densities.
B_{low}	$[\mathrm{cm}^{3}\mathrm{s}^{-1}]$	Integral radiative recombination coefficient at low carrier densities.
b_{low}	$[\mathrm{cm}^{2}\mathrm{s}^{-1}]$	Spectral radiative recombination coefficient at low carrier densities.
ϕ_{bb}	$[\mathrm{cm}^{-3}\mathrm{s}^{-1}\mathrm{sr}^{-1}]$	Planck's black body photon flux density per volume, time and solid angle.

written in terms of wavelengths.[a] In the latter equation, n_{i} $[\mathrm{cm}^{-3}]$ is the intrinsic carrier density.

The spectral coefficient of radiative recombination can be written in a more simple manner by using Planck's law describing the black body photon flux density,[53]

$$\phi_{\mathrm{bb}}(\lambda)\,d\lambda = \frac{2\,c_0}{\lambda^4}\exp\left(-\frac{h\,c_0}{\lambda\,kT}\right)\,d\lambda. \tag{3.7}$$

ϕ_{bb} $[\mathrm{cm}^{-3}\mathrm{s}^{-1}\mathrm{sr}^{-1}]$ in the latter equation is a photon flux density and gives the number of emitted photons in the wavelength interval $d\lambda$ per volume, solid angle and time.[b] Using ϕ_{bb} in Eq. (3.6) yields

$$b_{\mathrm{low}}(\lambda)\,d\lambda = 4\pi\,\frac{n_{\mathrm{Si}}^2}{n_{\mathrm{i}}^2}\,\alpha\,\phi_{\mathrm{bb}}\,d\lambda. \tag{3.8}$$

Note that the multiplication with 4π in the latter equation transforms the photon flux density per solid angle into a spherical photon flux density. For convenience, the different rates, photon fluxes and coefficients used in this section are summarized in Tab. 3.1.

[a] For the conversion I used the thermal equilibrium, $C_{\mathrm{eh}} = 1$ and $n \cdot p = n_{\mathrm{i}}^2$. Note that in this context I splitted the luminescence photon generation rate for an excited semiconductor in the terms b_{low} and $n\,p$, as indicated in Eq. (3.1). A fully thermodynamical treatment of the spectral luminescence photon generation rate of an excited semiconductor was carried out by Würfel,[52] who introduced the chemical potential for photons and thus was able to describe the emission spectra of non-thermal radiation.

[b] ϕ_{bb} as defined in Eq. (3.7) can be visualized as follows: A black body of volume V $[\mathrm{cm}^3]$ at a certain temperature T emits radiation in all directions. Spanning a sphere S around the volume and counting all photons of wavelength λ passing S gives a total of $4\pi \cdot \phi_{\mathrm{bb}}(\lambda) \cdot V$ photons per second (4π is the size of a unit sphere).

Wavelength-dependence of the refractive index, the absorption coefficient and the black body radiation

The refractive index $n_{\mathrm{Si}}(\lambda)$, the absorption coefficient $\alpha(\lambda)$ and the black body photon flux $\phi_{\mathrm{bb}}(\lambda)$ are the wavelength-dependent parameters of Eq. (3.8). Regarding luminescence imaging, especially the properties of the absorption edge of silicon is of main interest. This corresponds to the wavelength range from 900 nm to 1400 nm.

The refractive index n_{Si} relates the velocity of light within silicon to the velocity of light in vacuum. At room temperature n_{Si} decreases from 3.62 at 900 nm to 3.49 at 1400 nm.[54] In comparison to the parameters α and ϕ_{bb}, described in the following, the wavelength-dependence of n_{Si} in the relevant wavelength-range is negligible.

The absorption coefficient α together with Lambert-Beer's law [see i. e. Eq. (4.13)] determine how far light, of a particular wavelength, can penetrate into a material before it is absorbed. Several mechanisms contribute to this absorption of photons in silicon. In the visible range of the spectrum, the most dominant effect is the band-to-band absorption (absorption coefficient α_{b2b}), which is the basic process for semiconductor-based photovoltaics. Photons with energies above the band gap generate excess carriers by lifting electrons from the valence to the conduction band. Silicon is an indirect band gap semiconductor. Thus, the band-to-band absorption process is phonon-assisted resulting in a low absorption coefficient compared to direct band gap semiconductors.[55,56] Several authors[54,57–59] determined experimentally the absorption coefficient of silicon. Figure 3.2 shows the widely accepted data (red data) published by Keevers and Green.[55,57] It demonstrates that the absorption coefficient α is strongly dependent of the photon's wavelength. It decreases within the shown wavelength interval in the order of nine magnitudes and thus has a strong impact on the generation of luminescence photons [see Eq. (3.6)].

The black body photon flux density ϕ_{bb} gives the number of photons per wavelength interval which a black body emits at a specific temperature. Figure 3.2 shows ϕ_{bb} (green solid line) as calculated with Eq. (3.7) for a temperature of 300 K. It demonstrates that ϕ_{bb} increases within the relevant wavelength interval in the order of four magnitudes.

3.2.2 Spectral coefficient of radiative recombination

The resulting distribution of the coefficient of radiative recombination $b_{\mathrm{low}}(\lambda)$, given by Eq. (3.8), is shown in Fig. 3.3. $b_{\mathrm{low}}(\lambda)$, and thus the generation of luminescence photons, increases exponentially for wavelengths up to 1000 nm. For these wavelengths b_{low} is mainly determined by ϕ_{bb} (see Fig. 3.2). For longer wavelengths the absorption coefficient α_{b2b} begins to weaken the increase until a maximum is obtained at about 1125 nm. b_{low} then decreases rapidly because the photons energy becomes smaller than the band gap of silicon.

3.2.3 Integral coefficient of radiative recombination

The area underneath the red curve in Fig. 3.3 represents [see Eq. (3.3)] the integral coefficient of radiative recombination B_{low} at low carrier densities. The integration of the data in Fig. 3.3 from

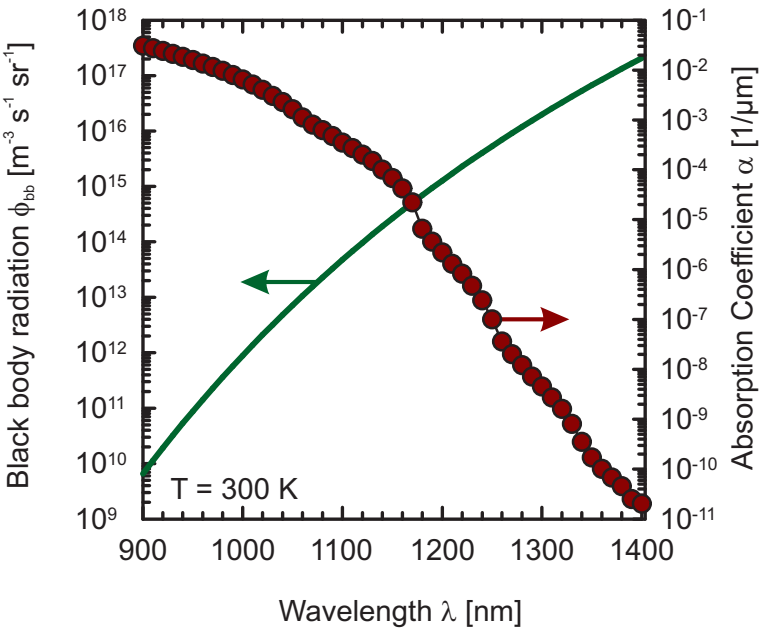

Figure 3.2: *Calculated black-body spectrum (green solid line) and absorption coefficient of silicon (red data) in the wavelength range relevant for luminescence imaging. The absorption data is taken from Ref. 57.*

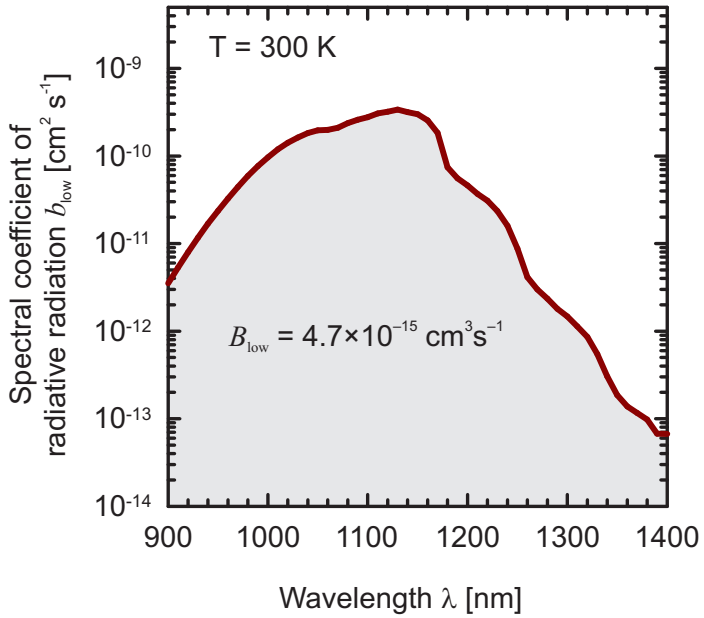

Figure 3.3: *Spectral coefficient of radiative recombination at low carrier densities.*

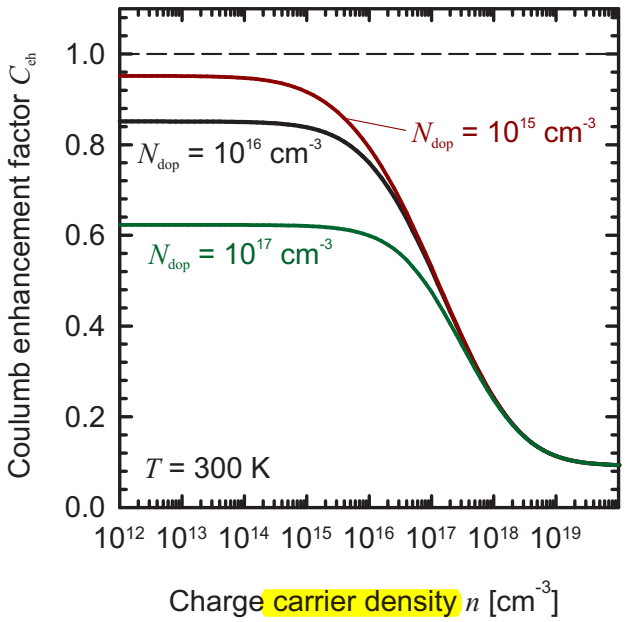

Figure 3.4: *Coulomb enhancement of the coefficient of radiative recombination.*

900 nm to 1400 nm yields[c]

$$B_{\text{low}} = 4.7 \times 10^{-15}\ \text{cm}^3\text{s}^{-1}. \tag{3.9}$$

This value is the same as given in Ref. 60, where the authors state that it is more reliable than previously published values.[61–64]

3.2.4 Coulomb enhancement of the coefficient of radiative recombination

The coefficient of radiative recombination B_{rad} is enhanced by the Coulomb attraction between electrons and holes, which leads to an increased hole density in the vicinity of an electron, and vice versa. This enhancement depends on both temperature[60,61] and carrier injection level;[50] it varies with the amount of screening among the free carriers. Figure 3.4 shows the calculated injection level dependence for 300 K using the parametrization of Altermatt et al.[65] In order to obtain the absolute values of B_{rad} from Fig. 3.4, the data needs to be multiplied with the value of B_{low} given in Eq. (3.9).

The data in Fig. 3.4 shows that the coefficient of radiative recombination declines with increasing hole or electron density or with increasing dopant density. However, for carrier density ranges well below the base dopant concentration, C_{eh} and thus B_{rad} do not depend on the injection level. For the examples shown in Fig. 3.4 this assumption holds for carrier densities one magnitude smaller than the dopant density.

[c] Note that the integration of the data can also be carried out over all wavelengths since b_{low} becomes negligibly small for wavelengths shorter than 900 nm and larger than 1400 nm.

3.3 Luminescence photon emission from the solar cell surface

The usual approach to describe the luminescence photon emission of one local surface element is to integrate the spectral luminescence photon generation rate g_{ph} [$\mathrm{cm}^{-4}\mathrm{s}^{-1}$] as defined in Eq. (3.4) over the depth W of the sample,

$$\varphi(\lambda)\, d\lambda = d\lambda \int_0^W dz\, f_{\mathrm{out}}\, b_{\mathrm{low}}(\lambda)\, C_{\mathrm{eh}}\, n\, p, \tag{3.10}$$

Here, $\varphi(\lambda)$ [$\mathrm{cm}^{-3}\mathrm{s}^{-1}$] gives the number of photons per time, per surface element and per wavelength interval. f_{out} is an emission probability for each luminescence photon generated at z (isotropical generation) to be emitted from the solar cell's surface into the solid angle of detection Ω. Ω is shown in Fig. 3.1 and is mainly determined by the used camera optics and the distance of the camera to the sample. The emission probability f_{out} accounts for internal reflections and reabsorption within the sample and is thus strongly dependent on z. Equation (3.10) has to be integrated over wavelength (i. e. the slit width of a spectrometer),

$$\Phi_{\mathrm{lum}}(\lambda) = \int_{\lambda_1}^{\lambda_2} d\lambda\, \varphi(\lambda), \tag{3.11}$$

to give $\Phi_{\mathrm{lum}}(\lambda)$ [$\mathrm{cm}^{-2}\mathrm{s}^{-1}$], the number of photons of wavelength λ ($\lambda_1 \leq \lambda \leq \lambda_2$) emerging from the surface per time and per surface element.

At first sight the luminescence integral defined in Eq. (3.10) only holds for planar surfaces. For textured surfaces the photons, which are emitted from the solar cell's surface in direction to the detector, have not necessarily been generated in the volume underneath the place of emission E. Contrarily, they might stem from different locations.

Three-dimensional ray-tracing programs (i. e. SunRays[66] or RaySim[67]) may account for all relevant optical effects of textured surfaces and programs based on finite element methods (FEM) can account for all electrical effects. However, these programs are still too time-consuming to allow for example a fitting of experimental data. In addition, an analytical description allows for a better understanding of the underlying effects.

In most practical cases a one-dimensional electrical model is sufficient to model transport mechanisms and carrier distribution within standard industrial silicon solar cells (see chapter 4). Thus, an one-dimensional optical model which allows the simulation and analysis of experimental data is much sought after. In chapter 5 of this work I show that the factor f_{out} is related to the absorption of impinging photons and thus is directly obtained from models developed i. e. for quantum efficiency analysis.

3.4 Solar cell structure analyzed in this work

I focus on the luminescence emission of crystalline silicon solar cells with a textured front surface. Without loss of generality I assume a p-doped base region of thickness W_{b} [$\mu\mathrm{m}$] and an n-doped emitter at the front side of thickness W_{e} [nm]. The contributions of thin but highly doped regions (i.e. emitter and back surface field) to the total luminescence emission is negligible.[7] This allows

to simplify the integral in Eq. (3.10) by restricting the bounds of integration to the base region of the device.

The product $n \cdot p$ in Eq. (3.10) is determined by

$$\begin{aligned} n(z) \cdot p(z) &= (n_0 + \Delta n(z)) \cdot (p_0 + \Delta n(z)) \\ &= n_0\, p_0 + \Delta n(z) \cdot (p_0 + n_0) + \Delta n(z)^2, \end{aligned} \tag{3.12}$$

where n_0 [cm^{-3}] and p_0 [cm^{-3}] are the thermally and Δn [cm^{-3}] and Δp [cm^{-3}] the stimulated (electrically or optically) excess electron and hole carrier concentrations, respectively.[d]

Assuming charge neutrality and room temperature ($n_0 \ll N_\mathrm{A}$), the term p_0 in Eq. (3.12) can be replaced by N_A [cm^{-3}], the dopant concentration of the base. For low-level injection ($\Delta n \ll N_\mathrm{A}$) and room temperature the product of electron and hole carrier densities, $n(z) \cdot p(z)$ in Eq. (3.12) further simplifies to

$$n(z) \cdot p(z) \xrightarrow{lli} \Delta n(z) \cdot N_\mathrm{A}. \tag{3.13}$$

In addition, within the low-level injection range, the Coulomb enhancement factor C_eh is in very good approximation independent of the excess charge carrier density [see Fig. 3.4 and Ref. 50] and thus independent of z.

By inserting the previous approximations into Eq. (3.10), I obtain

$$\varphi(\lambda)\, d\lambda = d\lambda, N_\mathrm{A}\, C_\mathrm{eh}\, b_\mathrm{low}(\lambda) \int_0^{W_\mathrm{b}} dz\, f_\mathrm{out}(z, \lambda)\, \Delta n(z) \tag{3.14}$$

as a good approximation.

3.5 Camera signal

The resulting φ, as given in the previous section, determines the luminescence photon flux per wavelength interval, which is emitted from the sample's surface into the detection cone Ω. These luminescence photons are then collected within one pixel of the camera. After a certain exposure time, the camera translates the collected luminescence photons into a camera signal S [counts]:

$$S = C_\mathrm{conv} \cdot t_\mathrm{exp} \cdot A_E \cdot \int_0^\infty d\lambda\, Q_\mathrm{cam}(\lambda)\, T_\mathrm{optics}(\lambda)\, \varphi(\lambda). \tag{3.15}$$

Here, C_conv [counts/eh] is the conversion factor from generated electron-hole pairs in the pixel to digital units or counts, t_exp is the exposure time, A_E is the size of the surface element which is imaged by one pixel, $Q_\mathrm{cam}(\lambda)$ accounts for the spectral quantum efficiency of the detector and $T_\mathrm{optics}(\lambda)$ is the transmittance of all optics in-between the sample and the detector itself, including filters and lenses.

[d] Note that the term $n_0 \cdot p_0$ always vanishes if the luminescence measurement is carried out with darkframe-subtraction.

3.6 Solving the luminescence integral

In accordance to Eq. (3.10), the calculation of the emitted luminescence photons from the solar cell surface in this work is carried out in three steps:

- First, I calculate charge carrier distributions $\Delta n(z)$ within the solar cell base for different working points (see chapter 4 for details).
- Second, I analyze the detection probability $f_{\mathrm{out}}(z)$ and modify the luminescence integral to accurately describe textured silicon solar cells (see chapter 5 for details).
- And third, I demonstrate the applicability of the derived equations by describing measured luminescence spectra. Regarding camera-based measurements, I explicitly carry out the integration of Eq. (3.14) to obtain analytical solutions for the photon flux emitted from the solar cell's front surface into the solid angle of detection (see chapter 6 for details).

CHAPTER 4

Charge carrier distributions within the solar cell base

For photoluminescence (PL) imaging, photons from the impinging flux $\Phi_{\mathrm{imp},0}$ are absorbed within the semiconductor and generate electron hole pairs. Contrarily, for electroluminescence (EL) imaging, the impinging photon flux is zero. In this case, charge carriers are injected into the solar cell base across the p-n junction by an applied voltage. For both cases (EL and PL) an equilibrium establishes between the generation (or injection) of charge carriers and the recombination (or extraction) at the surfaces and within the solar cell's base. As a result an excess charge carrier distribution $\Delta n(z)$ is obtained and the radiatively recombining charge carriers give rise to the luminescence photon generation.

4.1 Diffusion equation of charge carriers

4.1.1 Three dimensions

Fick's first law relates the dynamics of charge carriers to the gradient of their concentration field. It postulates that the flux diffuses from regions of high concentration to regions of low concentration, with a magnitude D that is proportional to the concentration gradient. In three dimensions, this is

$$\vec{J}(\vec{r}) = -D \nabla \left(\Delta n(\vec{r})\right), \tag{4.1}$$

where $\vec{J}\,[\mathrm{cm}^{-2}\mathrm{s}^{-1}]$ is the charge carrier flux passing the surface of a small volume element dV at a position $\vec{r}\,[\mathrm{cm}]$, $D\,[\mathrm{cm}^2\mathrm{s}^{-1}]$ the diffusivity of the charge carriers and $\Delta n\,[\mathrm{cm}^{-3}]$ the excess charge carrier concentration within dV.

In each volume element dV of the solar cell's base generation G and recombination R of electron-hole pairs occur. Under steady state conditions, the continuity equation describes the conversation of charge carriers within dV. Figure 4.1 illustrates this equation: The number of charge carriers $J_{in} + G$, entering the small volume dV, has to equal the number $J_{out} + R$, leaving

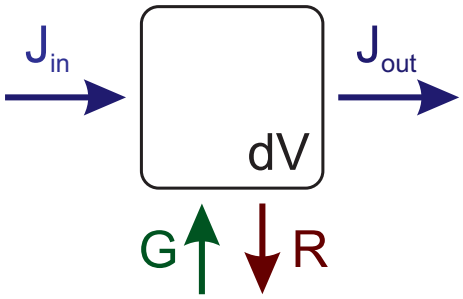

Figure 4.1: *Under steady state conditions, the continuity equation describes the conversation of charge carriers within dV: The number of charge carriers $J_{\mathrm{in}} + G$, entering the small volume dV, has to equal the number $J_{\mathrm{out}} + R$, leaving dV.*

dV. In three dimensions, the continuity equation reads

$$\nabla \vec{J}(\vec{r}) = G(\vec{r}) - R(\vec{r}), \tag{4.2}$$

where $G(\vec{r})$ [$\mathrm{cm^{-3}s^{-1}}$] and $R(\vec{r})$ [$\mathrm{cm^{-3}s^{-1}}$] denote the rates of electron-hole-pair optical generation and recombination, respectively. The recombination of excess charge carriers can be expressed by

$$R(\vec{r}) = \frac{\Delta n(\vec{r})}{\tau(\vec{r})}, \tag{4.3}$$

where $\tau(\vec{r})$ [s] denotes the charge carrier lifetime at the position $\vec{r}$. Inserting Eq. (4.3) and Eq. (4.1) into Eq. (4.2) one obtains

$$D\,\nabla^2\left(\Delta n(\vec{r})\right) - \frac{\Delta n(\vec{r})}{\tau(\vec{r})} = -G(\vec{r}), \tag{4.4}$$

a differential equation describing the diffusion of excess charge carriers inside the solar cell's base.

4.1.2 One dimension

In order to calculate an analytical solution of the one-dimensional minority charge carrier distribution $\Delta n(z)$ within the solar cell's base I neglect any lateral diffusion perpendicular to the axis z. The diffusion equation in Eq. (4.4) then becomes

$$\Phi_{\mathrm{imp,0}}\left(1 - R_{\mathrm{f}}\right) g_{\mathrm{eh}}(z) - \frac{D\,\Delta n(z)}{L_{\mathrm{b}}^2} + D\,\frac{d^2\Delta n(z)}{dz^2} = 0. \tag{4.5}$$

Here, D [$\mathrm{cm^2s^{-1}}$] is the diffusion constant, $L_{\mathrm{b}} = \sqrt{D\,\tau}$ [µm] the bulk diffusion length, $\Phi_{\mathrm{imp,0}}$ [$\mathrm{cm^{-2}s^{-1}}$] the impinging photon flux at the outer surface of the sample which is reduced by the external reflectance R_{f} at the surface and $g_{\mathrm{eh}}(z)$ [$\mathrm{cm^{-1}}$] the normalized, one-dimensional

generation profile of excess charge carriers. $g_{\mathrm{eh}}(z)$ describes the rate $G_{\mathrm{eh}}(z)$ [$\mathrm{cm^{-3}s^{-1}}$] of optical electron-hole-pair generation per time and per volume,

$$g_{\mathrm{eh}}(z) = \frac{G_{\mathrm{eh}}(z)}{\Phi_{\mathrm{imp,0}}\,(1 - R_{\mathrm{f}})}, \tag{4.6}$$

normalized to the impinging photon flux entering the base, $\Phi_{\mathrm{imp,0}} \cdot (1 - R_{\mathrm{f}})$. Note that while $\Phi_{\mathrm{imp,0}}$ in Eq. (4.5) and Eq. (4.6) describes the impinging photon flux at the outer surface of an external illumination (i. e. a lamp), Φ_{lum} [see for example Eq. (3.14)] gives the emitted photon flux of luminescence photons generated inside the semiconductor.

4.2 Boundary conditions of the diffusion equation

The luminescence emission of a solar cell can either be stimulated electrically (electroluminescence, EL) or optically (photoluminescence, PL). In both cases, a specific working point (wp) is defined by applying a voltage V_{appl}. While an applied voltage always leads to a current injection in the EL case, PL measurements up to the open circuit voltage leads to a current extraction. In the following, I analyze the excess charge carrier distributions of all possible EL and PL operation conditions. In principle, PL at an applied voltage (PL-wp) describes the excess charge carrier distribution from the short-circuit ($V_{\mathrm{appl}} = 0$) to the open-circuit ($V_{\mathrm{appl}} = V_{\mathrm{oc}}$) case. However, for the latter two cases, specific boundary conditions simplify the equations. For a better understanding, the PL derivations in this section are split up into photoluminescence at short-circuit conditions (PL-sc), photoluminescence at an applied voltage (PL-wp) and photoluminescence at open-circuit conditions (PL-oc).

Each operation condition (EL, PL-sc, PL-wp and PL-oc) leads to certain boundary conditions which have to be considered in the differential equation given in Eq. (4.5):

- The generation profile $g_{\mathrm{eh}}(z)$ for the non-illuminated case (EL) is zero. For PL-sc, PL-wp and PL-oc instead, the solar cell is illuminated with monochromatic light with a specific wavelength λ_{imp} [nm]. For the experimental setup presented in chapter 2 the illumination is carried out using a semiconductor laser with a wavelength of $810\ \mathrm{nm}$ which implies an absorption length of $13\ \mu\mathrm{m}$ in silicon. For absorption lengths much shorter than the device thickness it is allowed to use a simplified generation profile

  $$g_{\mathrm{eh},1}(z) = \frac{\alpha_{\mathrm{imp}}}{\cos\theta_1} \exp\left(\frac{-\alpha_{\mathrm{imp}}\, z}{\cos\theta_1}\right), \tag{4.7}$$

  which I will explain in more detail in section 4.3. α_{imp} in Eq. (4.7) is the absorption coefficient of the impinging photons in silicon and θ_1 denotes the angle of refraction of the impinging photons due to a textured surface.

- At $z = 0$ the charge carrier concentration is pinned by the externally applied voltage to a defined value for the EL, the PL-sc and the PL-wp case. This results in the boundary condition[68]

  $$n_1 = \frac{n_{\mathrm{i}}^2}{N_{\mathrm{A}}} \exp\left(\frac{V_i}{V_{\mathrm{T}}}\right), \tag{4.8}$$

Table 4.1: *Boundary conditions of the diffusion equation for the EL, PL-sc, PL-wp and PL-oc operation conditions. The generation profile $g_{\mathrm{eh}}(z)$ does only hold for impinging photons with wavelengths smaller than 850* nm. *At the rear surface ($z = W_{\mathrm{b}}$) the boundary condition for all operation conditions reads $S_{\mathrm{rear}}\Delta n(W_{\mathrm{b}}) = -D\,\Delta n'(W_{\mathrm{b}})$.*

	$z = 0$	$g_{\mathrm{eh}}(z)\vert_{\lambda_{\mathrm{imp}}}$
EL	$n_1 = \frac{n_{\mathrm{i}}^2}{N_{\mathrm{A}}}\exp(\frac{V_i}{V_{\mathrm{T}}})$	0
PL-sc	$n_1 = 0$	$\frac{\alpha_{\mathrm{imp}}}{\cos\theta_1}\exp(-\frac{z\,\alpha_{\mathrm{imp}}}{\cos\theta_1})$
PL-wp	$n_1 = \frac{n_{\mathrm{i}}^2}{N_{\mathrm{A}}}\exp(\frac{V_i}{V_{\mathrm{T}}})$	$\frac{\alpha_{\mathrm{imp}}}{\cos\theta_1}\exp(-\frac{z\,\alpha_{\mathrm{imp}}}{\cos\theta_1})$
PL-oc	$S_{\mathrm{eff}}\Delta n(0) = D\,\Delta n'(0)$	$\frac{\alpha_{\mathrm{imp}}}{\cos\theta_1}\exp(-\frac{z\,\alpha_{\mathrm{imp}}}{\cos\theta_1})$

where V_i is the local junction voltage,[a] V_{T} is the thermal voltage, n_{i} is the intrinsic carrier concentration, N_{A} is the base dopant concentration and $n_1 = \Delta n(0)$ [cm^{-3}] is the excess carrier density at $z = 0$. For PL-sc, the applied voltage at $z = 0$ is zero, implying $n_1 = 0$. For PL-oc, a different boundary condition is required, which I explain in the next section (Sec. 4.2.1).

- At $z = W_{\mathrm{b}}$ the recombination current due to the rear surface recombination velocity S_{rear} must equal the diffusion current,

$$S_{\mathrm{rear}}\Delta n(W_{\mathrm{b}}) = -D\frac{d}{dz}\Delta n(z)\big|_{z=W_{\mathrm{b}}}. \tag{4.9}$$

  The latter boundary condition is identical for all operation conditions investigated in this work (EL, PL-sc, PL-wp and PL-oc).

All boundary conditions are summarized in Tab. 4.1.

4.2.1 Photoluminescence at open-circuit conditions

The open-circuit condition differs from EL, PL-sc and PL-wp since the local voltage and thus the carrier concentration at the beginning of the base ($z = 0$) is not pinned to a defined value by an applied voltage. Even though no current is intentionally extracted or fed-in at $z = 0$, the impact of parasitic current losses has to be taken into account. These parasitic current losses include for example recombination within the space-charge region, within the volume of the emitter, at the front surface, at shunt resistances and beneath the metal contacts. And even worse, parasitic current losses localized in the vicinity of the investigated region may have an impact on PL-oc since all regions are interconnected by the emitter.

My approach for an analytical description is to lump all possible current losses into an effective surface recombination velocity S_{eff} [$\mathrm{cm/s}$] acting at the front of the base ($z = 0$). The

[a] The local junction voltage is discussed in more detail in Sec. 7.1.2, where also Eq. (4.8) is explicitly derived.

PL-oc case is thus an equilibrium between the current extraction due to S_{eff} and the diffusion current provided from the volume of the base,

$$S_{\mathrm{eff}} \Delta n_{\mathrm{oc}}(0) = D \, \frac{d}{dz} \Delta n_{\mathrm{oc}}(z)|_{z=0}, \tag{4.10}$$

similarly as for the rear surface in Eq. (4.9).

The PL-oc case applies not only to silicon solar cells but also to silicon wafers, where the effective surface recombination velocity S_{eff} corresponds to the front surface recombination velocity of the wafer.

4.3 Generation profile of charge carriers for optical excitation

Assuming that each electron-hole pair corresponds to one absorbed photon, the generation rate $G_{\mathrm{eh}}(z)$ is a direct measure for the change of the photon flux $\Phi_{\mathrm{imp}}(z)$ passing the medium,

$$G_{\mathrm{eh}}(z) = -\frac{d}{dz}\Phi_{\mathrm{imp}}(z). \tag{4.11}$$

Using the latter equation in Eq. (4.6) gives the normalized generation profile as

$$g_{\mathrm{eh}}(z) = -\frac{1}{\Phi_{\mathrm{imp},0}\,(1-R_{\mathrm{f}})}\cdot\frac{d}{dz}\Phi_{\mathrm{imp}}(z). \tag{4.12}$$

Lambert-Beer's law for the impinging photon flux in one dimension reads

$$\Phi_{\mathrm{imp}}(z) = \Phi_{\mathrm{imp},0}\,(1-R_{\mathrm{f}})\cdot\exp\left(-\alpha_{\mathrm{imp}}\,z\right). \tag{4.13}$$

Thus, for a planar solar cell and short-wavelength photons the generation profile

$$g_{\mathrm{eh}}(z)|_{\mathrm{planar,short}} = \alpha_{\mathrm{imp}}\,\exp\left(-\alpha_{\mathrm{imp}}\,z\right) \tag{4.14}$$

directly follows.

The difficulty to derive the generation profile of charge carriers lies in silicon devices featuring an optical confinement like a textured front surface or a highly reflecting rear surface. A textured surface refracts any incoming photons which consequently travel inside the semiconductor with a direction different to that of the illumination. Due to a highly reflecting rear surface photons exhibiting absorption lengths longer than the base thickness (above $900\ \mathrm{nm}$ for $200\ \mu\mathrm{m}$ thick solar cells) are reflected back into the solar cell device after hitting the rear surface. The photon thus may travel various times between the front and the rear surface until being finally absorbed or re-emitted from the surface. Due to an optical confinement, the photon path inside the solar cell becomes a function of the topography of the rear and the front surface as well as the wavelength of the photons. Figure 4.2 illustrates such a photon path for a solar cell featuring a textured front surface and a partly rough rear surface. The illumination is performed at H_1 in a certain angle to the front surface. The impinging photons are refracted at the textured surface and propagate from the front surface to the rear surface with an angle θ_1. The long-wavelength photon propagation (photons which are not absorbed within the first pass) is shown in Fig. 4.2 using the angles θ_2 and θ_n. In this figure, the photon is finally absorbed within a volume V, where consequently an electron-hole pair is generated.

4.3.1 Literature solution

A complete description of $g_{\mathrm{eh}}(z)$, which accounts for an infinite number of reflectances and holds for textured surfaces, was originally introduced by Basore[69] and was later extended by Brendel et al.[70] with an improved description of long-wavelength photons in thin-layer silicon solar cells. As the model in Ref. 70 is designed to describe thin-film solar cells, generation in the emitter is explicitly considered. For industrial crystalline silicon solar cells, for which the thickness W_{b}

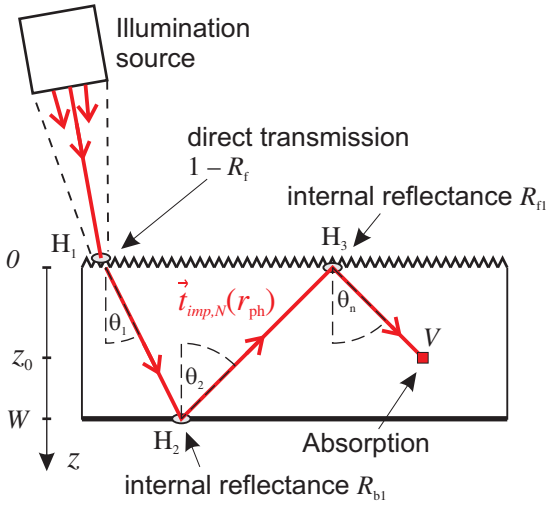

Figure 4.2: *Light propagation within a silicon device featuring a textured front surface and optical confinement.*

of the base is much greater than the thickness W_e of the emitter, the model can be simplified by using only the base contribution. The one-dimensional generation profile reads [see Ref. 70]

$$\begin{aligned} g_{eh}(z) = & \frac{\alpha_{imp}}{\cos\theta_1} \exp\left(\frac{-\alpha_{imp} z}{\cos\theta_1}\right) + \\ & \frac{\alpha_{imp}}{\cos\theta_2} T_1 R_{b1} \exp\left(\frac{-\alpha_{imp}(W_b - z)}{\cos\theta_2}\right) + \\ & \frac{\alpha_{imp}}{\cos\theta_n} \cdot T_1\, R_{b1}\, T_2\, R_{fl} \frac{1}{1 - T_n^2 R_{fn} R_{bn}} \times \\ & \left[\exp\left(\frac{-\alpha_{imp} z}{\cos\theta_n}\right) + T_n R_{bn} \exp\left(\frac{-\alpha_{imp}(W_b - z)}{\cos\theta_n}\right)\right], \end{aligned} \tag{4.15}$$

where α_{imp} is the absorption coefficient in silicon of the impinging photons of wavelength λ_{imp}. As shown in Fig. 4.2, the parameters θ_1, θ_2 and θ_n give the angles of light propagation, where the indexes 1, 2 and n denote the corresponding pass or surface hit of the photon propagation within the solar cell. R_{fl} and R_{fn} give the internal reflectance at the front surface, R_{b1} and R_{bn} give the internal reflectance at the rear surface and the transmittances T_1, T_2 and T_n describe the transmission of the i-th pass through the base. Details of how the different θ_i- and T_i-values are determined can be found in Ref. 70 and in the appendix A of this work.

Generation profile examples

Figure 4.3 exemplarily shows resulting generation profiles for the wavelengths 800 nm, 860 nm, 930 nm and 1000 nm. The generation profiles are calculated for a solar cell with a textured front surface ($\theta_1 = 41°$), a base thickniss of 200 µm and a diffusely reflecting rear with a reflectance

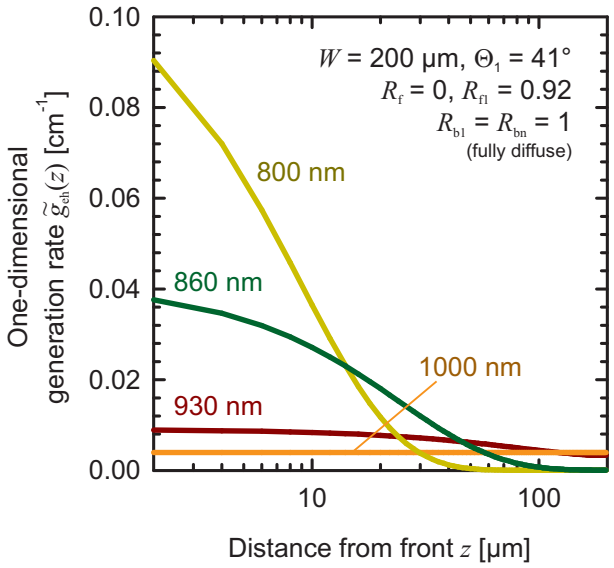

Figure 4.3: *Calculated generation profiles of four different wavelengths.*

of one ($R_\mathrm{b} = 1$). The x-axis is shown in a logarithmic scale for a better visualization of the generation close to the front surface.

The figure demonstrates that for short wavelength photons (high absorbtion) the generation of charge carriers mostly occurs close to the front surface. For these wavelengths the generation profiles rapidly decrease towards zero and all photons are absorbed before they reach the rear surface. Instead, for longer wavelength photons, the generation close to the front surface is smaller and the decrease towards the rear is less pronounced or is absent for very long wavelengths (very low absorbtion).

4.3.2 Simplification of the generation profile for the used experimental setup

For the setup used in this work ($\lambda_\mathrm{imp} = 810\ \mathrm{nm}$) and for solar cells with a thickness of about $200\ \mu\mathrm{m}$, the generation profile given in Eq. (4.15) simplifies substantially because of the strong photon absorption within the first micrometers. Reflections of impinging photons at the rear of the solar cell do not appear in this limit because for the used illumination wavelength only a negligible fraction of photons reaches the rear surface (see Fig. 4.3),

$$\exp\left(-\frac{\alpha_\mathrm{imp} W_\mathrm{b}}{\cos\theta_1}\right) \xrightarrow[W_\mathrm{b}\geq 100\ \mu\mathrm{m}]{\alpha_\mathrm{imp}=0.077\ \mu\mathrm{m}^{-1}} 0, \tag{4.16}$$

and consequently $T_1 \to 0$ follows. The normalized generation profile in this limit reads

$$g_{\mathrm{eh},1}(z) = \frac{\alpha_\mathrm{imp}}{\cos\theta_1} \exp\left(\frac{-\alpha_\mathrm{imp}\, z}{\cos\theta_1}\right) \tag{4.17}$$

and will be used to solve the differential equation [see Eq. (4.5)] for PL imaging. Nevertheless, the complete solution of the generation profile given in Eq. (4.15) is of upmost importance since it forms the base for the description of the emission probability f_out, as I will show in chapter 5.

4.4 Solutions for the diffusion equation

4.4.1 Electroluminescence

As a result of the boundary conditions [see Tab. 4.1] and the diffusion equation [see Eq. (4.5)] I obtain for the EL carrier distribution

$$\Delta n_{\mathrm{drk}}(z) = n_1 \cdot \left[\cosh\left(\frac{z}{L_\mathrm{b}}\right) - \frac{L_\mathrm{b}}{L_\mathrm{eff}} \sinh\left(\frac{z}{L_\mathrm{b}}\right)\right], \tag{4.18}$$

which is the well-known dark carrier distribution. Here, the effective diffusion length reads

$$L_\mathrm{eff} = L_\mathrm{b} \frac{L_\mathrm{b}\, S_\mathrm{rear} \sinh\left(\frac{W_\mathrm{b}}{L_\mathrm{b}}\right) + D \cosh\left(\frac{W_\mathrm{b}}{L_\mathrm{b}}\right)}{L_\mathrm{b}\, S_\mathrm{rear} \cosh\left(\frac{W_\mathrm{b}}{L_\mathrm{b}}\right) + D \sinh\left(\frac{W_\mathrm{b}}{L_\mathrm{b}}\right)} \tag{4.19}$$

and describes the solar cell's base recombination current[69,71] expressed by the bulk diffusion length L_b and the rear surface recombination velocity S_rear.

4.4.2 Photoluminescence at short-circuit conditions

In the PL-sc case the resulting carrier distribution is

$$\Delta n_{\mathrm{sc}}(z) = \Phi_{\mathrm{imp},0} \cdot \frac{(1-R_\mathrm{f})}{D} \cdot \frac{\cos(\theta_1)}{\alpha_\mathrm{imp}} \cdot \left[\frac{\Delta n_{\mathrm{drk}}(z)}{n_1} - \exp\left(-\frac{\alpha_\mathrm{imp} z}{\cos\theta_1}\right)\right]. \tag{4.20}$$

The latter equation was approximated by

$$\exp\left(-\frac{\alpha_\mathrm{imp}\, W_\mathrm{b}}{\cos\theta_1}\right) \ll 1 \tag{4.21}$$

and

$$\left(\frac{\cos\theta_1}{\alpha_\mathrm{imp}\, L_\mathrm{b}}\right)^2 \ll 1. \tag{4.22}$$

Using this approximation, numerous additive terms could be neglected and a compact analytical description of the PL-sc carrier distribution was obtained in Eq. (4.20). In the next chapter, this simplified carrier distribution allows me to solve the luminescence integral analytically and thus parameter dependences of the luminescence emission can be demonstrated easily.

The approximations of Eq. (4.21) and Eq. (4.22) hold for solar cells with a base thickness of more than $150\ \mu\mathrm{m}$, an impinging photon flux of $810\ \mathrm{nm}$ ($\alpha_\mathrm{imp} = 0.077\ \mu\mathrm{m}^{-1}$), and a bulk diffusion length L_b of more than $100\ \mu\mathrm{m}$. I demonstrate in Sec. 4.5.2 by a comparison to charge carrier distributions obtained using the numerical device simulator PC1D,[72] that the error introduced due to the approximations in Eq. (4.21) and Eq. (4.22) is below $4\ \%$ for an impinging wavelength of $810\ \mathrm{nm}$.

4.4.3 Photoluminescence at working-point conditions

Even though possible, I don't explicitly calculate the PL-wp case here. Instead, I utilize a fundamental superposition principle[73–75] stating that the carrier distribution inside the base at an arbitrary working point (the solar cell is illuminated and held at a specific voltage) is the sum of the dark carrier and the short circuit carrier distribution,

$$\Delta n_{\mathrm{wp}}(z, \lambda_{\mathrm{imp}}) = \Delta n_{\mathrm{drk}}(z, \lambda_{\mathrm{imp}}) + \Delta n_{\mathrm{sc}}(z, \lambda_{\mathrm{imp}}). \tag{4.23}$$

This superposition principle is directly represented in the diffusion equation [Eq. (4.5)], which is a linear differential equation. The dark case [$g_{\mathrm{eh}}(z) = 0$] gives the homogeneous solution and the short circuit case is one particular solution.

4.4.4 Photoluminescence at open-circuit conditions

Using the approximations introduced in Eq. (4.21) and Eq. (4.22) a simple analytical form

$$\Delta n_{\mathrm{oc}}(z) = \Phi_{\mathrm{imp},0} \cdot \frac{(1 - R_{\mathrm{f}})}{D} \cdot \frac{\cos\theta_1}{\alpha_{\mathrm{imp}}} \cdot \left[\frac{K\, L_{\mathrm{eff}}\, \alpha_{\mathrm{imp}}}{\cos\theta_1} \cdot \frac{\Delta n_{\mathrm{drk}}(z)}{n_1} - \exp\left(-\frac{z\, \alpha_{\mathrm{imp}}}{\cos\theta_1} \right) \right] \tag{4.24}$$

is also obtained for the excess charge carrier distribution at open-circuit conditions. Here, the parameter

$$K = \frac{1 + \frac{S_{\mathrm{eff}}}{D} \frac{\cos\theta_1}{\alpha_{\mathrm{imp}}}}{1 + \frac{S_{\mathrm{eff}}}{D} L_{\mathrm{eff}}} \tag{4.25}$$

was introduced, where S_{eff} is the effective front surface recombination velocity acting at the beginning of the base as defined in Eq. (4.10).

The comparison of the analytical PL-oc carrier distribution in Eq. (4.24) to the numerical device simulator PC1D in Sec. 4.5.2 demonstrates that the error introduced due to the approximations in Eq. (4.21) and Eq. (4.22) is below $1\ \%$ for an impinging wavelength of $810\ \mathrm{nm}$.

Note that applying the approximations of Eq. (4.21) and Eq. (4.22) to the more general approach of Duggan et al.,[76] which describes the minority carrier distribution of thin non-diffused epitaxial layers under optical excitation, gives consistent results.

4.4.5 Transformation PL-oc to PL-sc

The PL-sc carrier distribution is a limit of the PL-oc solution. For PL-sc, all excess electrons at $z = 0$ are extracted, giving the boundary condition $\Delta n_{\mathrm{sc}}(0) = 0$. This boundary condition is expressed equally by an infinite effective surface recombination velocity, $S_{\mathrm{eff}} \to \infty$. Hence, the factor K for PL-sc is

$$K_{\mathrm{sc}} = \lim_{S_{\mathrm{eff}} \to \infty} K = \frac{\cos\theta_1}{\alpha_{\mathrm{imp}}\, L_{\mathrm{eff}}}. \tag{4.26}$$

Inserting the latter equation into Eq. (4.24) is consistent to the result of Eq. (4.20).

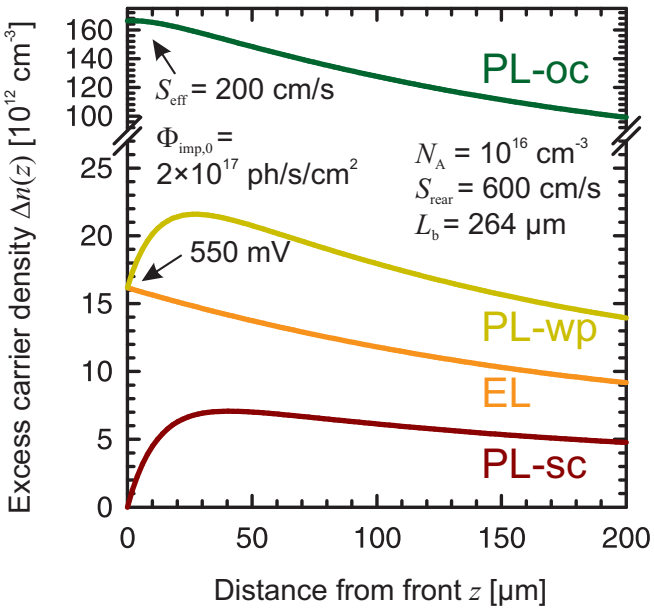

Figure 4.4: *Excess charge carrier densities within the base of a solar cell for EL, PL-sc, PL-wp and PL-oc conditions.*

4.5 Calculations and simulations of charge carrier distributions

4.5.1 Simulation of charge carrier distributions

The excess charge carrier distributions for EL, PL-sc, PL-wp and PL-oc as given by Eq. (4.20), Eq. (4.18), Eq. (4.23) and Eq. (4.24), respectively, are calculated for a solar cell which exhibits a bulk diffusion length of $264\ \mu\mathrm{m}$, a rear surface recombination velocity of $600\ \mathrm{cm/s}$, an effective front surface recombination velocity of $200\ \mathrm{cm/s}$[b] and a base dopant density of $10^{16}\ \mathrm{cm}^{-3}$. Excess charge carriers are generated optically by monochromatic light ($810\ \mathrm{nm}$, as used in our experimental setup presented in chapter 2) of $2 \cdot 10^{17}\ \mathrm{ph/s/cm^2}$ ($\approx 1\ \mathrm{sun}$) and/or are injected electrically by an applied voltage of $550\ \mathrm{mV}$. The resulting charge carrier distributions for EL (orange line), PL-sc (red line), PL-wp (yellow line) and PL-oc (green line) are shown in Fig. 4.4.

Excess charge carriers are injected electrically into the base or are generated optically very close to the front because of the small absorption length of $13\ \mu\mathrm{m}$ ($810\ \mathrm{nm}$) of the monochromatic light. Consequently, all charge carrier distributions in Fig. 4.4 exhibit the maximum carrier density close to the front surface. The EL (orange line) and the PL-wp (yellow line) carrier distributions are fixed at $z = 0$ due to the applied voltage of $550\ \mathrm{mV}$ meanwhile the PL-sc (red line) carrier distribution is fixed at zero. Note that for PL-sc the infinite sink at $z = 0$ extracts a vast majority of the generated carriers but not all of them. A small part remains in the base due to the diffusion limitation of the transport.[16,55] As a consequence, even at short-circuit conditions,

[b] Note that this value could for example stem from recombination within the emitter and at the front surface and would thus correspond for the given base dopant density to a lumped emitter saturation current density of $J_{0e} = 300\ \mathrm{fA/cm^2}$.

luminescence photons are generated within the base of the solar cell. In the PL-oc carrier distribution a very slight flattening is noticed in Fig. 4.4 for $z \to 0$ as a cause of the effective front surface recombination velocity. In addition, the carrier densities in the PL-oc case are about one magnitude higher than for EL, PL-sc and PL-wp.

For all carrier distributions shown in Fig. 4.4 generated or injected excess carriers at the front region also diffuse toward the rear surface. Due to recombination in the base and at the rear surface a decrease toward $z \to W$ follows. At $z = W$ the carrier loss due to the rear surface recombination velocity is observable for all carrier distributions by a non-zero slope.

Superposition principle

The calculated carrier distributions in Fig. 4.4 allow to directly demonstrate the superposition principle of Eq. (4.23). At $z = 0$ one observes that the charge carrier densities of PL-wp and EL exhibit the same value. Together with a charge carrier density of zero for PL-sc the superposition principle is fulfilled. Moreover, it holds for each depth z within the solar cell base. The sum of the EL (orange line) and PL-sc (brown line) excess charge carrier density gives the charge carrier density of the PL-wp distribution (yellow line).

4.5.2 Comparison of PL-oc and PL-sc to numerical device simulator

I verify for one particular set of parameters and for the experimental setup used in this work (α_{imp} is $0.077\ \mu\mathrm{m}^{-1}$) that the simplifications which were used for the derivation of the PL-sc and PL-oc carrier distributions due to

$$\exp\left(-\frac{\alpha_{\mathrm{imp}}\, W_{\mathrm{b}}}{\cos\theta_1}\right) \ll 1 \text{ and} \tag{4.27}$$

$$\left(\frac{\cos\theta_1}{\alpha_{\mathrm{imp}}\, L_{\mathrm{b}}}\right)^2 \ll 1 \tag{4.28}$$

are valid [see Eq. (4.21) and Eq. (4.22)]. Therefore, I compare the analytical description of the carrier distribution under open-circuit and short-circuit conditions according to Eq. (4.24) and Eq. (4.20), respectively, with carrier distributions obtained by the numerical device simulator PC1D.[72] The parameters used for this comparison are shown in Table 4.2. For a simple determination of S_{eff} I neglect current losses due to shunt resistances and recombination in the space charge region. In addition, the emitter is reduced to an ideal thin layer allowing to calculate the lumped emitter saturation current density $J_{0\mathrm{e}}$ from the front surface recombination velocity S_{front} and consequently the effective surface recombination velocity S_{eff} follows ($S_{\mathrm{front}} \to J_{0\mathrm{e}} \to S_{\mathrm{eff}}$).

In Fig. 4.5 the two excess carrier distributions Δn_{oc} and Δn_{sc} obtained by PC1D are shown by open symbols and the analytical carrier distributions [see Eq. (4.24) and Eq. (4.20)] as solid lines. The qualitative agreement is excellent: The analytical curves lie on top of the simulated curves within the whole base region. The numerical integration of the PC1D carrier distributions compared to the analytical solutions [see Eq. (6.12) and (6.15)] differ for PL-oc by only $0.38\ \%$ and for PL-sc by $3.31\ \%$, giving also a good quantitative agreement.

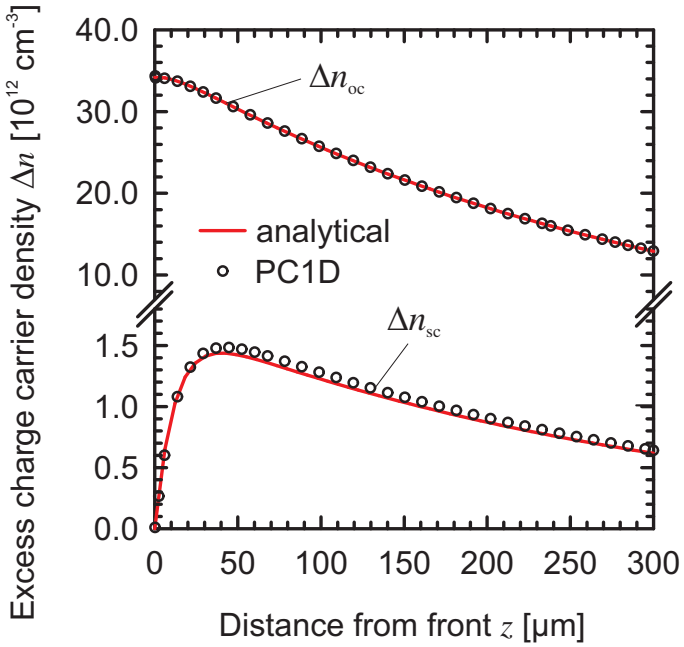

Figure 4.5: *Excess charge carrier densities within the base of a solar cell for PL-oc and PL-sc condition. The solid lines show analytical calculations according to Eq. (4.24) and Eq. (4.20). For comparison, the numerical solutions of the device simulation program PC1D are shown as open symbols. The parameters used for the solar cell simulation are given in Tab. 4.2.*

Table 4.2: *Simulation parameters for the comparison of the analytical solutions of PL-oc and PL-sc to a numerical device simulator in Fig. 4.5.*

wafer	300 µm thick, p-type, 1.47 Ωcm
front	$S_{\mathrm{front}} = 35825$ cm/s, n-type emitter, depth factor = 0.001 µm, peak doping = 4.2×10^{19} cm^{-3} (Erfc profile), $J_{0\mathrm{e}} = 300$ fAcm^{-2}, $S_{\mathrm{eff}} = 187$ cm/s (see text for calculation details)
rear	$S_{\mathrm{rear}} = 1000$ cm/s
volume	$L_{\mathrm{b}} = 300$ µm, no injection dependence, electron diffusivity 28.6 cm^2/s, $L_{\mathrm{eff}} = 298$ µm, $L_{\mathrm{C}} = 189$ µm
optics	no exterior front reflection, planar surface, all internal reflections 100 %
illumination	0.01 Wcm^{-2}, 810 nm ($L_\alpha = 13$ µm)

4.6 Short summary

In this chapter, I explicitly derived excess charge carrier distributions within the solar cell's base. These excess charge carrier distributions are one important part for the calculation of the total luminescence photon emission from silicon solar cells.

Boundary conditions for the diffusion equation were derived for all possible solar cell working points of luminescence imaging. Namely these working points are electroluminescence (EL), photoluminescence (PL) at short-circuit conditions (PL-sc), PL at an applied voltage (PL-wp) and PL at open-circuit conditions (PL-oc). I showed that for the illumination lenght of $810\ \mathrm{nm}$ used in this work a single exponential decay for the generation profile is sufficient. An approximation was introduced which holds well for solar cells with a base thickness of more than $150\ \mu\mathrm{m}$ and a bulk diffusion length of more than $100\ \mu\mathrm{m}$ and allows to obtain simple analytical solutions for the different PL charge carrier distributions.

Resulting charge carrier distributions of all working points were plotted and compared to each other. A comparison of the analytical solutions to results from a numerical device simulator gave good agreements.

CHAPTER 5

Luminescence photon emission probability

Measurable luminescence photon emission is located in the wavelength interval between approximately $900\ \mathrm{nm}$ and $1400\ \mathrm{nm}$, where the absorption within the device is weak (see absorption coefficient of silicon in Fig. 3.2 on page 28). Long-wavelength photons in combination with silicon devices featuring an optical confinement, like a textured front surface or a highly reflecting rear surface, make the derivation of the luminescence photon emission probability challenging. In the presence of optical confinement, the luminescence photons may travel various times between the front and the rear surface until being finally absorbed or emitted from the surface. Consequently, the luminescence photon emission probability becomes a function of the topography of the rear and the front surface as well as the wavelength of the luminescence photons itself.

5.1 Deriving the luminescence photon emission probability

5.1.1 Detection geometry

Aiming at the derivation of the luminescence photon emission probability, I focus on a system which uses a camera as the detector for the luminescence photons and which allows to analyze solar cells with textured front surfaces. Such a system is illustrated in Fig. 5.1(a). In this figure, the camera is shown without loss of generality by a single pixel with its corresponding optics. The solar cell is represented by thick horizontal lines corresponding to the front and the rear surface. Each pixel of the camera images the luminescence photon emission of a certain region A_E of the solar cell surface. Since the pixels are limited in size and has a certain distance to the solar cell surface not all luminescence photons emerging from A_E reach the pixel, as it would be the case for measurements with an integral sphere. Instead, the pixel only collects photons, which are sent from A_E into a certain spherical angle Ω (also often called a detection cone). Both parameters, Ω and A_E, depend on the optical properties of the used experimental setup. Note that the spherical angle Ω and A_E (and also Ω', Ω_1'', A_1 and A_2) in Fig. 5.1(a) are not to scale

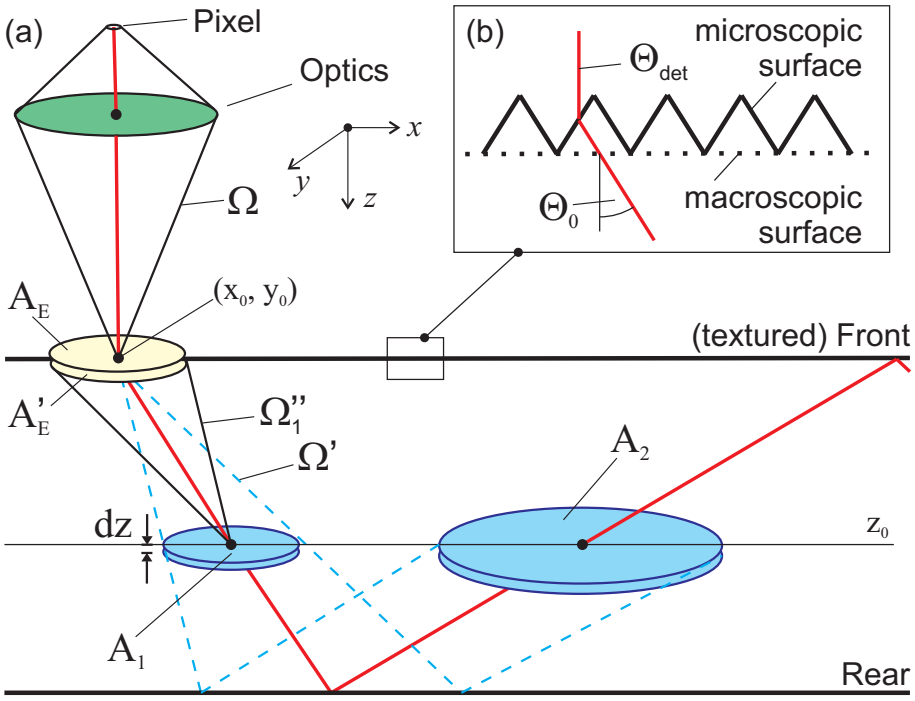

Figure 5.1: *All photons, which are sent from the surface element A_E into the detection cone Ω, are collected by the detector. Two volumes ($A_1 \cdot dz$ and $A_2 \cdot dz$) are shown, which contribute to the detectable photon emission. Ω' is the internal detection cone and Ω_1'' is the spherical angle of A_E seen from A_1.*

compared to the thickness of the solar cell and the distance of the camera to the solar cell.

Regarding a textured solar cell front surface, the microscopic and macroscopic front surface orientation differs, as shown in Fig. 5.1(b).[a] Therefore, the usual perpendicular detection ($\theta_{\mathrm{det}} = 0$) implies a refracted luminescence ($\theta_0 > 0$) emission path (red solid line in Fig. 5.1) inside the solar cell device. It becomes clear that the detectable luminescence photons stem from many different volume elements situated in the vicinity of A_E. As an example, Fig. 5.1(a) shows the two volumes $A_1 \cdot dz$ and $A_2 \cdot dz$. Both volumes give rise to luminescence photons, which are created at a certain depth z_0 and may finally emerge from the surface into one particular pixel of the camera. Since the luminescence photon generation inside the volumes $A_i \cdot dz$ is isotropical, only the fraction which is sent into the internal detection cone Ω_i'' can be collected within the pixel. Here, Ω_i'' [Ω_1'' is shown in Fig. 5.1(a)] denotes the spherical angle of A_E seen from A_i.

5.1.2 Summation of all involved volumes

The considerations of the previous section allow to express mathematically the number N_{lum} of photons that were generated at a depth z and consequently emerge from the surface element A_E.

[a] For planar surfaces, the microscopic and macroscopic front surface orientation is the same. Therefore, the luminescence emission path for a perpendicular detection is also perpendicular inside the solar cell device (for fully specular rear surfaces).

N_{lum} follows from integrating the luminescence photon generation g_{ph}, given in Eq. (3.4), over all volumes A_i, which may contribute to the photon emission at A_E,

$$N_{\mathrm{lum}}(z, A_E) = dz\, d\lambda\, dt \cdot \sum_{i=1}^{\infty} \int_{A_i} dA \cdot g_{\mathrm{ph}}(z, \lambda) \cdot \frac{\Omega_i''}{4\pi} \cdot T(dA, A_E). \tag{5.1}$$

Here, $T(dA, A_E)$ was introduced, which denotes the transmittance from the volume $dA \cdot dz$ to A_E. $T(dA, A_E)$ includes besides photon reabsorption reflection properties of the surfaces. Ω_i'' is the spherical angle of A_E seen from A_i, which is divided by the size of a unit sphere (4π) because of the isotropical generation of luminescence photons. Equation (5.1) sums up all volumes situated at a depth z, which may lead to photon emission at A_E; in Fig. 5.1 the first two volumes $A_1 \cdot dz$ and $A_2 \cdot dz$ are shown as an example.

Equation (5.1) simplifies to

$$N_{\mathrm{lum}}(z, A_E) = dz\, d\lambda\, dt \cdot \sum_{i=1}^{\infty} A_i \cdot g_{\mathrm{ph}}(z, \lambda) \cdot \frac{\Omega_i''}{4\pi} \cdot T(A_i, A_E) \tag{5.2}$$

for $\Omega_i'' \ll 4\pi$ and small volumes $dz\, A_i$, because in this case the transmittance $T(dA, A_E)$ can be assumed as constant over the volume $A_i \cdot dz$.

5.1.3 Conservation of Etendue

The étendue d^2G in three-dimensional geometry is defined as

$$d^2G = n^2\, dS\, \cos\theta\, d\Omega, \tag{5.3}$$

where n is the refractive index, $dS \cos\theta$ the light emitting surface projected to the direction θ of light propagation and $d\Omega$ is the solid angle of light emission.[77] Etendue is conserved as light travels through free space and at refractions or reflections.[78] Since the transmittance through the solar cell is already considered by the factor $T(A_i, A_E)$ in Eq. (5.2), I obtain

$$A_i\, \Omega_i''\, n_{\mathrm{Si}}^2\, \cos\theta_i = A_E'\, \Omega'\, n_{\mathrm{Si}}^2\, \cos\theta_0, \tag{5.4}$$

$$A_E'\, \Omega'\, n_{\mathrm{Si}}^2\, \cos\theta_0 = A_E\, \Omega\, n_{\mathrm{Air}}^2\, \cos\theta_{\mathrm{det}}, \tag{5.5}$$

where n_{Si} and n_{Air} give the refractive indexes of silicon and air, respectively, and θ_0 and θ_i the inclination of the surfaces A_E and A_i to the luminescence emission path (the red solid line in Fig. 5.1). θ_{det} is the inclination of the detector and will be set to zero in the following, as it is the usual case for a camera-based setup. Also $n_{\mathrm{Air}} = 1$[79,80] will be used in the following. Combining Eq. (5.4) and Eq. (5.5), I obtain

$$A_i\, \Omega_i''\, n_{\mathrm{Si}}^2\, \cos\theta_i = A_E\, \Omega \tag{5.6}$$

for the conservation of étendue.

5.1.4 One-dimensional luminescence photon emission probability

Inserting Eq. (5.6) into Eq. (5.2) yields

$$N_{\mathrm{lum}}(z, A_E) = dz\, d\lambda\, dt \cdot A_E \cdot g_{\mathrm{ph}}(z, \lambda) \cdot \frac{\Omega}{4\pi\, n_{\mathrm{Si}}^2} \cdot \sum_{i=1}^{\infty} T(A_i, A_E) \cdot \frac{1}{\cos\theta_i}. \tag{5.7}$$

Note how the conservation of étendue in the latter equation allows to express the surface element A_i and the internal emission cone Ω_i'' by the surface element A_E and the external detection cone Ω. As a consequence of Eq. (5.7), I obtain

$$\frac{N_{\mathrm{lum}}(z, A_E)}{dt\, A_E} = \varphi(\lambda)\, d\lambda = d\lambda \int_0^W dz\, g_{\mathrm{ph}}(z, \lambda) \cdot \frac{\Omega}{4\pi\, n_{\mathrm{Si}}^2} \cdot \sum_{i=1}^{\infty} T(A_i, A_E) \cdot \frac{1}{\cos\theta_i}, \tag{5.8}$$

a detailed expression for the emitted luminescence photon flux $\varphi(\lambda)$ [$\mathrm{cm^{-3}s^{-1}}$], which gives the number of detectable luminescence photons per time, wavelength interval and surface element.

The one-dimensional[b] luminescence photon emission probability f_{out} follows by comparing Eq. (5.8) to the definition of f_{out} in Eq. (3.10):

$$f_{\mathrm{out}}(z, \lambda) = \frac{\Omega}{4\pi\, n_{\mathrm{Si}}^2} \cdot \sum_{i=1}^{\infty} T(A_i, A_E) \cdot \frac{1}{\cos\theta_i}. \tag{5.9}$$

Here, A_E and Ω are both parameters determined by the optics of the measurement apparatus and the refractive index n_{Si} also is a known parameter. In contrast, $T(A_i, A_E)$ and θ_i are not known *a priori* but will be determined in the next section.

5.2 Transmittances

The transmittances $T(A_i, A_E)$ and θ_i of Eq. (5.9) depend on the photon's wavelength, the solar cell's geometry and the reflectance properties of the surfaces, due to absorption and reflection within the solar cell. This is easily exemplified for the volumes $A_1 \cdot dz$ and $A_2 \cdot dz$ shown in Fig. 5.1. Using Lambert-Beer's law [see Eq. (4.13)], the transmittances are

$$\begin{aligned} T(A_1, A_E) &= \exp\left(-\alpha \frac{z}{\cos\theta_1}\right), \\ T(A_2, A_E) &= \exp\left(-\alpha \frac{W - z}{\cos\theta_2}\right) \cdot R_{\mathrm{b}} \cdot \exp\left(-\alpha \frac{W}{\cos\theta_1}\right), \end{aligned} \tag{5.10}$$

where R_{b} is the reflectance at the rear surface and W the thickness of the device. However, it is not necessary to determine these transmittances for every volume $A_i \cdot dz$ involved in the emission of luminescence photons. As I will show in this section, the transmittances can be reverted and thus existing optical models developed for the absorption of photons can be used.

[b] In most practical cases a one-dimensional electrical model is sufficient to model transport mechanisms and carrier distribution within standard industrial silicon solar cells (see chapter 4). Thus, an one dimensional optical model which allows the simulation and analysis of experimental data is much sought after.

5.2.1 Reversibility of light rays

Microscopic reversibility implies that the direction of a light ray may be reverted, even if reflections at surfaces are involved. Applying this reversibility onto the absorption and emission of photons within the solar cell, I state that the following two situations are reverse to each other:

- The light ray $\vec{t}_{\mathrm{imp}}$ of photons, which imping on the solar cell's surface at the place A_E from a direction $\hat{t}_{\mathrm{imp},0}$, propagate within the solar cell and arrive at the volume $A_i \cdot dz$ of absorption from a direction $\hat{t}_{\mathrm{imp},N}$.

- The luminescence emission path $\vec{t}_{\mathrm{lum}}$ of luminescence photons, which are generated at $A_i \cdot dz$, sent into the direction $\hat{t}_{\mathrm{lum},0} = -\hat{t}_{\mathrm{imp},N}$, propagate inside the solar cell and are finally emitted from A_E into a direction $\hat{t}_{\mathrm{lum},N} = -\hat{t}_{\mathrm{imp},0}$.

Mathematically, this reversibility can be expressed by

$$\vec{t}_{\mathrm{lum}}(r_{\mathrm{ph}}) = \vec{t}_{\mathrm{imp}}(d - r_{\mathrm{ph}}) \quad \text{if} \quad \hat{t}_{\mathrm{lum},0} = -\hat{t}_{\mathrm{imp},N}. \tag{5.11}$$

Here, $\vec{t}_{\mathrm{imp}}(r_{\mathrm{ph}})$ accounts for the impinging photons traveling from A_E to $A_i \cdot dz$, $\vec{t}_{\mathrm{lum}}(r_{\mathrm{ph}})$ for the luminescence photons traveling vice versa. r_{ph} denotes the traveled distance and d the total length of the light ray. Note that due to the reversibility of light rays the condition $\hat{t}_{\mathrm{lum},0} = -\hat{t}_{\mathrm{imp},N}$ implies $\hat{t}_{\mathrm{lum},N} = -\hat{t}_{\mathrm{imp},0}$.

As an example, the reversibility of light rays is illustrated within two dimensions in Fig. 5.2. Figure 5.2(a) shows the absorption of impinging photons, whereas Fig. 5.2(b) illustrates the emission of luminescence photons. The assumed place of impinging photon absorption is marked with a red square in Fig. 5.2(a) and the place of luminescence photon generation with a green one in Fig. 5.2(b). Each photon within the figure propagates under an angle θ_1, θ_2 and θ_3 through the semiconductor until it is reflected at the surfaces, emerges from the front surface or is absorbed in the silicon. The reversibility of light rays implies the same angles θ_i of propagation for impinging and for luminescence photons.

5.2.2 Equality of transmittances

The number of photons N along a particular light ray $\vec{t}$ decreases due to the absorption within the silicon and by non-perfect reflection at the surfaces. As stated in the previous section, the light ray of impinging photons ($\vec{t}_{\mathrm{imp}}$) and the emission path of luminescence photons ($\vec{t}_{\mathrm{lum}}$) are reverse to each other. In addition, Lambert-Beer's law,

$$N = N_0 \cdot \exp\left(-\alpha\, r_{\mathrm{ph}}\right), \tag{5.12}$$

where N_0 is the number of photons at $r_{\mathrm{ph}} = 0$, only depends on the traveled distance r_{ph} of the photons and not on the direction of travel. Thus, for reverse light rays, the transmittance from A_E to A_i for impinging and from A_i to A_E for luminescence photons is equal,

$$T(A_E, A_i) = T(A_i, A_E). \tag{5.13}$$

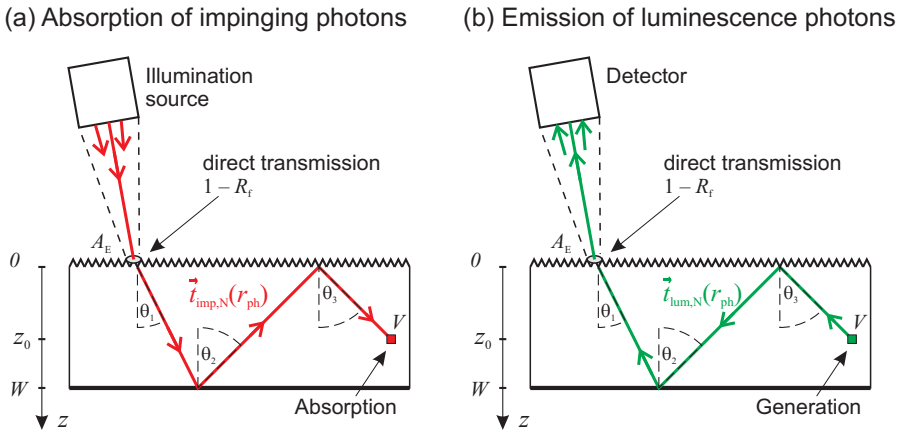

Figure 5.2: *Reversibility of light rays for the absorption of impinging photons (a) and the emission of luminescence photons (b).*

The benefit of this equality of transmittances is that $T(A_i, A_E)$, as used in the luminescence photon emission probability of Eq. (5.9), can directly be expressed by the transmittance of *impinging* photons,

$$T(A_i, A_E) = T(A_E, A_i) = \frac{N_{\text{imp}}(A_i)}{N_{\text{imp},0}}. \tag{5.14}$$

Here, $N_{\text{imp}}(A_i)$ is the number of remaining impinging photons when they pass the volume $A_i \cdot dz$ and $N_{\text{imp},0}$ is the number of photons which imping on the surface element A_E (i. e. from a lamp).

Inserting the description of the transmittance $T(A_i, A_E)$ of Eq. (5.14) into the expression of f_{out} in Eq. (5.9), yields the luminescence photon emission probability,

$$f_{\text{out}}(z, \lambda) = \frac{\Omega}{4\pi\, n_{\text{Si}}^2} \cdot \sum_{i=1}^{\infty} \frac{1}{\cos\theta_i} \cdot \frac{N_{\text{imp}}(A_i)}{N_{\text{imp},0}}. \tag{5.15}$$

The latter equation can be written as

$$f_{\text{out}}(z, \lambda) = \frac{\Omega}{4\pi\, n_{\text{Si}}^2} \cdot \frac{1}{\cos\theta_{f(i)}} \cdot \frac{\Phi_{\text{imp}}(z, \lambda)}{\Phi_{\text{imp},0}}, \tag{5.16}$$

where the term $1/\cos\theta_{f(i)}$ was introduced as an operator, which has to be applied to each summand of the photon flux[c]

$$\Phi_{\text{imp}}(z, \lambda) = \frac{1}{A_E} \cdot \sum_{i=1}^{\infty} N_{\text{imp}}(A_i). \tag{5.17}$$

$\Phi_{\text{imp}}(z, \lambda)$, as defined in the latter equation, is the sum over all volumes which are located at a depth z and absorb photons of the impinging photon flux

$$\Phi_{\text{imp},0} = \frac{N_{\text{imp},0}}{A_E} \tag{5.18}$$

[c] As a direct consequence of the one-dimensionality, $\Phi_{\text{imp}}(z, \lambda)$ can become larger than $\Phi_{\text{imp},0}$ for long-wavelengths photons, which travel various times between the surfaces.

at the surface element A_E.

Equation (5.16) makes obvious that the luminescence photon emission probability is directly related to the impinging photon flux profile. Thus, the mathematical description of the absorption of photons also describes the emission of photons!

Note the differences between $\Phi_{\mathrm{imp}}(z,\lambda)$ and $f_{\mathrm{out}}(z,\lambda)$ in Eq. (5.16). The first factor $\Omega\, 4\pi/n_{\mathrm{Si}}^2$ is required because of the isotropical generation of the luminescence photons. This factor thus reduces the number of isotropically generated luminescence photons to those, which are sent into the required detection/emission cone Ω. In contrast, the impinging photon flux is already defined as the number of photons inside Ω, which imping on the surface element A_E. The second factor $1/\cos\theta_{f(i)}$ in Eq. (5.16) accounts for the different geometries. The impinging photons, which pass for instance the area A_1, are counted for $N_{\mathrm{imp}}(A_1)$ but they are not related to the size of A_1 itself. The luminescence photons instead are generated in the volume $A_1 \cdot dz$ and send into the spherical angle Ω_1''. Here, the factor $1/\cos\theta_1$ is a direct consequence of the conservation of étendue, as shown in Eq. (5.6).

5.3 Relating the emission probability to the generation profile

Usually, a one-dimensional generation profile is given instead of a one-dimensional photon flux profile. Since both properties are related by [see also Eq. (4.12)]

$$g_{\mathrm{eh}}(z,\lambda) = -\frac{d}{dz}\frac{\Phi_{\mathrm{imp}}(z,\lambda)}{\Phi_{\mathrm{imp},0}\cdot(1-R_{\mathrm{f}})}, \tag{5.19}$$

the one-dimensional luminescence emission probability of Eq. (5.16) reads

$$f_{\mathrm{out}}(z,\lambda) = -(1-R_{\mathrm{f}})\cdot\frac{\Omega}{4\pi\, n_{\mathrm{Si}}^2}\cdot\frac{1}{\cos\theta_{f(i)}}\cdot\int_0^z dz'\, g_{\mathrm{eh}}(z',\lambda). \tag{5.20}$$

In general, the one-dimensional generation profile can be expressed by applying Lambert-Beer's law to each light turn,

$$g_{\mathrm{eh}}(z,\lambda) = \frac{\alpha}{\cos\theta_{f(i)}}\cdot\sum_i \exp\left(-\alpha\,\frac{z}{\cos\theta_i}\right), \tag{5.21}$$

which gives a sum of exponential decays. The latter generation profile implies the identity[d]

$$\int_0^z dz'\, g_{\mathrm{eh}}(z',\lambda) = -\frac{\cos\theta_{f(i)}}{\alpha}\, g_{\mathrm{eh}}(z,\lambda). \tag{5.22}$$

Inserting Eq. (5.22) into Eq. (5.20) yields the result

$$f_{\mathrm{out}}(z,\lambda) = (1-R_{\mathrm{f}})\cdot\frac{\Omega}{4\pi\, n_{\mathrm{Si}}^2}\cdot\frac{g_{\mathrm{eh}}(z,\lambda)}{\alpha}. \tag{5.23}$$

For clarity, Fig. 5.3 summarizes the different transformations between Φ_{imp}, g_{eh} and f_{out} carried out in this chapter.

[d]The constraint $g_{\mathrm{eh}}(z,\lambda) \to 0$ for very weak absorption ($\lambda \to \infty$) was used to determine the constant of integration to zero.

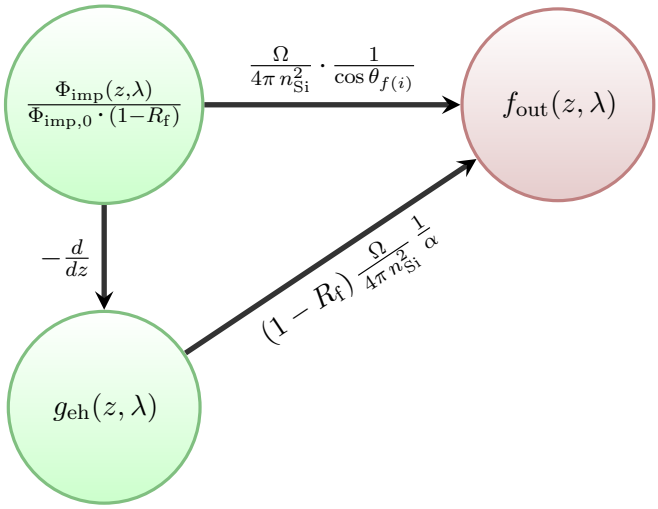

Figure 5.3: *Transformations between Φ_{imp}, g_{eh} and f_{out} as derived in this chapter.*

The result in Eq. (5.23) formulates a very general relation, called f-g-relation in the following, which states that the luminescence photon emission probability $f_{\mathrm{out}}(z,\lambda)$ directly follows from a normalized generation profile $g_{\mathrm{eh}}(z,\lambda)$. Therefore, previously published optical models developed for the absorption of light can directly be used for the emission of luminescence photons.

5.3.1 Research context of the result

I derived the f-g-relation in the following steps, as also visualized in Fig. 5.4:

- Summation of all volume elements, which lead to a luminescence photon emission in direction to the detector [see Eq. (5.1)].
- The conservation of étendue allows to express A_i and Ω_i'' by A_E and Ω.
- Comparison to the definition of f_{out} in Eq. (3.10).
- The equality of transmittances for reverse light rays allows to insert the generation profile g_{eh} of impinging photons.

As a result, the f-g-relation of Eq. (5.23) is obtained. Since only the reversibility of light rays and the conservation of étendue is required, the derived f-g-relation holds for electrically (EL) and optically (PL) stimulated luminescence.

Volume-summation approaches has been used by different authors[21,81,82] in a more specific manner. These authors focused their analysis on EL imaging and on planar front surfaces and obtained for this case explicit expressions for f_{out}; however, a relation of f_{out} to the generation profile g_{eh} was not obtained. The work in this chapter thus improves the volume-summation approach and shows for the first time that this approach directly leads to the f-g-

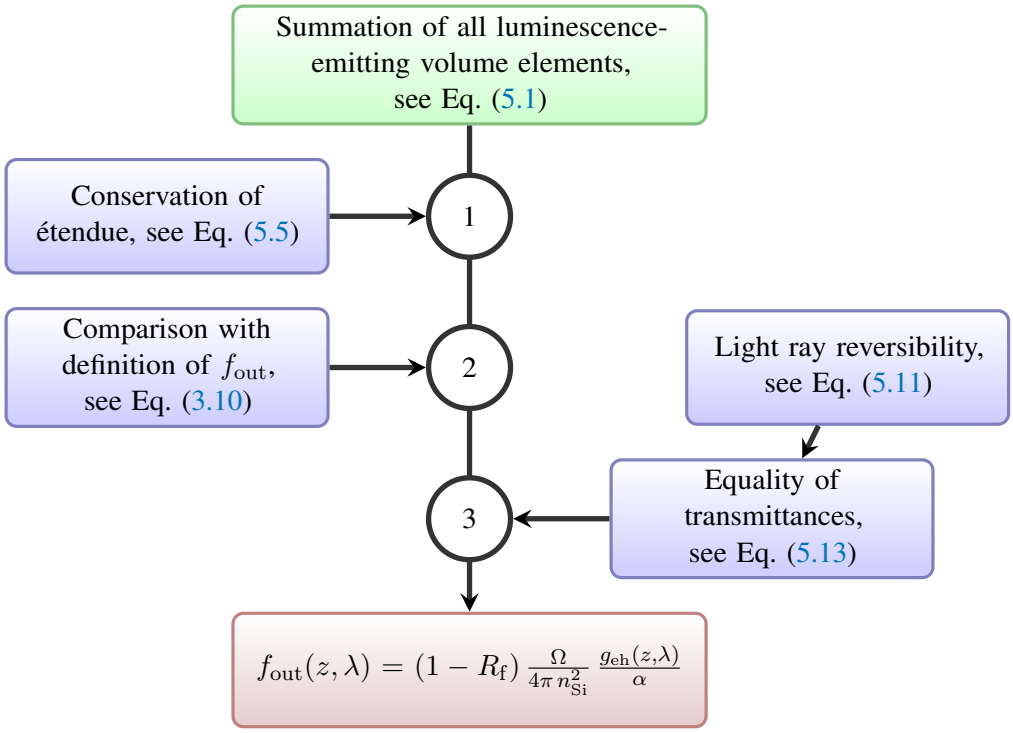

Figure 5.4: *Sketch of the different steps carried out in this chapter to derive the relation between* f_{out} *and* g_{eh}.

relation. Consequently, expressions also for textured surfaces, which exhibit all modern solar cells, can be obtained in a very simple manner (see Sec. 5.4).

The f-g-relation cannot only be derived using a volume-summation approach but also from the principle of detailed balance and the optical reciprocity theorem:

- By using the principle of detailed balance between radiative recombination and photogeneration,[51] Kirchartz et al. derived the f-g-relation in Ref. 83. This detailed-balance approach uses Kirchhoff's law[84] of radiation (emission equals absorption in heated objects) together with Würfel's generalized Planck law,[52] which consequently allows the calculation of the emitted luminescence photon flux φ in dependence of the absorptance a of the solar cell. Since the absorptance a is the integral over the generation rate g_{eh}, the f-g-relation can be obtained for devices with flat quasi-fermi levels. The authors of Ref. 83 stated that the f-g-relation is independent of the particular quasi-fermi level distribution and thus also holds for devices and working points with non-flat quasi-fermi levels, i. e. EL and PL on wafer-based silicon solar cells.[85]

- Another approach (also compare with Kirchartz et al. in Ref. 83) to derive the f-g-relation makes use of the optical reciprocity theorem introduced by Rau.[86] Rau's optical reciprocity theorem relates the electroluminescent photon emission to the quantum efficiency of the solar cell. Using this theorem, the f-g-relation follows, as also shown in the appendix B of this work. Since the derivation of the optical reciprocity theorem makes use of Donolato's theorem,[87] this approach is limited to the non-illuminated (EL) case only.

The detailed-balance and the optical-reciprocity approach are both based on macroscopic descriptions of the solar cell. In contrast, the volume-summation approach shown in this chapter is based on a microscopic description which is then transformed by the summation and integration to a macroscopic description.[e] Since it only requires the conservation of étendue and the reversibility of light rays it is directly valid for EL *and* PL imaging. For clarity, the three different approaches to derive the f-g-relation of Eq. (5.23) are visualized in Figure 5.5.

5.4 Resulting one-dimensional emission probability

Due to the resulting f-g-relation it is possible to use previously published optical models developed for the absorption of photons. In principle, any generation profile $g_{\mathrm{eh}}(z, \lambda)$ can be used in Eq. (5.23) to obtain the luminescence photon emission probability $f_{\mathrm{out}}(z, \lambda)$. In this work, I choose a generation profile published by Brendel et al. in Ref. 70 [also see Eq. (4.15)] because it is valid for textured front surfaces and is especially well suited to describe the long-wavelength photon propagation inside the solar cell.

Combining Eq. (5.23) with the generation profile $g_{\mathrm{eh}}(z, \lambda)$ of Eq. (4.15), the emission

[e] Note that the reversibility of light rays and the conversation of étendue were also used by Rau to derive the optical reciprocity theorem for solar cells in Ref. 86.

[f] The PL case was not explicitly addressed in Ref. 83 but since the derivation makes use of the equilibrium it holds for arbitrary quasi-fermi level distributions.[85]

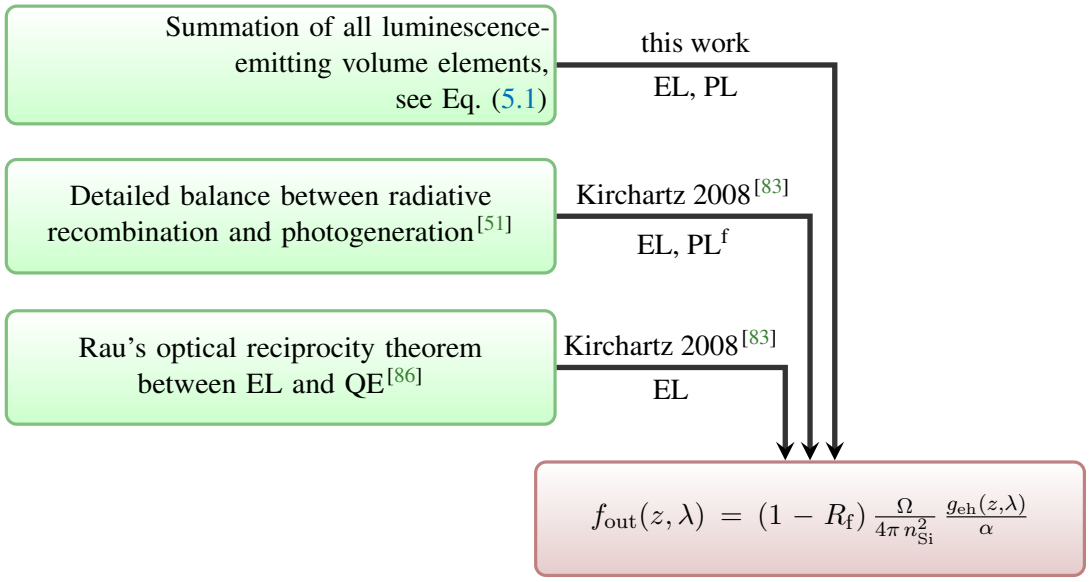

Figure 5.5: *Research context of the resulting relation between the luminescence photon emission probability and the generation profile.*

probability of a textured solar cell becomes

$$\begin{aligned} f_{\mathrm{out}}(z,\lambda) =& (1 - R_{\mathrm{f}}) \frac{\Omega}{4\pi\, n_{\mathrm{Si}}^2} \Bigg[\\ & \frac{1}{\cos\theta_1} \exp\left(\frac{-\alpha z}{\cos\theta_1}\right) + \\ & \frac{1}{\cos\theta_2} T_1 R_{\mathrm{b1}} \exp\left(\frac{-\alpha(W_{\mathrm{b}} - z)}{\cos\theta_2}\right) + \\ & \frac{1}{\cos\theta_n} \frac{T_1 R_{\mathrm{b1}} T_2 R_{\mathrm{f1}}}{1 - T_n^2 R_{\mathrm{fn}} R_{\mathrm{bn}}} \times \\ & \left(\exp\left(\frac{-\alpha z}{\cos\theta_n}\right) + T_n R_{\mathrm{bn}} \exp\left(\frac{-\alpha(W_{\mathrm{b}} - z)}{\cos\theta_n}\right)\right) \Bigg], \end{aligned} \tag{5.24}$$

which can directly be used in Eq. (3.14) for EL, PL-sc, PL-wp and PL-oc. In Eq. (5.24), α is the absorption coefficient and the term $(1 - R_{\mathrm{f}})$ accounts for the light intensity reduction as a consequence of the direct transmission of photons at the front surface. The parameters θ_1, θ_2 and θ_n give the angles of light propagation, where the indexes 1, 2 and n denote the corresponding pass or surface hit of the photon propagation within the solar cell. R_{f1} and R_{fn} give the internal reflectance at the front surface, R_{b1} and R_{bn} give the internal reflectance at the rear surface and the transmittances T_1, T_2 and T_n describe the transmission

$$T_i = \exp\left(-\frac{\alpha_{\mathrm{imp}} W_{\mathrm{b}}}{\cos(\theta_i)}\right) \tag{5.25}$$

of the i-th pass through the base. More details about the determination of the different θ_i- and T_i-values are found in Ref. 70 and in the appendix A of this work.

It was found experimentally for the absorption of light that the reflection at the rear surface of the solar cell is often neither specular nor ideal diffuse (Lambertian surface).[70] The mathematical description of the parameters in Eq. (5.24) therefore assumes a rear surface, where an areal fraction Λ behaves like an ideal Lambertian reflector (diffuse reflection) while a fraction $1 - \Lambda$ is ideally flat (specular reflection).[g] Such a description is especially important for long-wavelength light $> 1000\ \mathrm{nm}$, where multiple reflections within the device occur, as is the case for luminescence measurements.

5.5 Optical lateral resolution of luminescence imaging

One of the key features of luminescence imaging is the possibility to obtain lateral information about the local properties of solar cells. However, for solar cells which exhibit an optical confinement, i. e. due to a textured surface, photons are internally refracted and reflected. As analyzed in this chapter, the luminescence photons emerge from the solar cell in direction to the detector at a certain distance from the place of generation. Often, this effect is entitled "smearing" or "blurring". Based on the presented model for the emission of luminescence in this chapter [see Eq. (5.24)], I calculate the part of the solar cell from which the detected photons originate.

Figure 5.6(a) sketches the cross-section of a textured solar cell. I assume that the detector collects luminescence photons, which are emitted perpendicular to the surface at the position $(0, 0)$. The position of photon emission is visualized in Fig. 5.6(a) with a green arrow. The lateral distance d from the place of detection at $(0, 0)$ to the place of photon generation is the axis of abscissae shown in Fig. 5.6(a). I quantify this distance by

$$d_i(z, \lambda) = z\ \tan\theta_i + \sum_{k=1}^{i-1} W_\mathrm{b} \tan\theta_k. \tag{5.26}$$

Here, i denotes the corresponding light pass, θ_i is the angle of photon propagation and W_b the device's base thickness. Equation (5.26) allows to substitute the parameter z in Eq. (5.24) to obtain a distance-dependent emission probability f_out.

I calculate f_out using Eq. (5.24) and Eq. (5.26) for a $200\ \mu\mathrm{m}$ thick solar cell which exhibits a textured front surface ($R_\mathrm{fn} = 0.928$, $R_\mathrm{f1} = R_\mathrm{fs} = 0.62$) and a fully specularly ($\Lambda = 0$, $\theta_2 = \theta_1$) reflecting rear surface ($R_\mathrm{bn} = R_\mathrm{b1} = 1$). The solid angle of detection is set to a value of 0.00785, which corresponds to a realistic value for the experimental setup introduced in Chap. 2.

Figure 5.6 shows the calculated results for three different detection wavelengths (920, 1000 and $1100\ \mathrm{nm}$). It is shown in this figure that the lateral resolution strongly depends on the photon's wavelength. Volume elements, which have a distance of zero to the place of emission, exhibit an emission probability of about 6.5×10^{-5} for all three wavelengths. Already at a distance of $100\ \mu\mathrm{m}$ the emission probability is nearly zero for the $920\ \mathrm{nm}$ light, has dropped

[g] Note that the propagation of photons within each pass can only be described statistically for rough rear surfaces and multiple reflected light. θ_2 and θ_n then describe well a group of photons but do not hold for each single photon. Consequently, θ_2 and θ_n become an effective mean angle, which describe in combination with Eq. (5.25) the transmittance of the group of photons for the particular pass. θ_2 and θ_n then depend on the front and rear reflectance properties of the solar cell and the wavelength λ_imp of the impinging photons.

to about one-third for the $1000\ \mathrm{nm}$ light and is nearly unchanged for the $1100\ \mathrm{nm}$ light. For short-wavelength photons, the lateral resolution is high, whereas long-wavelength photons travel a larger distance through the sample. When defining the lateral resolution as the distance where the emission probability has dropped to one-half, the resolution for $920\ \mathrm{nm}$ is $\approx 19\ \mu\mathrm{m}$, for $1000\ \mathrm{nm}$ it is $\approx 71\ \mu\mathrm{m}$ and for $1100\ \mathrm{nm}$ it is $\approx 1200\ \mu\mathrm{m}$.

Note that the emission probability of the $1100\ \mathrm{nm}$ curve in Fig. 5.6(b) is not a continuous function any more. A step in the function is observable at $d \approx 360\ \mu\mathrm{m}$, where the internal reflection at the front surface occurs. Here, $R_{\mathrm{fl}} = R_{\mathrm{fs}} = 0.62$ is assumed, which was determined by Brendel et al.[70] using ray tracing simulations for a solar cell texture with inverted pyramids. For distances greater than $\approx 360\ \mu\mathrm{m}$ the emission probability is described with the effective mean angle θ_n. As a consequence, the location of the photon generation cannot be specified exactly any more.

5.6 Short summary

In this chapter, I explicitly derived the luminescence photon emission probability from the solar cell surface. This emission probability is one important part for the calculation of the total luminescence photon emission from silicon solar cells.

I presented an improved volume-summation approach, which allows to obtain the luminescence emission probability by the generation profile used for the absorption of photons. Since only the reversibility of light rays and transmittances as well as the conservation of étendue is required, the presented approach is valid for all working points including electro- and photoluminescence imaging.

Due to the resulting relation between the luminescence emission probability and the generation profile, it was possible to take advantage of previously published optical models developed for the absorption of photons. A generation profile was chosen, which is especially well suited to describe the long-wavelength photon propagation inside the solar cell. Consequently, a general description of the luminescence photon emission probability was obtained, which accounts for planar as well as textured silicon solar cells with rough rear surfaces.

Finally, I showed a first application of the obtained luminescence photon emission probability and calculated the expected optical resolution of luminescence imaging for different wavelengths. While the detection at short wavelengths can be carried out with a high lateral resolution ($\approx 19\ \mu\mathrm{m}$ for $920\ \mathrm{nm}$), the lateral resolution is low for long wavelength photons ($\approx 1200\ \mu\mathrm{m}$ for $1100\ \mathrm{nm}$).

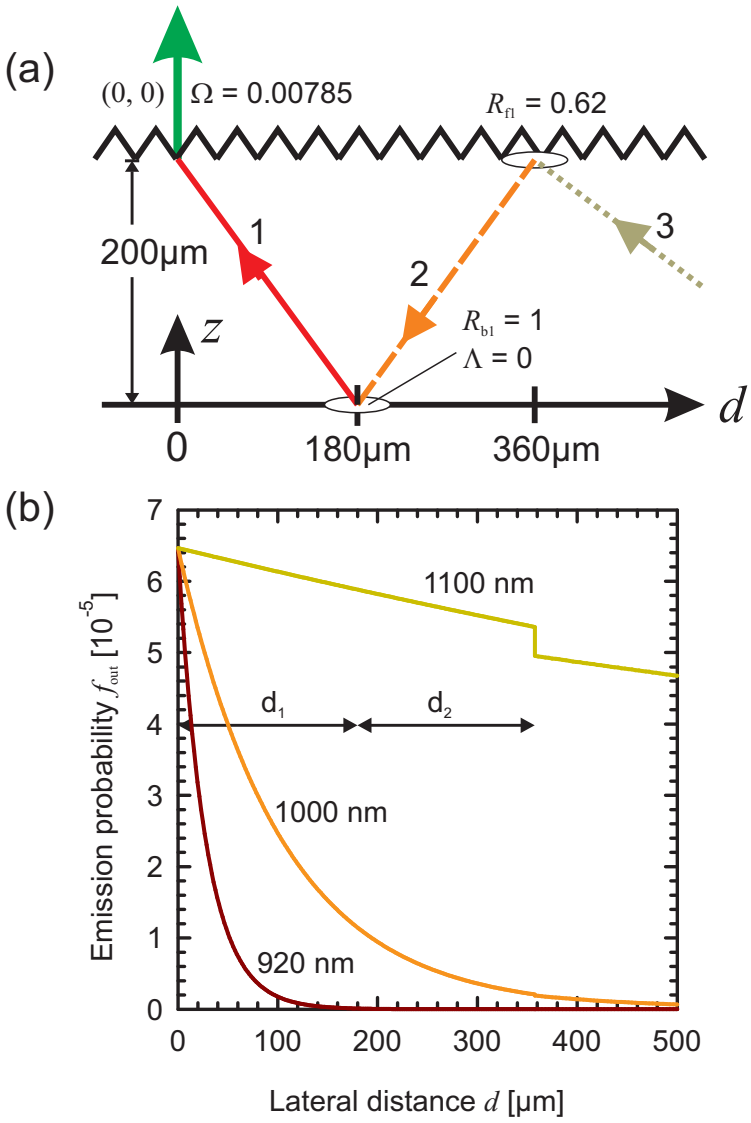

Figure 5.6: *Emission probability f_{out} from Eq. (5.24) in dependence of the distance d [see Eq. (5.26)] for three different wavelengths.*

CHAPTER 6

Spectral and integral analysis of the luminescence emission

The present chapter finally analyzes the luminescence emission integral. Therefore, I first summarize the key aspects of the previous chapters. The luminescence integral is then solved numerically resulting in luminescence emission spectra of silicon solar cells. These spectra are analyzed at different working points, different electrical and optical properties and are compared to experiment. Analytical solutions for the camera-based detection of luminescence photons for EL, PL-wp, PL-oc and PL-sc can be given in the short (< 920 nm) and long wavelength (> 1100 nm) range. This allows to discuss in detail the impact of various parameters of the solar cell onto the detected luminescence signal.

6.1 Luminescence emission integral

In chapter 3 the luminescence emission integral

$$\Phi_{\mathrm{lum}}(\lambda) = N_{\mathrm{A}}\, C_{\mathrm{eh}}\, b_{\mathrm{low}}(\lambda) \int_0^{W_{\mathrm{b}}} dz\, f_{\mathrm{out}}(z,\lambda) \Delta n(z) \tag{6.1}$$

is derived. Here, N_{A} is the bulk dopant concentration, C_{eh} a couloumb enhancement factor, b_{low} the spectral coefficient of radiative recombination, W_{b} the width of the base, f_{out} the luminescence emission probability and Δn the excess charge carrier distribution.

6.2 Excess charge carrier distributions

6.2.1 Electroluminescence

Regarding the electroluminescence (EL) case I derive in chapter 4 the excess charge carrier distribution [see Eq. (4.18)]

$$\Delta n_{\mathrm{drk}}(z) = n_1 \cdot \left[\cosh\left(\frac{z}{L_{\mathrm{b}}}\right) - \frac{L_{\mathrm{b}}}{L_{\mathrm{eff}}}\,\sinh\left(\frac{z}{L_{\mathrm{b}}}\right)\right], \tag{6.2}$$

which is the well-known dark carrier distribution. L_{b} is the bulk diffusion length and L_{eff} the effective diffusion length of the base, as defined in Eq. (4.19).

6.2.2 Photoluminescence at short-circuit conditions

In the PL-sc case the resulting excess charge carrier distribution is [see Eq. (4.20)]

$$\Delta n_{\mathrm{sc}}(z) = \Phi_{\mathrm{imp},0} \cdot \frac{(1-R_{\mathrm{f}})}{D} \cdot \frac{\cos(\theta_1)}{\alpha_{\mathrm{imp}}} \cdot \left[\frac{\Delta n_{\mathrm{drk}}(z)}{n_1} - \exp\left(-\frac{\alpha_{\mathrm{imp}} z}{\cos\theta_1}\right)\right]. \tag{6.3}$$

Here, $\Phi_{\mathrm{imp},0}$ denotes the impinging photon flux on the front surface of the monochromatic illumination, R_{f} the reflectance of the front surface, D the diffusion constant, θ_1 the angle of photon propagation of the impinging photons within its first pass in the semiconductor and α_{imp} the absorption coefficient of silicon of the impinging photons.

6.2.3 Photoluminescence at working-point conditions

For PL-wp I utilize a fundamental superposition principle[73–75] stating that the carrier distribution inside the base at an arbitrary working point (the solar cell is illuminated and held at a specific voltage) is the sum of the dark carrier and the short circuit carrier distribution (see Eq. (4.23)),

$$\Delta n_{\mathrm{wp}}(z, \lambda_{\mathrm{imp}}) = \Delta n_{\mathrm{drk}}(z, \lambda_{\mathrm{imp}}) + \Delta n_{\mathrm{sc}}(z, \lambda_{\mathrm{imp}}). \tag{6.4}$$

Thus, the solution for PL-wp is already given by the sum of Eq. (6.2) and Eq. (6.3).

6.2.4 Photoluminescence at open-circuit conditions

For the excess charge carrier distribution at open-circuit condition I obtain [see Eq. (4.24)]

$$\Delta n_{\mathrm{oc}}(z) = \Phi_{\mathrm{imp},0} \cdot \frac{(1-R_{\mathrm{f}})}{D} \cdot \frac{\cos\theta_1}{\alpha_{\mathrm{imp}}} \cdot \left[\frac{K\,L_{\mathrm{eff}}\,\alpha_{\mathrm{imp}}}{\cos\theta_1} \cdot \frac{\Delta n_{\mathrm{drk}}(z)}{n_1} - \exp\left(-\frac{z\,\alpha_{\mathrm{imp}}}{\cos\theta_1}\right)\right], \tag{6.5}$$

where K is defined in Eq. (4.25) and accounts for parasitic current losses[a] acting at the front of the bulk region.

[a] Parasitic currents, as introduced in Sec. 4.2.1, may be caused for example by shunt resistances or by recombination in the emitter or the space-charge region.

6.3 Luminescence photon emission probability

The luminescence photon emission probability is derived explicitly in chapter 5 and reads [see Eq. (5.24)]

$$
\begin{aligned}
f_{\mathrm{out}}(z,\lambda_{\mathrm{lum}}) = \frac{\Omega}{4\pi\, n_{\mathrm{Si}}^2}(1-R_{\mathrm{f}}) \Bigg[& \\
& \frac{1}{\cos\theta_1}\, \exp\left(\frac{-\alpha_{\mathrm{lum}} z}{\cos\theta_1}\right) + \\
& \frac{1}{\cos\theta_2}\, T_1 R_{\mathrm{b1}} \exp\left(\frac{-\alpha_{\mathrm{lum}} \cdot (W_{\mathrm{b}} - z)}{\cos\theta_2}\right) + \\
& \frac{1}{\cos\theta_n}\, \frac{T_1 R_{\mathrm{b1}} T_2 R_{\mathrm{f1}}}{1 - T_n^2 R_{\mathrm{fn}} R_{\mathrm{bn}}} \times \\
& \left(\exp\left(\frac{-\alpha_{\mathrm{lum}} z}{\cos\theta_n}\right) + T_n R_{\mathrm{bn}} \exp\left(\frac{-\alpha_{\mathrm{lum}} (W_{\mathrm{b}} - z)}{\cos\theta_n}\right)\right) \\
& \Bigg].
\end{aligned}
\tag{6.6}
$$

In this equation, α_{lum} is the absorption coefficient in silicon of the luminescence photons of wavelength λ_{lum}, the parameters θ_1, θ_2 and θ_n give the effective angles of light propagation, R_{f1} and R_{fn} give the internal reflectance at the front surface, R_{b1} and R_{bn} give the internal reflectance at the rear surface and the transmittances T_1, T_2 and T_n describe the transmission of the i-th pass through the base. The indexes 1, 2 and n denote the corresponding pass or surface hit of the photon propagation within the solar cell.

The luminescence emission probability of Eq. (6.6) holds for textured and planar solar cells and the operation conditions EL, PL-sc, PL-wp and PL-oc. It is thus ready to be used in the luminescence integral [see Eq. (6.1)].

6.4 Spectral (spectrometer-based) luminescence detection

6.4.1 Luminescence spectra of different working points

Resulting luminescence spectra of different working points are shown in Fig. 6.1. The data for this figure is calculated using the luminescence emission integral of Eq. (6.1), the luminescence emission probability of Eq. (6.6) and the corresponding carrier distributions of Eqs. (6.2) to (6.5). Fig. 6.1(a) shows the data in a linear and Fig. 6.1(b) in a logarithmic scale. The solar cell parameters used for this calculation are given in Tab. 6.1.

The resulting spectra shown in Fig. 6.1 increase strongly for wavelengths up to 1000 nm. For longer wavelengths, the increase begins to weaken and a maximum is obtained at about 1155 nm. For wavelengths larger than 1155 nm the spectra decrease rapidly. Since the emission spectra are mainly determined by the spectral coefficient of radiative recombination b_{low} (see Sec. 3.2.2), the shape is quite similar. However, a peak-shift from 1125 nm (b_{low}) to 1155 nm (this section) is observed which directly follows from the reabsorption of photons: Photons with a short wavelength have a higher probability to be absorbed than photons with longer wavelengths.

structural:	$N_A = 10^{16}$ cm^{-3}, $W = 200$ µm,
optical:	$\theta_1 = 41.3$ deg, $R_{b1} = R_{bn} = 0.80$, $\Lambda = 0.50$,
	$R_f = 0$, $R_{fs} = 0.62$, $R_{fn} = 0.928$
base:	$L_b = 800$ µm, $S_{rear} = 200$ cm/s, $S_{front} = 201$ cm/s
excitation:	$V_{appl} = 550$ mV, $\Phi_{imp,0} = 1$ sun, $\lambda_{imp} = 810$ nm

Table 6.1: *Parameters used for the calculations of Fig. 6.1, 6.3 and 6.4 (if not otherwise stated).*

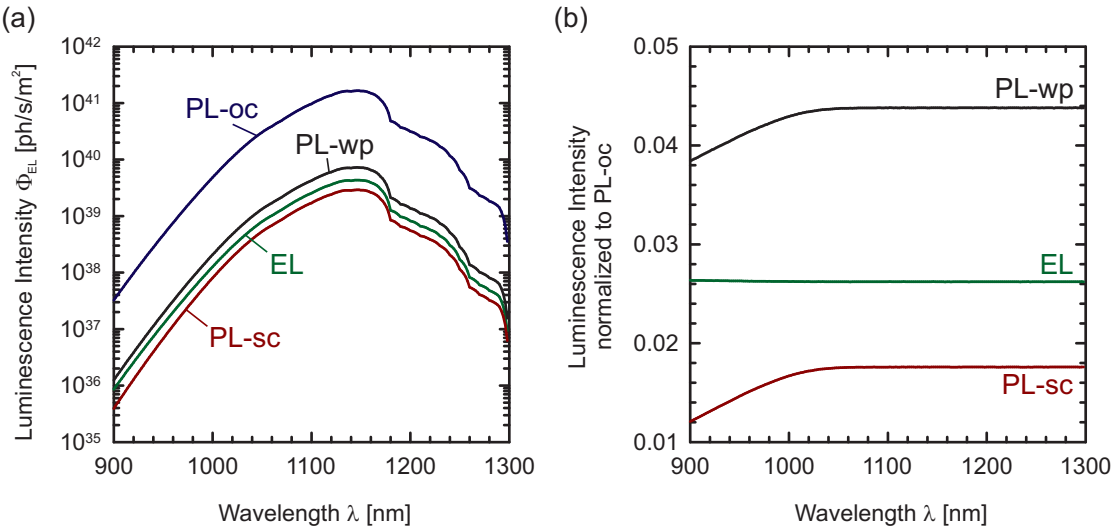

Figure 6.1: *Calculated luminescence spectra of different working points (a) and normalized to the PL-oc distribution (b) to show the differences in the shape of the spectra. The used parameters are given in Tab. 6.1.*

The spectra shown in Fig. 6.1 demonstrate that even though the totally emitted number of photons drastically change in dependence of the working point the shape of the spectra hardly changes. This can be observed in Fig. 6.1(b), where the luminescence emission normalized to the PL-oc case is shown. Changes in the shape of the spectra are only present for the short-wavelength range up to 1040 nm. For longer wavelengths, the shape of the spectra is identical. In this wavelength range the shape is not determined any more by the charge carrier distribution because the reabsorption becomes extremely low and thus the luminescence emission probability is independent of the depth of photon generation.

6.4.2 Experimental verification of caculated spectra

I verify the derived equations by describing measured luminescence spectra.

A convenient experimental verification of the derived equations is the description of measured luminescence spectra resulting from the different working points (EL, PL-sc, PL-wp and PL-oc) analyzed in this work. However, as deduced in Fig. 6.1, the different working points only result in

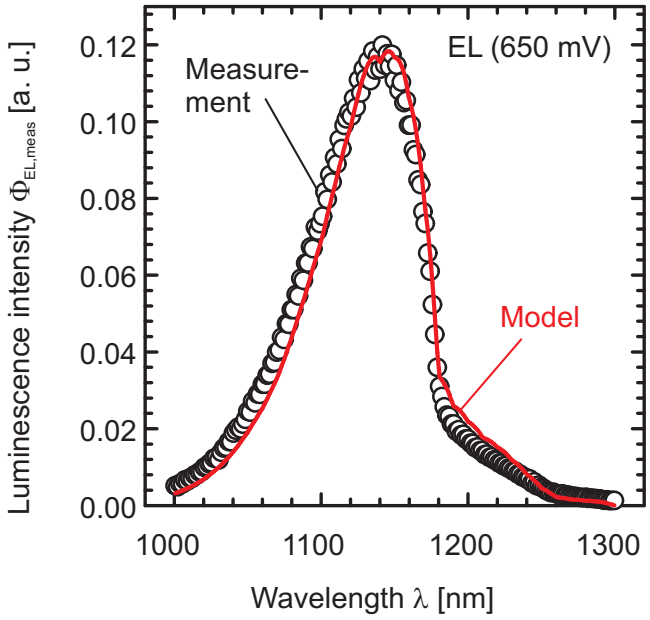

Figure 6.2: *Spectrum of the luminescence emission of an alkaline textured monocrystalline solar cell at an applied voltage of 650* mV.

differences in the spectra within the short-wavelength range. The measurement equipment which was at my disposal throughout the work at this thesis was not sensitiv enough to allow for an accurate measurement in this range. Thus, I focus in this section on the shape of the luminescence spectra for wavelengths larger than $1000\ \mathrm{nm}$ and carry out the measurements exemplarily for the EL case.

An indium-gallium-arsenide (InGaAs) spectrometer is used which detects photons in the wavelength range from $900\ \mathrm{nm}$ to $1700\ \mathrm{nm}$. The photons are collected by an optical fiber which itself is mounted perpendicularly above the solar cell. A relative intensity calibration was carried out to correct for the optical properties of the fiber and the detector.

I measure the luminescence emission of a textured monocrystalline solar cell at an applied voltage of $650\ \mathrm{mV}$ in absence of ambient light. For this measurement, the signal-to-noise ratio is improved by averaging 500 measurements and by removing the dark signal and remaining stray light by subtracting a dark spectrum (where no voltage is applied to the solar cell) from each measurement.

The open circles in Fig. 6.2 show the measured spectrum. It exhibits a maximum at about $1140\ \mathrm{nm}$ and approaches zero for wavelengths shorter than $1000\ \mathrm{nm}$ or longer than $1250\ \mathrm{nm}$. The data is shown in arbitrary units since an absolute irradiance calibration was not carried out for this setup. The luminescence spectrum is thus only measured in relative units,

$$\Phi_{\mathrm{EL,meas}} = C_{\mathrm{opt}} \cdot \Phi_{\mathrm{EL}}, \tag{6.7}$$

with an unknown constant C_{opt}.

I describe the measured spectrum using Eq. (6.1), the luminescence emission probability in

Eq. (6.6) and the dark carrier distribution of Eq. (6.2). Due to the large number of parameters, I first reduce them by using different measurement methods:

- A thickness measurement determines $\mathrm{W} = 225\ \mu\mathrm{m}$.
- Due to the alkaline textured front surface I set $\theta_1 = 41.3°$.[69]
- An analysis of the measured reflection yields $R_{\mathrm{b1}} = R_{\mathrm{bn}} = 0.64$ and $\Lambda = 0.79$.
- The scaling factor C_{opt} is determined using a calibrated quantum efficiency measurement and the optical reciprocity theorem.[86]

Finally, a least-square fit is performed to the measured data using the remaining parameters L_{b} and S_{rear}.

The spectra calculated with the determined parameters is shown in Fig. 6.2 as a red line and is in a good agreement to the measured data. The parameters L_{eff} and L_{C} [for the definitions see Eq. (4.19) and Eq. (6.11)] of this solar cell are determined to $1050\ \mu\mathrm{m}$ and $200\ \mu\mathrm{m}$, respectively, and are in good agreement to the expected values of this industrial monocrystalline solar cell. The derivation of L_{eff} to an extended quantum efficiency analysis is $20\ \%$.

6.4.3 Impact of optical properties on the luminescence spectrum

I determine the impact of optical solar-cell parameters like the rear surface reflectance R_{b} and the lambertian factor Λ onto the luminescence spectrum. I again restrict the analysis to the EL spectrum because optical parameters only have an impact on the long-wavelength range of the spectrum and thus the used distribution of excess charge carriers does not influence the results. Therefore, the bulk diffusion length is set to $1600\ \mu\mathrm{m}$ and the rear surface recombination velocity of this solar cell is zero. If not otherwise stated the parameters of Tab. 6.1 are used.

The calculations of the different electroluminescence spectra are carried out using the emission probability of Eq. (6.6) and the dark carrier distribution of Eq. (6.2). Figure 6.3 shows four different spectra (A, B, C). For a better visualization of the differences in the spectra, Fig. 6.3(b) shows the cases B and C normalized to the spectra of case A (green dash-dotted line).

The four spectra are calculated for solar cells exhibiting different rear surface reflectances R_{b} and lambertian factors Λ:

A. The green dash-dotted line shows the resulting spectrum for the same rear surface as in case A but using tabulated values from literature for the absorption coefficient [see Fig. 3.2 or Ref. 55]. This spectrum is thus the upper limit of EL emission for the underlying solar cell. While in the wavelength range up to $1175\ \mathrm{nm}$ the emission is substantially smaller than for case A, both cases approaches for longer wavelengths since reabsorption becomes negligibly small.

B. The case of a perfect specular mirror at the rear, $R_{\mathrm{b}} = 1$ and $\Lambda = 0$, is shown in Fig. 6.3 as a blue solid line. This spectrum equals case B for short wavelengths but is about one-third smaller for wavelengths above $1150\ \mathrm{nm}$. This is a consequence of internally at the rear reflected light which does not fulfill the escape condition at the front.

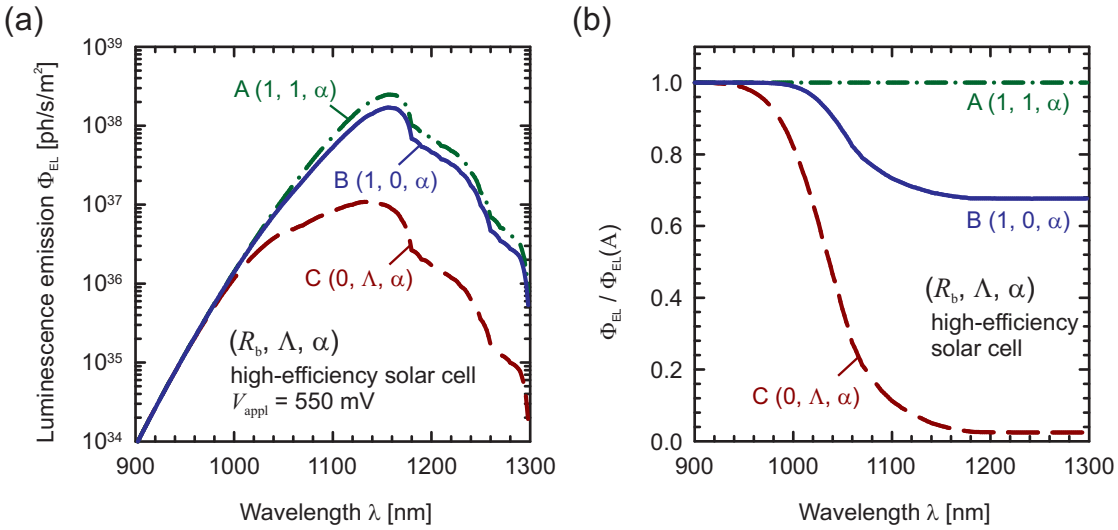

Figure 6.3: *Spectra (a) of the electroluminescence emission of a high-efficiency solar cell with different optical properties which are given by* $(R_\mathrm{b}, \Lambda, \alpha)$*. The used parameters are given in Tab.6.1, if not otherwise stated here. The spectra normalized to case A (b) visualizes the differences in the shape of the spectra.*

C. The red dashed line in Fig. 6.3 shows the calculated spectrum for a solar cell with a perfect absorber at the rear surface, which is expressed by $R_\mathrm{b} = 0$. Regarding optical parameters, this case is the lower limit of EL emission. It differs substantially from cases A and B for wavelengths larger than $1000\ \mathrm{nm}$. For the wavelength range above $1160\ \mathrm{nm}$ only $2.5\ \%$ of the luminescence of case B is emitted. It thus emphasizes the strong dependence of the luminescence emission on the rear surface reflectance.

6.4.4 Impact of base properties on the luminescence spectrum

I determine the impact of base properties like the bulk diffusion length L_b and the rear surface recombination velocity S_rear onto the luminescence spectrum. Again, the analysis is carried out for the EL case only. If not otherwise stated the parameters of Tab. 6.1 are used for the calculations.

Figure 6.4(a) shows four resulting electroluminescence spectra (A, B, C and D). The four spectra are calculated for solar cells exhibiting different base properties:

A. $L_\mathrm{b} = 800\ \mu\mathrm{m}$ and $S_\mathrm{rear} = 2\ \mathrm{cm/s}$ (black line),

B. $L_\mathrm{b} = 800\ \mu\mathrm{m}$ and $S_\mathrm{rear} = 200\ \mathrm{cm/s}$ (red line),

C. $L_\mathrm{b} = 400\ \mu\mathrm{m}$ and $S_\mathrm{rear} = 200\ \mathrm{cm/s}$ (green line),

D. $L_\mathrm{b} = 800\ \mu\mathrm{m}$ and $S_\mathrm{rear} = 3000\ \mathrm{cm/s}$ (blue line).

For a better visualization of the differences in the shape of the spectra, Fig. 6.4(b) shows the cases B, C and D normalized to the spectra of case A (black line).

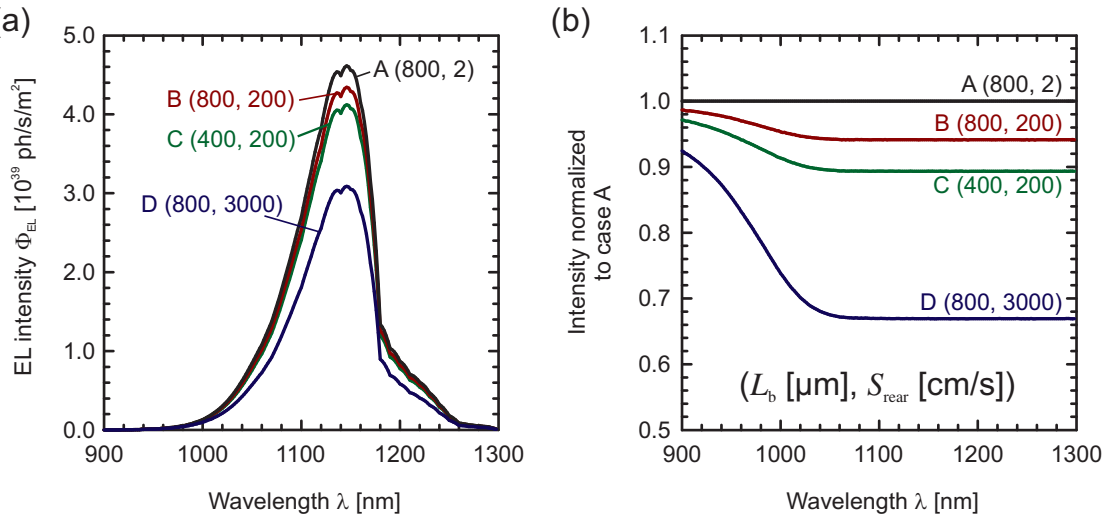

Figure 6.4: *Spectra (a) of the electroluminescence emission of solar cells with different bulk properties. The spectra normalized to case A (b) shows the differences in the shape. The used parameters are given in Tab. 6.1 if not otherwise stated here.*

Figure 6.4 demonstrates that the totally emitted luminescence increases with increasing L_b and decreasing S_{rear}, because the excess charge carrier density within the bulk is higher if the recombination in the bulk or at the rear is smaller. Changes in the shape of the spectra are only present for the short-wavelength range up to 1000 nm. For longer wavelengths, the shape of the spectra is identical, as can be deduced from Fig. 6.4(b). In this wavelength range the shape is only determined by optical parameters since the reabsorption of luminescence photons becomes extremely low and thus the luminescence emission probability is independent of the depth of the photon generation.

In principle, the determination of electrical solar cell parameters by restricting measured spectra to certain wavelengths is possible and has already been widely investigated.[21,23,24,83,88]

6.5 Integral solutions for the short- and long-wavelength range

Using the emission probability f_{out} of Eq. (6.6) and the corresponding carrier distributions of Sec. 6.2, general analytical solutions for the luminescence emission with Eq. (6.1) directly follow. In this section, I explicitly carry out the integration of Eq. (6.1) and derive closed analytical expressions without integral for two marginal luminescence detection cases: Long and short wavelengths. The long-wavelengths limit holds for wavelengths larger than 1100 nm, and the short-wavelengths limit for wavelengths smaller than 920 nm.

6.5.1 Detection in the long-wavelength range

For the long-wavelength range ($\gtrapprox 1100$ nm) the impact of reabsorption becomes negligible because of

$$\alpha_{\mathrm{lum,lg}} \to 0. \tag{6.8}$$

This limit for the absorption coefficient implies $T_1 = T_2 = T_n = 1$ and simplifies f_{out} to a function

$$f_{\mathrm{out,lg}} = \frac{\Omega}{4\pi\, n_{\mathrm{Si}}^2}\,(1-R_{\mathrm{f}})\cdot\left[\frac{1}{\cos\theta_1}+\frac{R_{\mathrm{b1}}}{\cos\theta_2}+\frac{R_{\mathrm{b1}}R_{\mathrm{f1}}}{1-R_{\mathrm{fn}}R_{\mathrm{bn}}}\,\frac{1}{\cos\theta_n}\,(1+R_{\mathrm{bn}})\right]. \tag{6.9}$$

Note that the latter emission probability $f_{\mathrm{out,lg}}$ for long wavelengths only depends on optical parameters and not on z any more and may thus be pulled out of the luminescence integral in Eq. (6.1).

Electroluminescence

I insert the limit $f_{\mathrm{out,lg}}$ and the dark carrier distribution of Eq. (6.2) into the luminescence integral of Eq. (6.1) and obtain a closed-form for the electroluminescence emission of long-wavelength photons,

$$\begin{aligned}\Phi_{\mathrm{EL,lg}}(\lambda_{\mathrm{lum}}) =& C_{\mathrm{eh}}\, b_{\mathrm{low}}(\lambda_{\mathrm{lum}})\,\frac{\Omega}{4\pi\, n_{\mathrm{Si}}^2}\,(1-R_{\mathrm{f}})\,n_{\mathrm{i}}^2\,\exp\left(\frac{V_i}{V_{\mathrm{T}}}\right)\times \\ & L_{\mathrm{C}}\cdot\left[\frac{1}{\cos\theta_1}+\frac{R_{\mathrm{b1}}}{\cos\theta_2}+\frac{R_{\mathrm{b1}}R_{\mathrm{f1}}}{1-R_{\mathrm{fn}}R_{\mathrm{bn}}}\,\frac{1}{\cos\theta_n}\,(1+R_{\mathrm{bn}})\right].\end{aligned} \tag{6.10}$$

L_{C} in the latter equation is the collection length and reads [69,89]

$$L_{\mathrm{C}} = L_{\mathrm{b}}\,\frac{L_{\mathrm{b}}\,S_{\mathrm{rear}}\left(\cosh\left(\frac{W_{\mathrm{b}}}{L_{\mathrm{b}}}\right)-1\right)+D\,\sinh\left(\frac{W_{\mathrm{b}}}{L_{\mathrm{b}}}\right)}{L_{\mathrm{b}}\,S_{\mathrm{rear}}\,\sinh\left(\frac{W_{\mathrm{b}}}{L_{\mathrm{b}}}\right)+D\,\cosh\left(\frac{W_{\mathrm{b}}}{L_{\mathrm{b}}}\right)}. \tag{6.11}$$

The electroluminescence photon flux $\Phi_{\mathrm{EL,lg}}$ is thus directly proportional to the collection diffusion length L_{C}. In Ref. 22 and Ref. 90 we utilized this proportionality to determine spatially resolved mappings of the collection diffusion length L_{C}.

Photoluminescence at short-circuit conditions

Accordingly, for photoluminescence measurements at short-circuit conditions, the emitted luminescence photon flux for the long-wavelengths range is

$$\begin{aligned}\Phi_{\mathrm{sc,lg}}(\lambda_{\mathrm{lum}}) =& C_{\mathrm{eh}}\, b_{\mathrm{low}}(\lambda_{\mathrm{lum}})\,\frac{\Omega}{4\pi\, n_{\mathrm{Si}}^2}N_{\mathrm{A}}\,\Phi_{\mathrm{imp,0}}\,\frac{\cos\theta_1}{D\,\alpha_{\mathrm{imp}}}\,(1-R_{\mathrm{f}})^2\times\left(L_C-\frac{\cos\theta_1}{\alpha_{\mathrm{imp}}}\right)\times \\ & \left[\frac{1}{\cos\theta_1}+\frac{R_{\mathrm{b1}}}{\cos\theta_2}+\frac{R_{\mathrm{b1}}R_{\mathrm{f1}}}{1-R_{\mathrm{fn}}R_{\mathrm{bn}}}\,\frac{1}{\cos\theta_n}\,(1+R_{\mathrm{bn}})\right].\end{aligned}$$

(6.12)

Note the similarities between $\Phi_{\mathrm{sc,lg}}$ and $\Phi_{\mathrm{EL,lg}}$. The PL-sc case defines a virtual voltage

$$V_{\mathrm{PL-sc}} = V_{\mathrm{T}} \cdot \ln\left(\frac{n_{\mathrm{i}}^2\,\alpha_{\mathrm{imp}}\,D}{\Phi_{\mathrm{imp,0}}\,N_{\mathrm{A}}\,(1-R_{\mathrm{f}})\,\cos\theta_1}\right) \tag{6.13}$$

which in combination with a reduced collection length $(L_{\mathrm{C}} - \cos\theta_1/\alpha_{\mathrm{imp}})$ leads to the same luminescence photon flux as in the EL case [compare with Eq. (6.5.1)].

Photoluminescence at an applied voltage

Using the finding of Eq. (4.23), that the carrier distribution inside the base at an arbitrary working point (the solar cell is illuminated and held at a specific voltage) is the sum of the dark carrier and the short circuit carrier distribution, the luminescence emission integral [see Eq. (6.1)] for PL-wp is split into two parts. The luminescence emission

$$\Phi_{\mathrm{wp}} = \Phi_{\mathrm{sc}} + \Phi_{\mathrm{EL}} \tag{6.14}$$

for the PL-wp case thus simply follows as the sum of Eq. (6.10) and Eq. (6.12).

Regarding the determination of local junction voltages V_i using luminescence images, as used for example in all luminescence based series resistance methods,[16] Eq. (6.14) makes clear why the voltage determination using PL images should be corrected locally by subtracting the PL-sc signal. The subtraction gives the same local junction condition as using EL and thus the resulting signal becomes proportional to $\exp(V_i/V_{\mathrm{T}})$. By only evaluating one photoluminescence signal the value of the local junction voltage V_i can only be approximated.[15]

Photoluminescence at open-circuit conditions

For photoluminescence measurements at open-circuit conditions, the measured luminescence signal for the long wavelength range is

$$\begin{aligned}\Phi_{\mathrm{oc,lg}}(\lambda_{\mathrm{lum}}) =& C_{\mathrm{eh}}\,b_{\mathrm{low}}(\lambda_{\mathrm{lum}})\,\frac{\Omega}{4\pi\,n_{\mathrm{Si}}^2}N_{\mathrm{A}}\,\Phi_{\mathrm{imp,0}}\,\frac{\cos\theta_1}{D\,\alpha_{\mathrm{imp}}}\,(1-R_{\mathrm{f}})^2\times \\ & \left(\frac{\alpha_{\mathrm{imp}}}{\cos\theta_1}\,K\,L_{\mathrm{eff}}\,L_C - \frac{\cos\theta_1}{\alpha_{\mathrm{imp}}}\right)\times \\ & \left[\frac{1}{\cos\theta_1} + \frac{R_{\mathrm{b1}}}{\cos\theta_2} + \frac{R_{\mathrm{b1}}R_{\mathrm{f1}}}{1-R_{\mathrm{fn}}R_{\mathrm{bn}}}\,\frac{1}{\cos\theta_n}\,(1+R_{\mathrm{bn}})\right],\end{aligned} \tag{6.15}$$

where the excess charge carrier distribution for open-circuit conditions, given in Eq. (6.5), was used. L_{eff} in the latter equation is the effective diffusion length as defined in Eq. (4.19).

6.5.2 Detection in the short-wavelength range

Focusing on the short-wavelength range smaller than $920\ \mathrm{nm}$ the assumption holds that only photons are detected which are emitted in direction to the front surface:

$$f_{\mathrm{out,sh}}(\lambda_{\mathrm{lum}}) = \frac{\Omega}{4\pi\,n_{\mathrm{Si}}^2}\,(1-R_{\mathrm{f}})\,\frac{1}{\cos\theta_1}\,\exp\left(-\frac{\alpha_{\mathrm{lum}}\,z}{\cos\theta_1}\right). \tag{6.16}$$

Note that there is no impact of the rear surface on the emission probability. Even though this reduces substantially the emitted luminescence photon flux it can be an advantage i. e. for the determination of local junction voltages: A short-wavelength detector (like silicon) monitors only the fraction of the carrier distribution which is close to the junction and is thus insensitive on lateral variations of the rear surface reflectance.

Electroluminescence

For the EL detection using a short-wavelength detector I obtain

$$\begin{aligned}\Phi_{\mathrm{EL,sh}}(\lambda_{\mathrm{lum}}) =& C_{\mathrm{eh}}\, b_{\mathrm{low}}(\lambda_{\mathrm{lum}})\, \frac{\Omega}{4\pi\, n_{\mathrm{Si}}^2}\, (1-R_{\mathrm{f}})\, n_{\mathrm{i}}^2\, \exp\left(\frac{V_i}{V_{\mathrm{T}}}\right) \times \\ & \frac{\alpha_{\mathrm{lum}} - \cos\theta_1 / L_{\mathrm{eff}}}{\alpha_{\mathrm{lum}}^2 - (\cos\theta_1 / L_{\mathrm{b}})^2}.\end{aligned} \tag{6.17}$$

In the latter equation I approximated the result by

$$\exp\left(-\frac{\alpha_{\mathrm{lum}}\, W}{\cos\theta_1}\right) \to 0. \tag{6.18}$$

The latter approximation is important to simplify the integrals for the detection of the short wavelength range. For 920 nm and a textured, 200 µm thick solar cell the exponential term in Eq. (6.18) gives a value of 1.66×10^{-3}.

The short-wavelength luminescence emission $\Phi_{\mathrm{EL,sh}}$ depends strongly on the detection wavelength and has a non-linear dependence of the recombination parameters L_{b} and L_{eff}. In contrast, a long-wavelength detector (like InGaAs) shows a way more simple dependence of the recombination properties [see Eq. (6.10)] but is instead more sensitive to the reflectance properties of the rear surface and multiple internal reflections within the sample.

Photoluminescence at short circuit conditions

For PL-sc I obtain

$$\begin{aligned}\Phi_{\mathrm{sc,sh}}(\lambda_{\mathrm{lum}}) =& C_{\mathrm{eh}}\, b_{\mathrm{low}}(\lambda_{\mathrm{lum}})\, \frac{\Omega}{4\pi\, n_{\mathrm{Si}}^2}\, N_{\mathrm{A}}\, \Phi_{\mathrm{imp,0}}\, \frac{\cos\theta_1}{D\,\alpha_{\mathrm{imp}}}\, (1-R_{\mathrm{f}})^2 \times \\ & \frac{2\,(\alpha_{\mathrm{lum}}+\alpha_{\mathrm{imp}})\, L_{\mathrm{b}}^2\, \cos\theta_1 - L_{\mathrm{eff}}\, \left[1 + 2\alpha_{\mathrm{lum}}\alpha_{\mathrm{imp}} L_{\mathrm{b}}^2 + \cos(2\theta_1)\right]}{(\alpha_{\mathrm{lum}}+\alpha_{\mathrm{imp}}) L_{\mathrm{eff}}\, \left[1 - 2\alpha_{\mathrm{lum}}^2 L_{\mathrm{b}}^2 + \cos(2\theta_1)\right]},\end{aligned} \tag{6.19}$$

where the approximations of Eq. (6.18) and

$$\left(\frac{\cos\theta_1}{\alpha_{\mathrm{imp}}\, L_{\mathrm{b}}}\right)^2 \ll 1 \tag{6.20}$$

where used. The latter approximation holds for solar cells with a base thickness of more than 150 µm, an impinging photon flux of 810 nm ($\alpha_{\mathrm{imp}} \approx 0.077$ nm), and a bulk diffusion length L_{b} of more than 100 µm.

Photoluminescence at an applied voltage

Just like for the detection at the long-wavelength range the PL-wp case again simply follows as the sum of Eq. (6.17) and Eq. (6.19).

Photoluminescence at open circuit conditions

For PL-oc I obtain

$$\begin{aligned}\Phi_{\mathrm{oc,sh}}(\lambda_{\mathrm{lum}}) =& C_{\mathrm{eh}}\, b_{\mathrm{low}}(\lambda_{\mathrm{lum}})\, \frac{\Omega}{4\pi\, n_{\mathrm{Si}}^2} N_{\mathrm{A}}\, \Phi_{\mathrm{imp,0}}\, \frac{1}{D\, \alpha_{\mathrm{imp}}}\, (1-R_{\mathrm{f}})^2 \times \\ & \frac{1}{2\,(\alpha_{\mathrm{lum}}+\alpha_{\mathrm{imp}})\left[1-2\alpha_{\mathrm{lum}}^2 L_{\mathrm{b}}^2+\cos(2\theta_1)\right]} \times \\ & \Big[\cos\theta_1\, \left(-3+4\,L_{\mathrm{b}}^2\, \left(\alpha_{\mathrm{lum}}^2+K\,\alpha_{\mathrm{imp}}\,(\alpha_{\mathrm{lum}}+\alpha_{\mathrm{imp}})\right)\right) \\ & -4\,\alpha_{\mathrm{lum}}\,\alpha_{\mathrm{imp}}\,(\alpha_{\mathrm{lum}}+\alpha_{\mathrm{imp}})\,K\,L_{\mathrm{b}}^2\,L_{\mathrm{eff}}-\cos(3\theta_1)\Big],\end{aligned} \tag{6.21}$$

where again the approximations of Eq. (6.18) and of Eq. (6.20) are used.

6.6 Integral (camera-based) luminescence detection

6.6.1 Impact of solar cell parameters on the detected signal

A qualitative and quantitave analysis of luminescence images requires an understanding of the detected luminescence signal S and its correlation to underlying solar cell parameters. The equations, derived in this chapter, describe the parameter-dependences of the detected luminescence signal mathematically. For a rough determination of the impact of the different parameters I calculate the luminescence emission in the short- and the long-wavelength-range for the parameters given in Tab. 6.1 on page 64. A small variation is performed to each parameter separately and the resulting change in the detected luminescence emission is observed.

The results of this analysis are shown in Tab. 6.2. The parameter itself is shown in the first column and its default value in the second column. The variation of the parameter is given in the third column. The last two columns show the resulting percentaged change of the detected luminescence signal in the corresponding wavelength-range.

Table 6.2 demonstrates that the base dopant density N_{A} and the applied voltage V_{appl} affect the short- and the long-wavelength range in the same manner i. e. an increase of 47% is obtained for the increase in V_i (550 to 560 mV). All other parameters affect only the long-wavelength range while the short-wavelength range does not change significantly. A strong impact have the optical parameters onto the long-wavelength range detection: 17% decrease due to the variation in R_{b} (0.9 to 0.8) and 2.55% increase due to the variation in Λ (0.5 to 0.6). The impact of the base properties L_{b} and S_{rear} onto the long-wavelength range is small but not negligibly: 0.2% (L_{b} from 800 to 850 $\mu\mathrm{m}$) and 1.35% (S_{rear} from 200 to 250 $\mathrm{cm/s}$).

One practical result of this analysis is that a voltage determination using luminescence imaging can be carried out more accurately using a short-wavelength detector, i. e. a silicon

parameter	default	variation	difference	900-920nm [%]	1100-1120nm [%]
N_A [$10^{15}\mathrm{cm}^{-3}$]	10	9	-1	+0.04	+0.04
W [µm]	200	210	+10	+0.16	+3.0
R_b	0.8	0.7	-0.1	-0.01	-17
Λ	0.5	0.6	+0.1	0.00	+2.6
L_b [µm]	800	850	+50	+0.07	+0.21
S_rear [cm/s]	200	250	+50	-0.35	-1.4
V_i [mV]	550	560	+10	+47	+47

Table 6.2: *Impact of solar cell parameters onto the electroluminescence-signal detected in the short- and the long-wavelength range. For example: A change of the local voltage V_i (550 to 560 mV) leads to a signal increase of 47% in both wavelength-ranges.*

camera, since the impact of optical and base properties is very small. While a long-wavelength detector, i. e. an InGaAs camera, is equally sensitive to the voltage, it also detects variations in optical and base properties.

6.6.2 Rear surface reflectance of short- and long-wavelength range detection

I experimentally demonstrate the impact of the rear surface reflectance onto the short- and long-wavelength range detection. Figure 6.6 shows two electroluminescence images of the same region of a multicrystalline silicon solar cell and a local reflection measurement. The image in Fig. 6.6(a) is captured by a silicon (Si) camera and the image in Fig. 6.6(b) by an indium-gallium-arsenide (InGaAs) camera. Note that the images are taken completely without filters.

The comparison of these images reveals that the visible structures differ. The region marked with a blue arrow in Fig. 6.6(b) is more pronounced by a decreased luminescence signal of the InGaAs detector than for the Si detector. Since Eqs. (6.17) and (6.10) depict a stronger impact of the rear surface reflectance onto the long-wavelength (InGaAs) detector, I carry out local reflection and quantum efficiency measurements. The resulting reflectances of the regions at position 1 and 2 are shown in Fig. 6.6(c). The analysis reveals that the effective diffusion length is $L_\mathrm{eff} = 500$ µm in both regions but the rear reflectance R_b is 0.60 at position 1 and 0.98 at position 2. The results are thus consistent with Eqs. (6.17) and (6.10).

6.6.3 Dependence of the EL signal on the effective diffusion length

I discuss the dependence of the EL signal on the effective diffusion length. For a better understanding of the correlations I deduce a simplified version of the short-wavelength EL solution in Eq. (6.17). The focus within this section lies on measurements carried out with a silicon camera since this is – up to now – the most commonly used detector type for luminescence imaging in reasearch laboratories and industry.

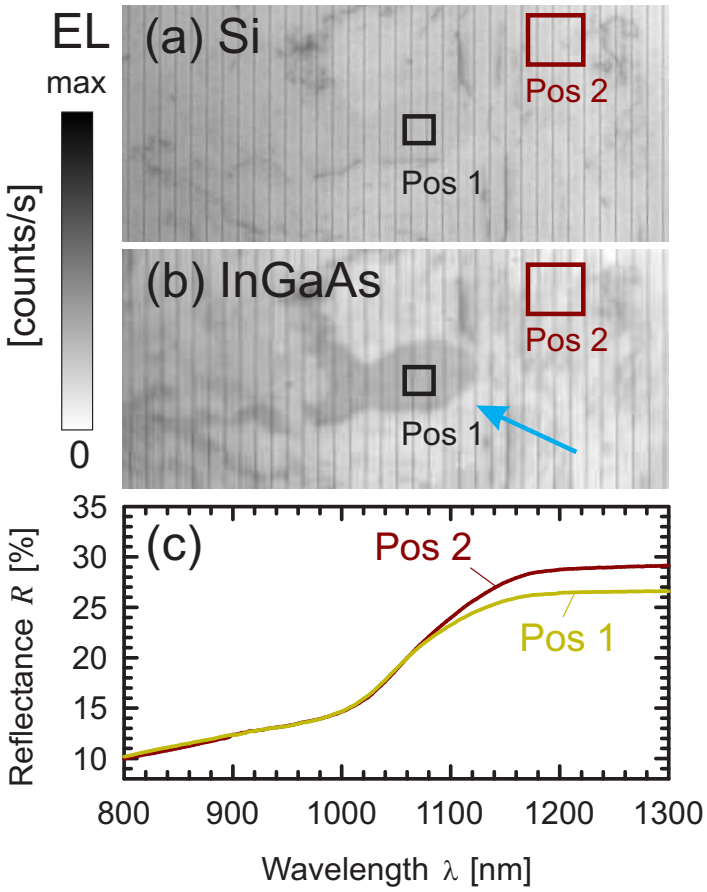

Figure 6.6: *Two luminescence images captured with a silicon (a) and an indium-gallium-arsenide (b) detector. Local reflectance measurements (c) were carried out at position* 1 *and* 2*.*

Theory

The short-wavelength EL solution of Eq. (6.17) can be approximated by

$$(\frac{\cos\theta_1}{\alpha_{\mathrm{lum}}}\frac{1}{L_{\mathrm{b}}})^2 \ll 1, \tag{6.22}$$

which allows to neglect the denominator of Eq. (6.17). Using this approximation, I define

$$\widehat{\Phi}_{\mathrm{EL}} = \Phi_{\mathrm{EL,sh}}\big|_{\mathrm{approx.}}\,\alpha_{\mathrm{lum}}\,B_{\mathrm{rad}}^{-1}\,\frac{4\pi\,n_{\mathrm{Si}}^2}{\Omega}\,(1-R_{\mathrm{f}})^{-1}\,\frac{1}{n_{\mathrm{i}}^2\,\exp(V_i/V_{\mathrm{T}})} \tag{6.23}$$

and thus obtain

$$\widehat{\Phi}_{\mathrm{EL}} = 1 - \alpha_{\mathrm{lum}}^{-1}\,\frac{\cos\theta_1}{L_{\mathrm{eff}}}, \tag{6.24}$$

which is an approximated and normalized version of the short-wavelength EL solution.

Calculations

I calculate, using the luminescence integral of Eq. (6.1) and the photon emission probability of Eq. (6.6), the emitted electroluminescence emission in dependence of the effective diffusion length L_{eff}. To account for a silicon detector, I restrict the detection to photons in-between $950\ \mathrm{nm}$ and $960\ \mathrm{nm}$. These wavelengths approximate the luminescence peak detection of the silicon detector, which follows from the product of the detector's quantum efficiency and the luminescence intensity.

The result of this calculation is shown in Fig. 6.7 as green curves. A parameter space is obtained since different combinations of the bulk diffusion length L_{b} and the rear surface recombination velocity S_{rear} may give the same L_{eff}-value but a different luminescence emission. I observe that the luminescence signal raises very quickly for short effective diffusion lengths up to a quite constant plateau.

Additionally, Fig. 6.7 shows with the blue dotted line the normalized short-wavelength approximation of Eq. (6.24). Note that these values are only relative and not absolute and thus only allow a qualitative comparison to the calculated curve (green lines). The accuracy of the short-wavelength approximation is very good for effective diffusion lengths larger than $100\ \mu\mathrm{m}$. For shorter effective diffusion lengths the deviation due to the approximation in Eq. (6.22) becomes visible.

Measurement

I demonstrate experimentally the dependence of the luminescence emission on L_{eff}. Therefore, I measure the luminescence emission of 20 monocrystalline silicon solar cells at the same applied voltage of $520\ \mathrm{mV}$. All solar cells are processed equally but exhibit a process failure at the rear and thus have different rear surface recombination velocities. Using quantum efficiency analysis, I determine the effective diffusion length of each solar cell. Figure 6.7 shows the measured (Φ_{EL}, L_{eff})-datapairs as circles. Compared to the calculated curves (green lines), a good agreement is achieved.

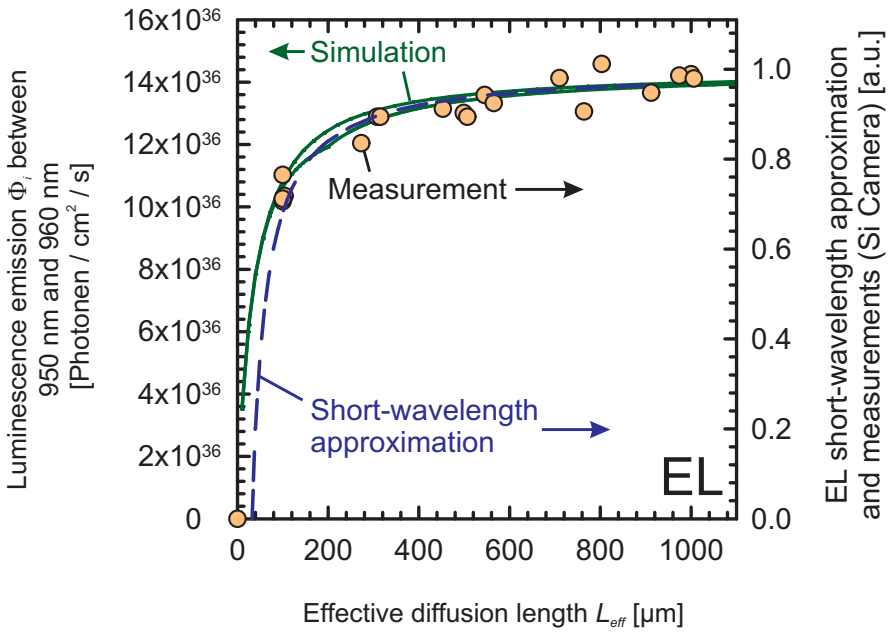

Figure 6.7: *The dependence of the luminescence emission detected between* 950 nm *and* 960 nm *on the effective diffusion length* L_{eff}*. The curves calculated with the optical model of this work (green solid lines) are in good agreement with the short-wavelength approximation (blue dotted line) and the measured values (yellow data).*

Fuyuki's approximation

The approximation of Fuyuki et al.[91] states that the measured electroluminescence photon flux Φ_{EL} is proportional to the effective diffusion length L_{eff} and thus inversely proportional to the bulk saturation current density $J_{0\mathrm{b}}$. Although this approximation has already been used in different publications,[92,93] it only holds for effective diffusion lengths considerably smaller than the solar cell's base thickness.[15,94] This approximation follows directly from the fact that the effective diffusion length L_{eff} equals the bulk diffusion length L_{b} for effective diffusion lengths smaller than $W/4$. I thus obtain with Eq. (6.17) Fuyuk's approximation

$$\Phi_{\mathrm{EL,sh}} \propto \frac{\alpha_{\mathrm{lum}} - \frac{\cos\theta_1}{L_{\mathrm{eff}}}}{\alpha_{\mathrm{lum}}^2 - \left(\frac{\cos\theta_1}{L_{\mathrm{b}}}\right)^2} \xrightarrow{L_{\mathrm{eff}} \ll \frac{W}{4}} \frac{L_{\mathrm{b}}}{\cos\theta_1}. \tag{6.25}$$

Figure 6.7 shows the dependence of the EL signal of the effective diffusion length. Fuyuki's approximation would result in a straight line through the origin, which clearly holds only for very small effective diffusion lengths.

Relation to quantum efficiency

The analysis of the external quantum efficiency Q_{EQE} in the wavelength range between $700\ \mathrm{nm}$ and $900\ \mathrm{nm}$ yields information about the diffusion properties within the solar cell base. The slope of the plot Q'^{-1}_{EQE} versus α^{-1} contains the effective diffusion length L_{eff}.[69,95]

I demonstrate that the effective diffusion length follows in the same manner from the EL spectrum. Therefore, I write

$$\widehat{\Phi}_{\mathrm{EL}}^{-1} = \frac{1}{1 - \alpha_{\mathrm{lum}}^{-1} \frac{\cos\theta_1}{L_{\mathrm{eff}}}} \approx 1 + \alpha_{\mathrm{lum}}^{-1} \frac{\cos\theta_1}{L_{\mathrm{eff}}}, \tag{6.26}$$

which reveals that the plot $\widehat{\Phi}_{\mathrm{EL}}^{-1}$ versus $\alpha_{\mathrm{lum}}^{-1}$ provides information about the effective diffusion length L_{eff}.

Rau[86] investigated the correlations between the EL spectrum and the external quantum efficiency in detail and obtained a reciprocity relation between these two quantitites. I further analyze and explain Rau's reciprocity relation in Sec. B.1 whereas Sec. B.2 shows experimental results.

6.6.4 Dependence of the EL signal on the collection length

For solar cells with a rear surface recombination velocity $S_{\mathrm{rear}} \to \infty$ and a bulk diffusion length $L_{\mathrm{b}} > 3W$, it follows from Eq. (6.2) that the minority carrier distribution decreases linearly from $z = 0$ to $z = W$, as shown in Fig. 6.8(a). Since L_{C} is the integral of the normalized minority charge carrier concentration over W, L_{C} is proportional to W in this case. Hence, according to the long-wavelength EL model given by Eq. (6.10), the camera signal should be proportional to W.

To confirm this prediction experimentally, a set of 15 monocrystalline silicon solar cells was prepared. Firstly, p-type $1.5\ \Omega\mathrm{cm}$ FZ-silicon wafers with an area of $2 \times 2\ \mathrm{cm}^2$ were etched

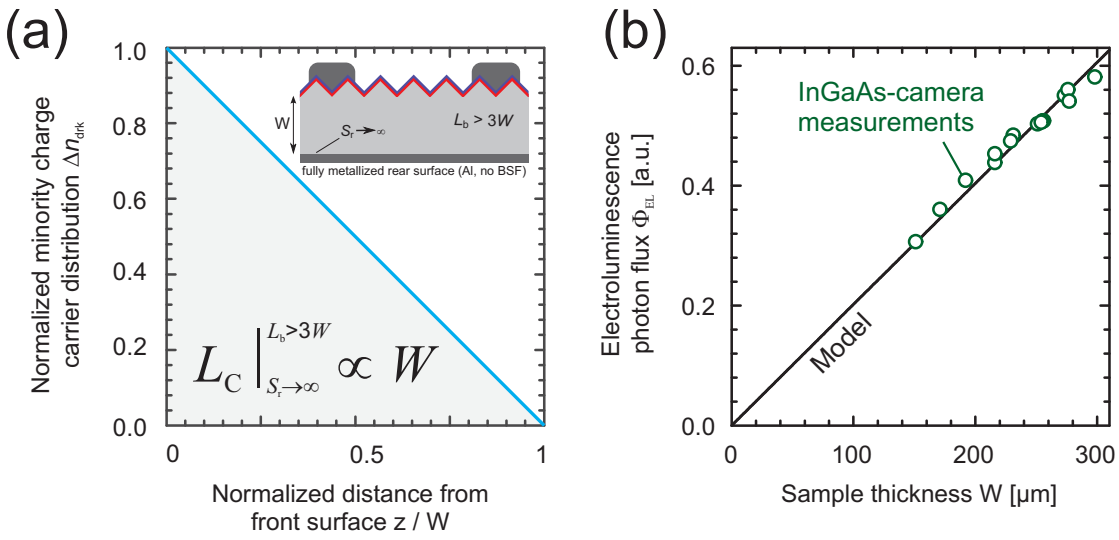

Figure 6.8: *(a) According to Eq. (6.2), the normalized minority charge carrier distribution decreases linearily from $z = 0$ to $z = W$ for the case of $L_\mathrm{b} > 3W$ and $S_\mathrm{rear} \to \infty$. The inlay shows the structure of the solar cells discussed in section 6.6.4. (b) The camera signal (circles) is proportional to the thickness of the sample, in accordance with the model given by Eq. (6.10) (solid line).*

to obtain different thicknesses between 150 and 300 µm. The solar cells were then fabricated identically on these wafers and have an unpassivated and fully metallized rear surface, providing a very high rear surface recombination velocity S_rear above 10^4 cm/s and a bulk diffusion length L_b of the minority charge carriers above 900 µm (corresponding to $L_\mathrm{b} > 3W$). Both values have been confirmed by analyzing IQE measurements. These solar cells thus provide a good approximation to the idealized case of $S_\mathrm{rear} \to \infty$. The structure of the solar cells is shown schematically as an inlay in Fig. 6.8(a).

EL measurements were carried out with the above described solar cells using the Cheetah (Indium-Gallium-Arsenide) camera, which is sensitive over the whole spectral range of EL emission (see also Fig. 2.2 on page 8). The applied voltage was 520 mV. An optical longpass filter with a cut-off wavelength of 1080 nm was mounted in front of the camera in order to restrict the detection to the long-wavelength luminescence emission. Each measurement was repeated 30 times to increase the signal-to-noise ratio. For the evaluation of the camera signal, values were averaged over 20 pixels between two fingers. Figure 6.8(b) shows the results of the measurements together with the model given by Eq. (6.10). The proportionality factor was determined using linear regression of the measured data.

The measured data is in good agreement with the model given in Eq. (6.10) and demonstrates that both the electroluminescence emission at near-bandgap wavelengths (i. e. wavelengths above 1080 nm) and the signal of the camera detecting the electroluminescence emission are proportional to the collection diffusion length L_C.

6.6.5 Superposition principle

The superposition principle[73,74] of Eq. (6.14) states that, for each depth z, the carrier density of PL-wp is the sum of the EL and PL-sc carrier densities.

In experiments it is not possible to explicitly monitor the carrier distribution within the base. However, luminescence measurements directly access the integral over the carrier distribution and may thus give an indirect proof of the superposition principle.

I analyze a silicon solar cell at various operation conditions to experimentally demonstrate the superposition principle. The solar cell under investigation is made of monocrystalline (float-zone) silicon, exhibits a textured front surface, a metalized rear with local contacts and a grid at the front (for details of the solar cell structure see Ref. 96). I measure the PL-sc, the EL and the PL-wp luminescence emission and drive the applied voltage V_{appl} for the EL and the PL-wp case from $450\ \mathrm{mV}$ up to $550\ \mathrm{mV}$ in $10\ \mathrm{mV}$ steps. For the luminescence measurement I choose the indium-gallium-arsenide (InGaAs) camera to correctly measure the PL-sc signal without any disturbance of the reflected excitation light. Note that this measurement does not depend on the investigated wavelength range of the luminescence spectrum since the superposition principle holds for each solar cell depth z.

Figure 6.9 shows the results of the measurement. The PL-sc luminescence emission Φ_{sc} is shown as a solid blue line and the subtraction

$$\Phi_{\mathrm{sub}}(V_{\mathrm{appl}}) = \Phi_{\mathrm{wp}}(V_{\mathrm{appl}}) - \Phi_{\mathrm{EL}}(V_{\mathrm{appl}}) \tag{6.27}$$

as red squares. Figure (6.9) demonstrates that for low applied voltages (up to $490\ \mathrm{mV}$) the subtracted emission Φ_{sub} is in good agreement with the measured value for Φ_{sc}.

However, for applied voltages above $490\ \mathrm{mV}$, the measured luminescence emission at short circuit conditions is smaller than the photon flux Φ_{sub}. This underestimation is explained by the impact of the solar cell's series resistance[75] $R_{\mathrm{ser},i}$ onto the local voltage. $R_{\mathrm{ser},i}$ causes a difference between the local voltage V_i and V_{appl}. However, the superposition principle of Eq. (6.14) only holds for the local voltage V_i and not for the applied voltage V_{appl}.

The local voltage V_i is

$$V_i = V_{\mathrm{appl}} \pm J_i\, R_{\mathrm{ser},i} \tag{6.28}$$

where the plus sign holds for the PL-wp case (current extraction) and the minus sign for the EL case (current injection). In the latter equation, $R_{\mathrm{ser},i}$ is the local series resistance and the current density $J_i = I/A_{\mathrm{cell}}$ accounts for the extracted/injected current I at the local position i. Consequently, the measured EL and PL-wp data pairs corresponds to different local voltages. For each data pair, Φ_{EL} is measured at a lower local voltage than V_{appl} and Φ_{wp} at a higher one. For this reason, I correct the simple V_i-dependence of the EL emission [see Eq. (6.10) and (6.17)] by

$$\Phi_{\mathrm{EL,corr}}(V_{i,\mathrm{PL}}) = \Phi_{\mathrm{EL,meas}}(V_{i,\mathrm{EL}})\, \frac{\exp\left(\frac{V_{i,\mathrm{PL}}}{V_{\mathrm{T}}}\right)}{\exp\left(\frac{V_{i,\mathrm{EL}}}{V_{\mathrm{T}}}\right)}. \tag{6.29}$$

The correction in the latter equation scales the measured EL signal to the same local voltage as the measured PL signal. Thus, both measurement become comparable.

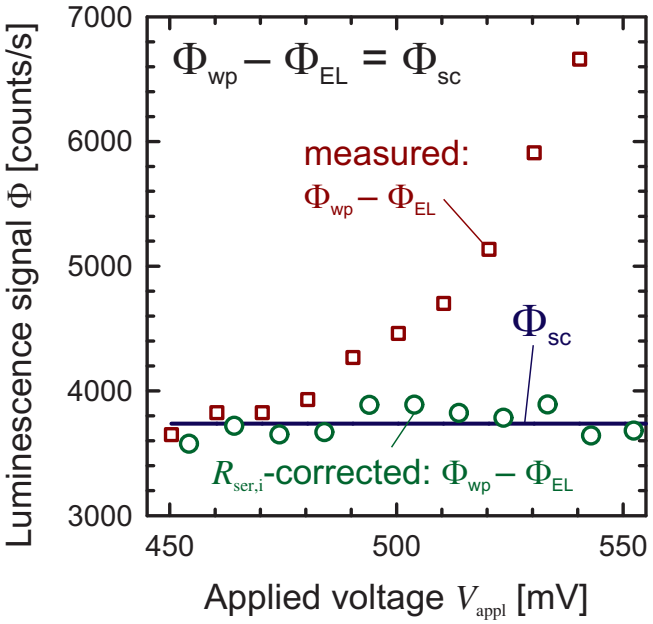

Figure 6.9: *Experimental demonstration of the superposition principle using a monocrystalline silicon solar cell: The luminescence emission Φ_{sc} at short circuit conditions (solid line) equals $\Phi_{wp} - \Phi_{EL}$. The measured data of $\Phi_{wp} - \Phi_{EL}$ (red squares) was corrected for local series resistance effects (green circles).*

To determine the necessary local voltages $V_{i,\mathrm{PL}}$ and $V_{i,\mathrm{EL}}$ I assume, that the local current density J_i equals the globally extracted/injected current I divided by the solar cell area A_{cell}. For homogeneous solar cells this is usually a good assumption. For the series resistance correction a series resistance is assumed which consequently determines the local voltages as indicated in Eq. (6.28) and allows to carry out the correction of Eq. (6.29). As a result I find that a series resistance value of $0.55\ \Omega\mathrm{cm}^2$ gives the best agreement of Φ_{sub} and Φ_{sc}: The resulting corrected values lie on a straight line, as shown in Fig. 6.9 by green circles, as expected due to the superposition principle. Note that the series resistance value of $0.55\ \Omega\mathrm{cm}^2$ is in good agreement with the value of $0.65\ \Omega\mathrm{cm}^2$ which was obtained from global IV-measurements.

6.7 Short summary

In this chapter, I analyzed the luminescence emission integral which describes the detectable luminescence photon emission of the solar cell's surface.

The resulting luminescence spectra increase strongly for short wavelengths up to a maximum of about $1155\ \mathrm{nm}$ and decreases rapidly for larger wavelengths. Compared to the spectral coefficient of radiative recombination a peak-shift of about $30\ \mathrm{nm}$ to larger wavelength follows due to the higher reabsorption probability of short-wavelength photons.

Even though the total number of photons emitted from a solar cell differs substantially at different working points (EL, PL-sc, PL-wp, PL-oc), the emitted spectra maintains mainly its

shape. Deviations can be found for wavelengths below $950\ \mathrm{nm}$ only. Similarly, base properties of the solar cell device only change the shape of the spectra within this short-wavelength range. In the long-wavelength range instead, optical properties like the roughness of the rear surface or the rear surface reflectance change the shape of the spectra.

The parameter dependences of an integrating detector (like a camera) was analyzed. Therefore, analytical solutions were found for the short- and the long-wavelength range for all working points. Regarding the electroluminescence case, it was shown that the local voltage has a substantial impact onto the detected camera signal for short-wavelength detectors. For long-wavelength detectors instead, the base and the optical properties of the solar cell device also play an important role.

Experimentally it was shown that the long-wavelength EL emission is proportional to the collection length L_{C}. Regarding the short-wavelength detection, I showed by theory and experiment that the EL signal in dependence of the effective diffusion length L_{eff} is proportional in a first approximation to $(1 - \cos\theta_1 / L_{\mathrm{eff}} / \alpha)$.

CHAPTER 7

Solar cell equivalent circuit model and series resistance imaging

Luminescence imaging allows for a fast and spatially resolved characterization of silicon wafers and solar cells.[97] As shown in the previous chapters, the luminescence emission depends exponentially on the local junction voltage. For this reason, luminescence imaging allows for a spatially resolved determination of this voltage.[7,15] Compared to non-camera-based scanning techniques like contact resistance scanning (Corescan),[98] which directly probes the surface potential, luminescence imaging is very fast and non-destructive.

Solar cells are large-area devices and a large fraction of the generated current is under usual operation conditions extracted at the terminals. As a consequence, the local junction voltage (compared to the voltage applied to the terminals) is strongly affected by the current flow to the terminals and the resistivity of the different conducting media, like finger, busbar and emitter. Using luminescence imaging, different methods for the determination of the local series resistance have been introduced.[16–20,99] All these methods require a modeling of the current flow, where the so-called independent local diode model is usually utilized.[100–103] In this model, the solar cell is split into many small local elements, which are contacted to the terminals using an independent series resistance carrying only the current of the local element itself. Even though it was demonstrated that the results based on this independent diode model are reasonable and their magnitude of the correct order,[15,20,92] it is a substantial simplification and the physical validity is not obvious at first sight.

7.1 Determination of the local junction voltage

7.1.1 Local voltage

The local voltage V_{loc} describes the splitting of the quasi-Fermi levels at every position (x, y, z) within the solar cell,

$$q\,V_{\mathrm{loc}} = \Delta E_{\mathrm{F}}. \tag{7.1}$$

The splitting ΔE_F of the quasi-Fermi level is given by

$$\Delta E_\mathrm{F} = E_\mathrm{Fn} - E_\mathrm{Fp}, \tag{7.2}$$

where E_Fn and E_Fp are the quasi-Fermi levels of the electrons and the holes, respectively. The Fermi-Dirac statistics relates the local voltage V_loc to the carrier densities n and p by

$$n \cdot p = n_\mathrm{i}^2 \cdot \left[\exp\left(\frac{V_\mathrm{loc}}{V_\mathrm{T}}\right) - 1\right], \tag{7.3}$$

where n_i is the intrinsic carrier density. For a p-type base in low-level injection with a dopant concentration N_A, the product

$$n(z) \cdot p(z) \xrightarrow{lli} \Delta n(z) \cdot N_\mathrm{A} \tag{7.4}$$

simplifies [see Eq. (3.13)]. Inserting Eq. (7.4) into Eq. (7.3) yields

$$n = \frac{n_\mathrm{i}^2}{N_\mathrm{A}} \cdot \left[\exp\left(\frac{V_\mathrm{loc}}{V_\mathrm{T}}\right) - 1\right]. \tag{7.5}$$

7.1.2 Local junction voltage

The local *junction* voltage V_i describes the splitting of the quasi-Fermi levels at the beginning of the base ($z = 0$). Here, the index i refers to the lateral position (x, y) of the solar cell. For $z = 0$ Eq. (7.5) becomes

$$n(0) = n_1 = \frac{n_\mathrm{i}^2}{N_\mathrm{A}} \cdot \left[\exp\left(\frac{V_i}{V_\mathrm{T}}\right) - 1\right] \tag{7.6}$$

for a p-type base operating under low-level injection conditions. The local junction voltage is thus a direct measure of the carrier concentration n_1 at the beginning of the base. Due to the usual assumption of a flat Fermi level in the space charge layer[68] (which yields that E_Fn is the same on both sides of the junction) the local junction voltage can be measured directly using a voltmeter by contacting the emitter and the rear surface.

7.1.3 Relative local junction voltage

A measurement of the local luminescence emission allows to determine the local junction voltage because it directly probes excess carrier densities [see Eq. (6.1)]. The local luminescence emission Φ_i can be abbreviated by [see Eq. (6.17)]

$$\Phi_i = C_i \cdot \exp\left(\frac{V_i}{V_\mathrm{T}}\right), \tag{7.7}$$

where C_i is used as a calibration constant here. All parameters which are included in C_i were determined explicitly in Sec. 6.5.2; C_i includes only parameters which do not directly depend on the local voltage. However, if injection dependent parameters are present in the investigated sample, C_i may become voltage dependent.

The local junction voltage is then extracted with Eq. (7.7) using

$$V_i = V_\mathrm{T} \cdot \ln\left(\frac{\Phi_i}{C_i}\right) = V_\mathrm{T} \ln(\Phi_i) - V_\mathrm{T} \ln(C_i). \tag{7.8}$$

A single luminescence image (Φ_i known but C_i not) thus already contains valuable information about lateral voltage differences ΔV_i if C_i is independent of i (i. e. for monocrystalline silicon solar cells). The absolute V_i value, however, still needs to be corrected for the offset.

7.1.4 Absolute local junction voltage

The absolute value of the local junction voltage can be determined from a luminescence image if the calibration constant C_i is known. Assuming that C_i does not depend on voltage, C_i can be determined if V_i equals V_appl. This assumption holds at two different operation conditions:

- For PL a luminescence image captured at open-circuit[16] conditions allows to calculate C_i because balancing currents within the emitter lead to an iso-potential over the whole solar cell. As a consequence, the measured V_oc voltage at the terminals equals the local voltage V_i. By applying the correction for diffusion-limited carriers[a] the calibration constant is

$$C_{i,\mathrm{PL}} = \frac{\Phi_{i,\mathrm{oc}} - \Phi_{i,\mathrm{sc}}}{\exp\left(\frac{V_\mathrm{oc}}{V_\mathrm{T}}\right)}. \tag{7.9}$$

  Note that V_oc in Eq. (7.9) corresponds to the same illumination intensity and spectrum as used for the PL measurement and is usually directly measured meanwhile the PL measurement is carried out. Glatthaar et al. pointed out in Ref. 15 that the correction for diffusion-limited carriers is not needed in general since $\Phi_{i,\mathrm{oc}} \gg \Phi_{i,\mathrm{sc}}$ holds in most cases.

- For EL imaging a similar procedure[104] is used. In contrast to PL the calibration constant is extracted from a luminescence image where the current fed into the solar cell is as small as possible but still allows to capture a luminescence image. The small current flow leads to negligible voltage drops over the current path and thus $V_i = V_\mathrm{appl}$ holds. The calibration constant then reads

$$C_{i,\mathrm{EL}} = \frac{\Phi_{i,\mathrm{EL}}}{\exp(\frac{V_\mathrm{appl}}{V_\mathrm{T}})}. \tag{7.10}$$

For an image of the absolute local voltage two luminescence images are thus needed. After C_i is determined either with EL or with PL the local voltage directly follows from Eq. (7.8).

[a] The diffusion-limited carriers are those which cannot be extracted from the base even at short-circuit conditions. The correction of the local PL luminescence signal for diffusion-limited carriers is carried out by subtracting the PL-sc luminescence signal, see Sec. 6.5.1 for more details.

7.2 Two-dimensional equivalent circuit models of solar cells

Aiming at a quantitative analysis of the local junction voltage (i. e. for a local series resistance determination) a model for the current flow from the local element up to the terminals is required. Such equivalent circuits have been used previously for the analysis and simulation of silicon solar cells in one[105] and two dimensions using interconnected and independent diode models.[100–103] In principle, the two-dimensional approaches split up the solar cell in many small local elements, whereas each local element can be interpreted as a miniature solar cell. Then, the elements are interconnected to each other (interconnected diode model) or to the terminals (independent diode model). Contrarily, the one-dimensional (global) equivalent circuit model just exhibits one single element for the whole cell and is not suitable to analyze images of the local junction voltage.

In this section, I firstly focus on the modeling of the local elements. Then, I discuss in detail the interconnected diode model. By assuming a voltage dependent local series resistance I transform the interconnected diode model into the independent diode model. The linearization of the voltage dependent series resistance, to allow for a simple analysis of junction voltage images, is carried out in the next section.

7.2.1 Local elements

In general, two different types of local elements are required to model electrical and optical properties of an industrial silicon solar cell. These two local elements represent

- a region with a finger or a busbar on top or
- an intermediate region.

The two local elements exhibit different local IV-characteristics. Since the aim of my studies is the description and interpretation of measured data I focus on the description of the local elements using a diode model. However, in general, the local IV-characteristics could also stem from more complex simulations[106] or from measurements.

Local two-diode model

In this work, I use the local two-diode model to describe the IV characteristics of the local elements. The local two-diode model is the adaption of the global two-diode model on local elements. I choose this model because it usually describes well the IV characteristics of mono- and multicrystalline silicon solar cells. The first diode accounts for the saturation current resulting from base- and emitter recombination and the second diode usually accounts for any deviation of the ideal first-diode behavior and may represent injection dependent parameters, recombination within the space-charge region[107,108] or an unpassivated space-charge region at the cell edges.[109]

The corresponding equivalent circuit of the local element representing a region with a finger or busbar on top is shown in Fig. 7.1(a) and the local element representing an intermediate region in Fig. 7.1(b). These circuits include

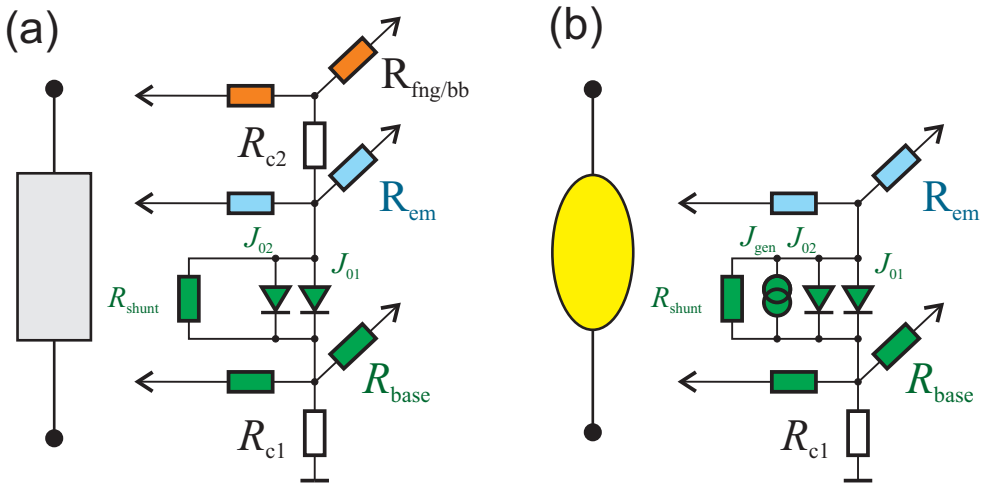

Figure 7.1: *Equivalent circuit of a local element i (a) in a region shadowed by the finger or the busbar and (b) in an intermediate region.*

- a local saturation current density $J_{01,i}$ of the first diode describing the emitter, the bulk and the rear surface recombination,
- a local second diode saturation current density $J_{02,i}$ which considers defects within the space charge region of unpassivated cell edges,
- a local shunt resistance $R_{\mathrm{sh},i}$ in parallel to the diodes,
- local series resistances $R_{\mathrm{fng/bb},i}$, $R_{\mathrm{em},i}$ and $R_{\mathrm{base},i}$, which allow for the interconnection of the local elements and
- local contact resistances $R_{\mathrm{c1},i}$ and $R_{\mathrm{c2},i}$ to contact the emitter to the finger or busbar and the rear metalization to the base.

Within the intermediate local elements [see Fig. 7.1(b)] a local photo current $I_{\mathrm{ph},i}$ describes the generation of excess carriers due to the absorption of photons within the solar cell's base. This photo current is the generation current reduced by diffusion-limited carriers which cannot be extracted from the base even at short-circuit conditions.

The photo current $I_{\mathrm{ph},i}$ is the maximum extractable current of that specific region. However, at a certain working point the extractable current

$$I_{\mathrm{extr},i} = I_{\mathrm{ph},i} - I_{\mathrm{rec},i}, \tag{7.11}$$

is the photo current reduced by the recombination current $I_{\mathrm{rec},i}$ within the local element i. $I_{\mathrm{extr},i}$ follows with the local two-diode model[105] to

$$\begin{aligned} I_{\mathrm{extr},i}(V_i) =& A_{\mathrm{loc}}\, J_{\mathrm{ph},i} - A_{\mathrm{loc}}\, J_{01,i} \exp\left(\frac{V_i}{V_{\mathrm{T}}}\right) \\ & - A_{\mathrm{loc}}\, J_{02,i} \exp\left(\frac{V_i}{2V_{\mathrm{T}}}\right) - A_{\mathrm{loc}}\, \frac{V_i}{R_{\mathrm{sh},i}}, \end{aligned} \tag{7.12}$$

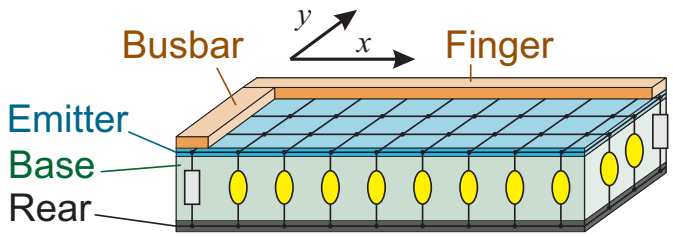

Figure 7.2: *Symmetry element of a solar cell which comprises an emitter and a finger grid at the front side of the base and a fully metalized rear contact.*

where A_{loc} is the size of the local element.

7.2.2 Model of interconnected diodes

A quite realistic approach to connect the local elements (introduced in Sec. 7.2.1) in two dimensions is shown in Fig. 7.2. The local elements are interconnected to a network using the local series resistances $R_{\mathrm{fng/bb},i}$, $R_{\mathrm{em},i}$ and $R_{\mathrm{base},i}$.

Mathematical description of the interconnected diode model

The interconnection of the local elements allows for a current exchange between local elements. Due to this interaction the current $I_{\mathrm{term},i}$ of an element i, which is extracted at the terminals, becomes

$$I_{\mathrm{term},i}(V_{\mathrm{appl}}) = I_{\mathrm{extr},i}(V_i) - I_{\mathrm{loss},i}(V_{\mathrm{appl}}). \tag{7.13}$$

Here, $I_{\mathrm{extr},i}$ is the extractable current from the local element i, as given in Eq. (7.12) and $I_{\mathrm{loss},i}$ is the current which may be supplied to any of the other elements (i.e. to a strong shunt or bad grain). While $I_{\mathrm{extr},i}$ is directly determined by the local voltage $I_{\mathrm{loss},i}$ depends on the complete solar cell configuration and is thus a function of the applied global voltage. Note that if current is supplied to another element the local voltage of that element increases. V_i fully describes the recombination of the local elements of the solar cell, hidden current losses do not exist.

In the interconnected model, the local voltage

$$\begin{aligned} V_i(V_{\mathrm{appl}}) &= V_{\mathrm{appl}} + \Delta V_{\mathrm{cpi}}(V_{\mathrm{appl}}) \\ &= V_{\mathrm{appl}} + \sum_j \int_{\mathrm{cp}_{i,j}} dS\, R_{\mathrm{cpij}}(V_{\mathrm{appl}})\, J_{\mathrm{cpij}}(V_{\mathrm{appl}}). \end{aligned} \tag{7.14}$$

scales with the applied voltage V_{appl} [mV] and with the voltage drop ΔV_{cpi} [mV] over all possible current paths $\mathrm{cp}_{i,j}$ of the i-th element (the concept of current paths is illustrated in the next section). In the latter equation, R_{cpij} [Ωcm] is the ohmic resistance of the current path $\mathrm{cp}_{i,j}$ and $J_{\mathrm{cpij}}(V_{\mathrm{appl}})$ [mAcm^{-2}] is the local current density which flows within that path.

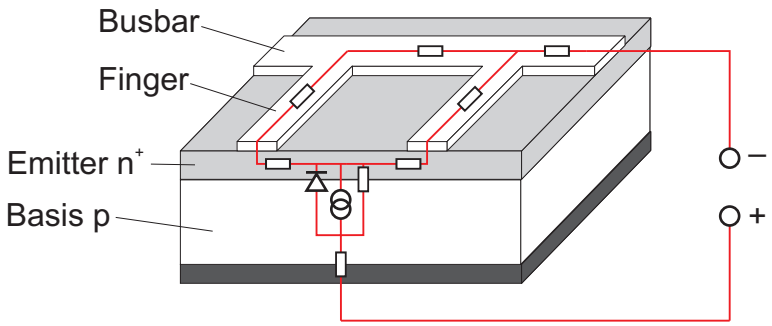

Figure 7.3: *Two possible current paths (red solid lines) and its underlying series resistances of a local element described by a diode, a current generator and a shunt resistance.*

Concept of current paths

To illustrate the concept of current paths Fig. 7.3 shows a representative region of a solar cell. The current is generated at one local element and flows within the emitter sheet resistance, the contact resistance and the finger- and busbar-resistance to the terminals. Two possible current paths of the local element are sketched in Fig. 7.3. In general, the resulting current path depends on the interaction of the different local elements and thus on numerousness parameters like the lateral distribution of series resistances, the lateral variation in base recombination and consequently even on the applied bias voltage V_{appl}. Current paths of different elements even overlap in certain series resistances like the finger and emitter-sheet resistance. As a consequence these series resistances are also called distributed[110] series resistances.

Application of the interconnected diode model

The interconnected model results in reliable values for all working points assuming that the recombination within the local elements is correctly modeled. Even though it can only be solved analytically for specific geometries,[105,111] circuit simulation programs,[112] like SPICE,[113,114] analyze conveniently these complicated networks.

The disadvantages of a circuit simulation program are the high computation time if carried out for a whole solar cell and that not all parameters are accessible by experiment.

7.2.3 Model of independent diodes

To overcome the limitations of the interconnected diode model the independent diode model, which connects each local element to the terminals using an independent series resistance, was used by different authors.[16,17,100,102,103] In contrast to the interconnected diode model each local element is directly connected to the terminals using an independent series resistance. Figure 7.4 exemplarily shows this model for three local elements.

In the following, I demonstrate that the independent local diode model directly follows from the interconnected diode model if a voltage-dependent local series resistance is assumed.

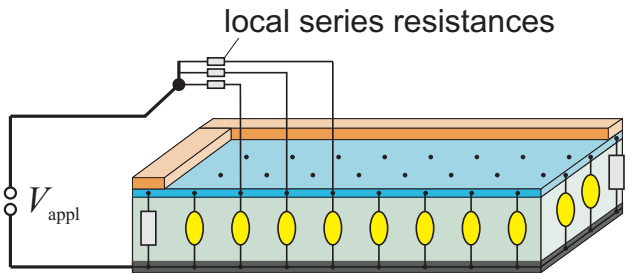

Figure 7.4: *Symmetry element of a solar cell which is modeled using the independent diode model. The connection of the local elements with an independent local series resistance is exemplarily shown for three local elements.*

As a simplification, the voltage-dependent local series resistance can be linearized in terms of the current extracted from the local element and thus approximated using an absolute and a differential part. At the end of this chapter, the validness of the independent diode model is verified using two-dimensional network simulations.

Mathematical description of the independent diode model

Within the independent diode model the voltage drop

$$\Delta V_{\mathrm{cpi}}(V_{\mathrm{appl}}) = V_i(V_{\mathrm{appl}}) - V_{\mathrm{appl}} \tag{7.15}$$

between the local and the applied voltage is caused by the current extracted from that local element flowing through an independent series resistance,

$$\Delta V_{\mathrm{cpi}}(V_{\mathrm{appl}}) = R_{\mathrm{ser},i}(V_{\mathrm{appl}}) \cdot I_{\mathrm{extr},i}(V_i). \tag{7.16}$$

Here, $R_{\mathrm{ser},i}$ is the independent series resistance and corresponds to the effective local series resistance of the current path, whereas $I_{\mathrm{extr},i}$ is the current extracted from the local element i.

By comparing Eq. (7.16) to Eq. (7.14) it becomes clear that the effective local series resistance

$$R_{\mathrm{ser},i}(V_{\mathrm{appl}}) = \frac{1}{I_{\mathrm{extr},i}(V_i)} \sum_j \int_{\mathrm{cp}_{i,j}} dS\, R_{\mathrm{cpij}}(V_{\mathrm{appl}})\, J_{\mathrm{cpij}}(V_{\mathrm{appl}}). \tag{7.17}$$

depends on the applied voltage. Since the current path $\mathrm{cp}_{i,j}$ and the local current J_{cpij} flowing in that path may change on the specific working point or applied voltage V_{appl} the local series resistance $R_{\mathrm{ser},i}$ also is a function of V_{appl}.

Application of the independent diode model

As a result of the independent diode model (marked with a star * in the following) the locally extracted current equals the extracted current at the terminals,

$$I^*_{\mathrm{term},i}(V_{\mathrm{appl}}) = I_{\mathrm{extr},i}(V_i). \tag{7.18}$$

In comparison to the current $I_{\mathrm{term},i}$ of the interconnected diode model [see Eq. (7.13)] the current loss term $I_{\mathrm{loss},i}$ does not appear in the latter equation because each local element is contacted to the terminals by an independent local series resistance.

The application of the independent local diode model, i. e. the determination of global IV characteristics, is very simple because all locally extracted currents $I_{\mathrm{extr},i}$ add up to the global current

$$I^*(V_{\mathrm{appl}}) = \sum_i I_{\mathrm{extr},i}(V_i). \tag{7.19}$$

The local voltage V_i in the latter equation scales with the applied voltage V_{appl} according to Eq. (7.16) and Eq. (7.12).

Limitations of the independent diode model

The independent diode model is the adaption of the global diode model to local measurements. This model is thus easy to understand and results in series resistance values which are directly related to the series resistances extracted from the global IV characteristics.

In contrast to the interconnected diode model the independent diode model does not consider for any current losses $I_{\mathrm{loss},i}$ which may occur for example due to the interaction of local elements. As a consequence, a strong current loss (i. e. a shunt resistance or recombination-active defects) which is only present within one local element (or one region of the solar cell) would be (wrongly) interpreted as a voltage-dependence of the local series resistance. Thus, the limitations of the independent diode model become obvious: A physical effect (in this example the current exchange between two local elements) manifests itself in a different way (a voltage dependence of the local series resistance).

7.3 Linearization of the independent diode model

The difficulty of the independent diode model using a voltage dependent series resistance, as introduced in the previous section, is that the current path and the current flow within that path are unknown in experiment. For this reason, I simplify the independent diode model and propose a linearization of the voltage dependent series resistance. The resulting model is called linearized independent diode model in the following.

7.3.1 Mathematical description

The voltage drop ΔV_{cpi} of Eq. (7.16) may be expressed as a function of the current $I_{\mathrm{extr},i}$ extracted from the local element,

$$\Delta V_{\mathrm{cpi}}(I_{\mathrm{extr},i}) = R_{\mathrm{ser},i}(I_{\mathrm{extr},i}) \cdot I_{\mathrm{extr},i}. \tag{7.20}$$

The latter equation can then be approximated in a Taylor series

$$P_{\Delta \mathrm{V_{cpi}}}(I_{\mathrm{extr},i}) = \sum_{n=0}^{\infty} \frac{\Delta V_{\mathrm{cpi}}^{(n)}(I_{\mathrm{extr},i,0})}{n!} (I_{\mathrm{extr},i} - I_{\mathrm{extr},i,0})^n \tag{7.21}$$

around a current $I_{\mathrm{extr},i,0}$. The linearization of Eq. (7.20) thus becomes

$$\begin{aligned} L_{\Delta \mathrm{V_{cpi}}}(I_{\mathrm{extr},i}) &= \Delta V_{\mathrm{cpi}}(I_{\mathrm{extr},i,0}) + \left.\frac{d\Delta V_{\mathrm{cpi}}(I_{\mathrm{extr},i})}{dI_{\mathrm{extr},i}}\right|_{I_{\mathrm{extr},i,0}} \cdot (I_{\mathrm{extr},i} - I_{\mathrm{extr},i,0}) \\ &= R_{\mathrm{abs},i} \cdot I_{\mathrm{extr},i,0} + R_{\mathrm{diff},i} \cdot (I_{\mathrm{extr},i} - I_{\mathrm{extr},i,0}). \end{aligned} \tag{7.22}$$

Here, the absolute local series resistance

$$R_{\mathrm{abs},i} = \frac{\Delta V_{\mathrm{cpi}}(I_{\mathrm{extr},i,0})}{I_{\mathrm{extr},i,0}} \tag{7.23}$$

and the differential local series resistance

$$R_{\mathrm{diff},i} = \left.\frac{d\Delta V_{\mathrm{cpi}}(I_{\mathrm{extr},i})}{dI_{\mathrm{extr},i}}\right|_{I_{\mathrm{extr},i,0}} \tag{7.24}$$

were introduced. Note that the differential series resistance does not follow from the slope of $R_{\mathrm{abs},i}(V_{\mathrm{appl}})$ but from the slope of $\Delta V_{\mathrm{cpi}}(I_{\mathrm{extr},i})$. However, if the voltage dependence of the local series resistance $R_{\mathrm{ser},i}(V_{\mathrm{appl}})$ is known, the differential series resistance at the working point $I_{\mathrm{extr},i,0}$ is

$$\begin{aligned} R_{\mathrm{diff},i}(I_{\mathrm{extr},i,0}) &= \frac{d}{dI_{\mathrm{extr},i}} \left(R_{\mathrm{ser},i} \cdot I_{\mathrm{extr},i}\right)|_{I_{\mathrm{extr},i,0}} \\ &= R_{\mathrm{abs},i} + I_{\mathrm{extr},i,0} \cdot \left(\frac{dR_{\mathrm{ser},i}}{dV_{\mathrm{appl}}} \frac{dV_{\mathrm{appl}}}{dI_{\mathrm{extr},i}} \right) \Big|_{I_{\mathrm{extr},i,0}}, \end{aligned} \tag{7.25}$$

where $I_{\mathrm{extr},i}$ follows with Eq. (7.11). The latter equation directly demonstrates that the absolute and differential series resistance exhibit the same value if the local series resistance does not depend on voltage.

Figure 7.5 illustrates a ΔV_{cpi}-$I_{\mathrm{extr},i}$-plot for a constant and a voltage-dependent local series resistance. The ratio $\Delta V_{\mathrm{cpi}}/I_{\mathrm{extr},i}$ of each datum gives the absolute series resistance while the slope $\Delta V'_{\mathrm{cpi}}(I_{\mathrm{extr},i})$ of the curve gives the differential series resistance.

The absolute local series resistance is determined by a method introduced by Trupke[16] and the differential local series resistance by a method introduced by Kampwerth.[19]

7.3.2 Application of the linearized independent diode model

The local voltage is calculated in the linear approximation from the applied voltage by

$$V_i - V_{\mathrm{appl}} = R_{\mathrm{abs},i} \cdot I_{\mathrm{extr},i,0} + R_{\mathrm{diff},i} \cdot (I_{\mathrm{extr},i} - I_{\mathrm{extr},i,0}). \tag{7.26}$$

The latter equation may even be simplified once more using just a constant, absolute series resistance,

$$V_i - V_{\mathrm{appl}} = R_{\mathrm{abs},i} \cdot I_{\mathrm{extr},i}. \tag{7.27}$$

This equation is the basis used for the determination of local series resistance mappings.[16–20,93]

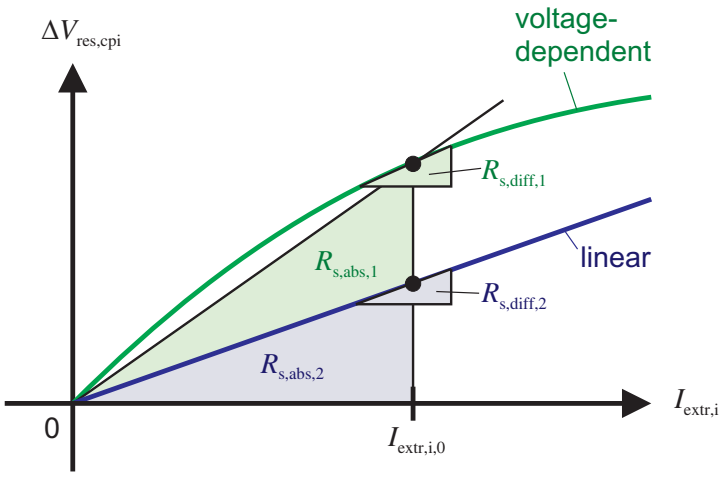

Figure 7.5: *Voltage dependent (1, green) and linear (2, blue) local series resistance.*

The approximation of Eq. (7.27) using an absolute local series resistance $R_{\mathrm{abs},i}$ corresponds to the situation that each local element is connected to the terminals by an independent, constant series resistance. The extension in Eq. (7.26), using a linear $R_{\mathrm{abs},i}$ and a differential local series resistance $R_{\mathrm{diff},i}$, allows to describe a voltage dependence of the local series resistance in a certain voltage range.

7.4 Network simulations to verify the validity of the independent diode model

To verify the validity of the independent diode model and its linearization the voltage dependence of the local series resistance is analyzed in this section. Therefore, an electrical network simulation similar to the ones presented in i. e. Ref. 115 and 116 is set up. After a short description of the network simulation and the simulated symmetry element the voltage dependence of the local series resistance is extracted for different solar cells: A monocrystalline silicon solar cell with and without broken fingers and local shunt resistances and a multicrystalline silicon solar cell.

7.4.1 Simulated symmetry element

The general-purpose circuit simulation program SPICE[113,114] (Simulation Program with Integrated Circuits Emphasis) is used to simulate one symmetry element of a solar cell. This symmetry element consists of $31 \cdot 17 = 527$ interconnected local elements. A three-dimensional sketch of this symmetry element is shown in Fig. 7.2. To account for the regions with metal (finger or busbar) on top and the intermediate regions two different types of local elements are used (marked with a gray rectangle and a yellow ellipse).

SPICE attempts to find an approximations to the system-describing differential equations.

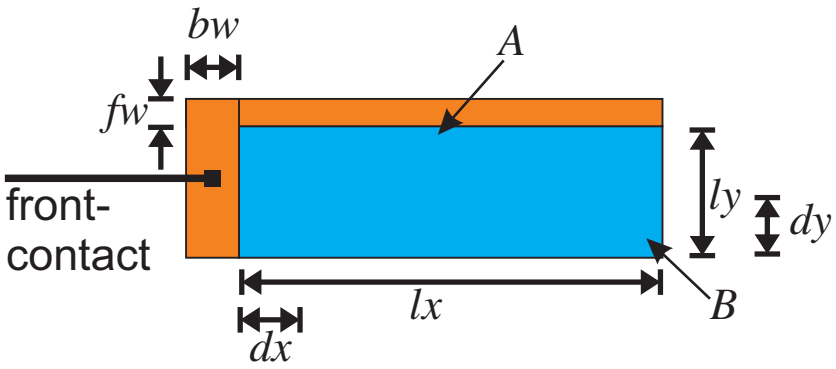

Figure 7.6: *Top-view of the symmetry element simulated with SPICE.*

It is thus able to fully simulate the interconnected diode model introduced in Sec. 7.2.2. The parameters of the simulation and of the symmetry element are summarized in Tab. 7.1 and Fig. 7.6 shows a top-view of the used geometry.

7.4.2 Voltage dependence of the local series resistance

Various voltages ranging from zero up to the open-circuit voltage are applied to the terminals of the simulated symmetry element. For each voltage, the effective series resistance is calculated for the local element i using

$$R_{\mathrm{ser},i}(V_{\mathrm{appl}}) = \frac{V_i - V_{\mathrm{appl}}}{I_{\mathrm{extr},i}(V_i)}. \tag{7.28}$$

The local voltages and currents are extracted at two local positions, which are marked in Fig. 7.6 with A and B. While position A is very close to the finger, position B is the most distant point to the contacts for this symmetry element. The locally extracted current is directly calculated with Eq. (7.12).

Besides the local series resistances the simulation determines the global light-IV and J_{sc}-V_{oc} characteristics. The analysis of these characteristics yields a global series and global shunt resistance as well as the maximum-power-point voltage.[55,117]

Monocrystalline silicon solar cell

Figure 7.7 shows the voltage dependence of the local series resistance for the simulated symmetry element (see Tab. 7.1 and Fig. 7.6). The light-IV and J_{sc}-V_{oc} analysis determines a global series resistance of $0.49\ \Omega\mathrm{cm}^2$. For voltages smaller than V_{mpp} the local series resistances at positions A and B have constant values of $0.13\ \Omega\mathrm{cm}^2$ and $0.74\ \Omega\mathrm{cm}^2$, respectively.

For voltages above $530\ \mathrm{mV}$ the effective series resistance first slightly rises and then rapidly decreases to zero at $620\ \mathrm{mV}$, which is the global open-circuit voltage. As a consequence of the open-circuit condition the locally extracted current $I_{\mathrm{extr},i}$ becomes zero as well as the voltage drop between the local and the applied voltage. Thus the ratio of these two values, which determines

Table 7.1: *SPICE simulation parameters.*

parameter	**value**
Illuminated base width lx	$31\ \mathrm{mm}$
Illuminated base height ly	$1.36\ \mathrm{mm}$
x-Resolution dx	$1\ \mathrm{mm}$
y-Resolution dy	$0.08\ \mathrm{mm}$
Half finger width fw	$80\ \mu\mathrm{m}$
Half busbar width bw	$1000\ \mu\mathrm{m}$
Busbar & Finger height	$12.5\ \mu\mathrm{m}$
Specific finger and busbar resistance	$3 \times 10^{-6}\ \Omega\mathrm{cm}$
Contact resistance to emitter	$0.003\ \Omega\mathrm{cm}^2$
Emitter sheet resistance	$50\ \Omega/\mathrm{sq}$
Shunt resistance	$1 \times 10^{10}\ \Omega\mathrm{cm}^2$
Specific base resistance	$1.5\ \Omega\mathrm{cm}$
$J_{01,i}$	$1000\ \mathrm{fA/cm}^2$
$J_{02,i}$	$0\ \mathrm{fA/cm}^2$
$J_{\mathrm{ph},i}$	$36\ \mathrm{mA/cm}^2$

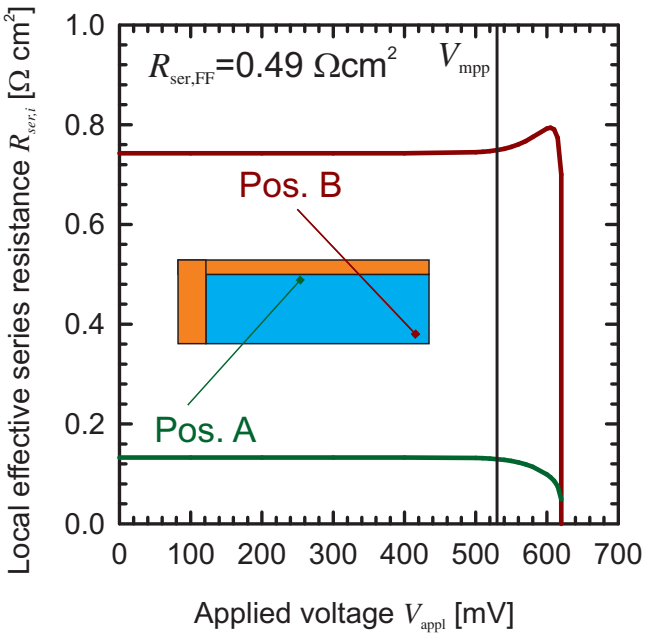

Figure 7.7: *Local effective series resistance for the positions A and B of the symmetry element shown in the inset.*

the local series resistance [see Eq. (7.28)], becomes meaningless at and close-to open-circuit conditions. Note that at these working points also the independent diode model itself does not hold any more because the current $I_{\mathrm{loss},i}$ becomes much larger than $I_{\mathrm{extr},i}$.

Figure 7.7 demonstrates that for this symmetry element the approximation of a constant local series resistance holds very well for voltages from zero up to the maximum-power-point voltage V_{mpp}. For voltages higher than V_{mpp} the approximation is not valid. It is thus not possible to describe the whole IV-characteristics of a solar cell with the constant series resistance approximation [see Eq. (7.27)] of the independent diode model.

Monocrystalline silicon solar cell with a broken finger

The symmetry element of the SPICE simulation is modified to account for high local series resistances. Therefore, a finger cut is simulated at a specific distance from the busbar (see inset in Fig. 7.8). The symmetry element thus exhibits globally and locally higher series resistance values.

The finger cut is simulated at a distance of $29\ \mathrm{mm}$ to the busbar, which is close to the total width of the finger ($31\ \mathrm{mm}$). As a consequence, the global series resistance increases to $1.1\ \Omega\mathrm{cm}^2$. Figure 7.8 shows the voltage dependence of the local series resistances at position A and B. Qualitatively, a similar behavior as in Fig. 7.7 is obtained. However, the local series resistance of position B is way higher ($3.9\ \Omega\mathrm{cm}^2$) and the maximum between the maximum-power-point and the open-circuit voltage is more pronounced. The increase even starts at voltages smaller than the

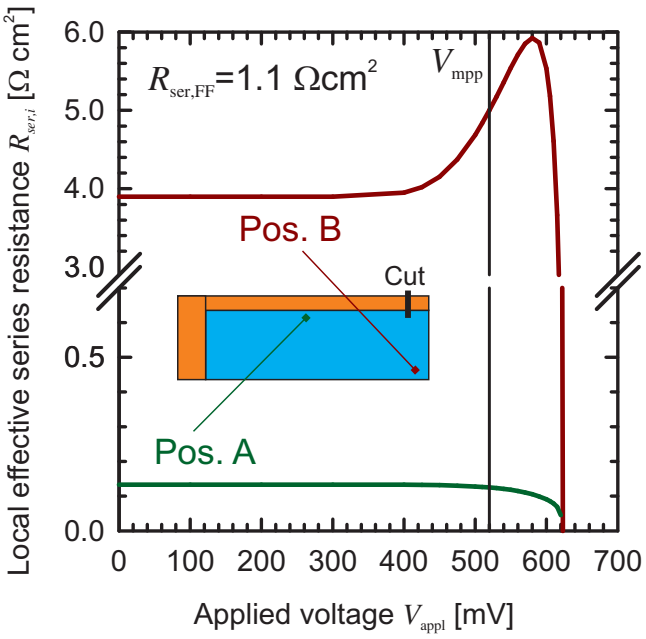

Figure 7.8: *Local effective series resistance for the positions A and B of the symmetry element shown in the inset. The finger is cut at a distance of* $29\ \mathrm{mm}$ *to the busbar to simulate a high local series resistance.*

maximum-power-point voltage. This distortion is a direct consequence of the interconnection of the local elements and the overlapping of different current paths.

Figure 7.8 thus demonstrates that the constant series resistance approximation of the simulated symmetry element with a broken finger holds well for position A but only for voltages up to $400\ \mathrm{mV}$ for position B. At the maximum power point voltage, the absolute and the differential series resistance has to be considered for position B, as given in Eq. (7.26).

Monocrystalline silicon solar cell with a local shunt resistance

I modify the simulation to account for a local shunt resistance which I place in the center region of the symmetry element (see inset in Fig. 7.9). The local shunt fulfills one local element (size $dx \cdot dy$) and exhibits a value of $1\ \Omega\mathrm{cm}^2$. As a result, the global shunt resistance follows to $560\ \Omega\mathrm{cm}^2$. Note that the series resistance ($R_{\mathrm{ser,FF}}$) increases although no modifications to the local series resistances or to the finger were carried out.

The resulting local series resistances are shown in Fig. 7.9. It is shown, that local shunt resistances of this strength do not have any influence on the local series resistance value since the resulting curves are very similar to the ones obtained in Fig. 7.7.

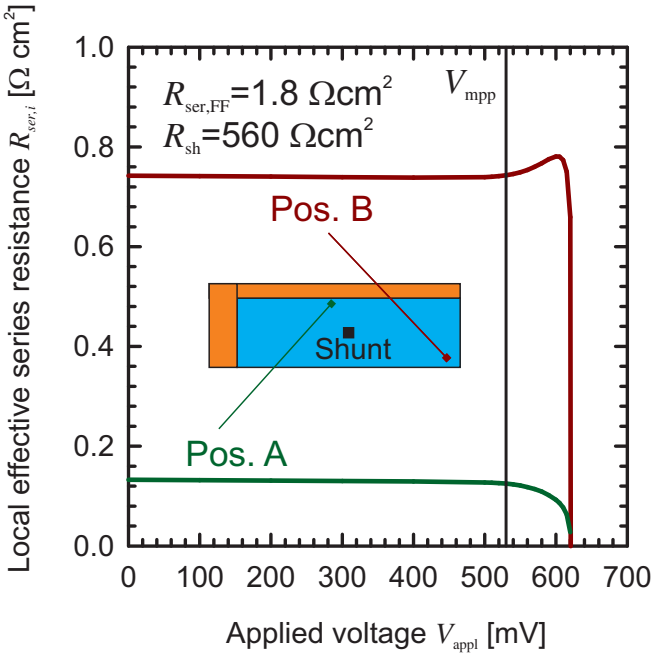

Figure 7.9: *Local effective series resistance for the positions A and B of the symmetry element shown in the inset. A strong local shunt resistance is placed in the center region.*

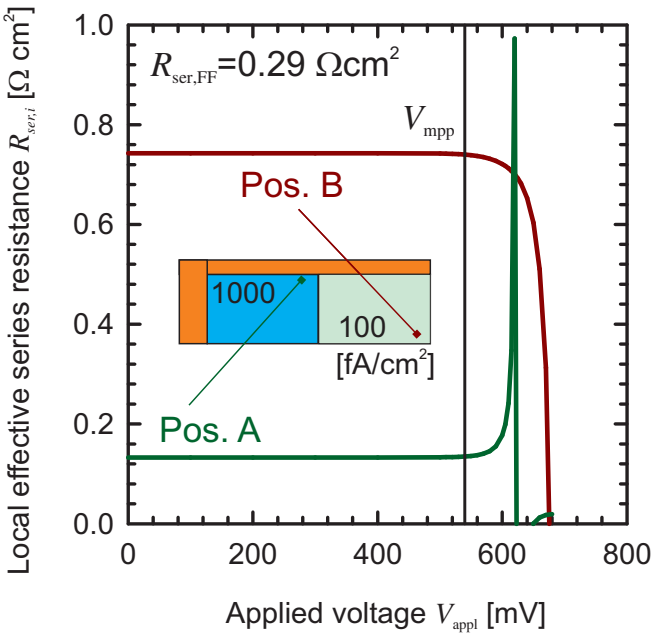

Figure 7.10: *Local effective series resistance for the positions A and B of the symmetry element shown in the inset. The symmetry element exhibits two regions of different diode qualities.*

Multicrystalline silicon solar cell

To model multicrystalline material I split the simulated symmetry element into two regions of equal size. The region close to the busbar (bad grain) exhibits a saturation current density of the first diode of $1000\ \mathrm{fA/cm^2}$ and the other region (good grain) of $100\ \mathrm{fA/cm^2}$.

The resulting curves are shown in Fig. 7.10. In comparison to the monocrystalline solar cell simulation of Fig. 7.7 the curves of the local series resistances are very similar. Only at and around open-circuit conditions the curves show a different behavior. While the asymptotic behavior of the curve of position A is very strong and at voltages smaller than V_{oc}, the curve of position B is continuous. This effect results from the different diode qualities in the two regions: At open circuit conditions the region of $100\ \mathrm{fA/cm^2}$ supplies current to the region of $1000\ \mathrm{fA/cm^2}$. The extracted current for position B thus hardly becomes zero.

7.4.3 Results

The results for the simulated types of silicon solar cells show that the independent model is physically valid in a wide voltage range. It describes all four types from short-circuit up to maximum power point conditions in exception of the simulated solar cell exhibiting a broken finger. This cell can only be described up to voltages of $400\ \mathrm{mV}$. Regarding voltages above the maximum power point, the independent diode model does not hold any more. The current exchange between different local elements manifests itself as a voltage dependence of the local

series resistance.

7.5 Series resistance imaging

The results of the network simulations show that the independent diode model can be applied for the analysis of measured luminescence images to determine images of the local series resistance.

7.5.1 Discussions of different series resistance imaging methods

All luminescence-based series resistance methods introduced so far are based on the determination of the local voltage (see Sec. 7.1). They use the independent diode model to determine a resistance accounting for the voltage drop from the terminals to the local region and the locally extracted current. It thus gives exactly the local series resistance $R_{\mathrm{ser},i}$ introduced in the previous section.

For the determination of the local series resistance of multicrystalline silicon solar cells photoluminescence (PL) based methods[16,19,20] are preferred because they are able to separate $R_{\mathrm{ser},i}$ and $J_{0,i}$.[20,116] All introduced methods based on electroluminescence (EL) imaging only[18,92,93] are not able to separate $R_{\mathrm{ser},i}$ and $J_{0,i}$ conveniently. It was shown analytically[15] that these methods do only determine the product of $R_{\mathrm{ser},i}$ and $J_{0,i}$.

Fuyuki's assumption[91] was used in Ref. 92 and 93 to separate $R_{\mathrm{ser},i}$ and $J_{0,i}$. However, as already shown in Sec. 6.6.3, this assumption is not applicable to most industrial solar cells because it only holds for solar cells with effective diffusion lengths much smaller than the thickness of the device.

7.5.2 Series resistance imaging of a multicrystalline silicon solar cell

I use the definition of the absolute local series resistance in Eq. (7.23) to calculate the local series resistance from images of the local junction voltage. These images are generated from PL images, as explained in Sec. 7.1.4. In total, four PL images are required: A PL-oc- and a PL-sc-image at a small illumination intensity to calculate the calibration constant C_i and a PL-wp- and a PL-sc-image to determine the voltage drop ΔV_i. The parameters J_{01}, J_{02} and R_{sh}, necessary to model the recombination within the local elements in Eq. (7.23), are extracted from the global J_{sc}-V_{oc} characteristics. The method chosen in this section is thus very similar to the one introduced by Trupke et al.[16]

I investigate in a multicrystalline silicon solar cell to demonstrate the capability to separate local series resistance effects from variations in the bulk recombination. Figure 7.11 shows a photoluminescence image at working point conditions (PL-wp). The illumination is set to two-thirds of a sun and the applied voltage is $500\ \mathrm{mV}$, well below the open-circuit voltage of this solar cell. Clearly visible in Fig. 7.11 are lines of low luminescence emission. Those lines are dislocation networks of high recombination activity. The busbar and fingers appear with a dark contrast because the luminescence photons cannot emerge from the solar cell at this places.

Figure 7.12 shows the resulting series resistance mapping of this multicrystalline silicon solar cell. While the structure of the multicrystalline material nearly vanishes in this image the local series resistance becomes clearly visible. Due to the definition of the local series resistance along

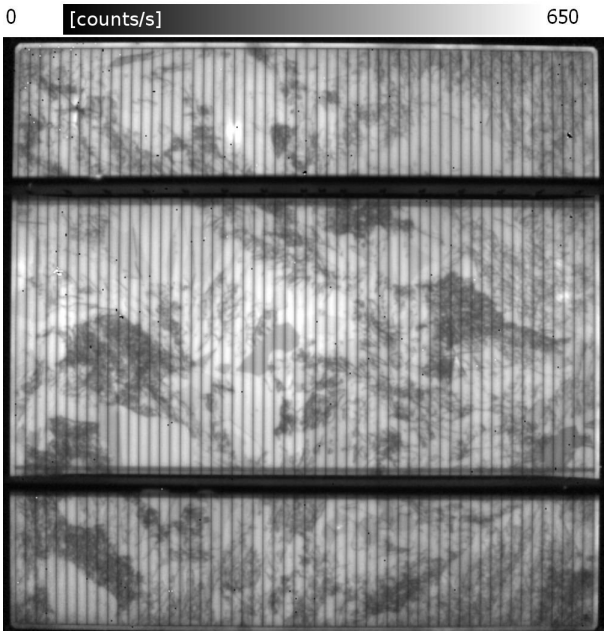

Figure 7.11: *Photoluminescence image at working-point conditions of a multicrystalline solar cell.*

the current path the local series resistance is smaller at regions close to the busbar and exhibits its largest value at the most distant point to the busbar. This is clearly visible in Fig. 7.12, where regions close to the busbar exhibit values around $0.4\ \Omega\mathrm{cm}^2$ and regions in-between the busbar of $1.0\ \Omega\mathrm{cm}^2$. In addition, small defects of the finger grid become visible in Fig. 7.12 at the left side in-between the busbars.

7.6 Short summary

After a short introduction how local junction voltages are extracted from EL and PL images, I discussed equivalent circuits of different local regions of a solar cell. I explained the interconnected diode model, which depends on local elements connected to each other and to the terminals. Analytical equations, which describe the flow of the current generated in the local element to the terminals were obtained.

By interpreting the voltage drop between the terminals to be caused by a local series resistance, the transition of the interconnected to the independent diode model was made. In general, this local series resistance dependes on voltage. I could express this voltage dependence using a Taylor series and thus a linearization was obtained, which describes the local series resistance by an absolute and a differential one.

To verify the physical validity of the independent local diode model various types of solar cells have been modeled using network simulations. The results showed that the independent local diode model can be used to describe a wide variety of solar cells from short-circuit up to

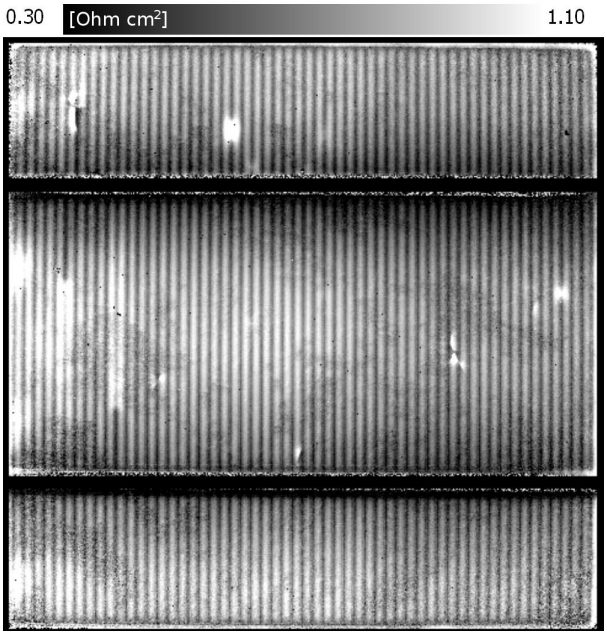

Figure 7.12: *Series resistance image of a multicrystalline solar cell extracted from photoluminescence images.*

maximum power point conditions. However, for applied voltages at and close-to open-circuit conditions the independent diode model does not hold any more and current exchange between local elements wrongly manifests itself as a voltage dependence of the local series resistance.

Finally, a series resistance image was determined for a multicrystalline silicon solar cell. It was shown that the series resistance effects are separated well from lateral variations in the bulk material.

CHAPTER 8

Local impact analysis (LIA)

Efficiency improvements are one of the main concerns in any solar cell production environment. Solar cell characterization techniques identify the dominant loss mechanism and thus help to evaluate, which parts of the solar cell has to be improved. Even though global solar cell characterization techniques are commonly applied to silicon solar cells, spatially resolved methods often yield more information since solar cells are large-area devices. While quantitative spatially resolved methods are well established, the impact onto the global energy conversion efficiency η still remains unclear in most cases.

To overcome this limitation, I propose in this chapter a simple two-dimensional analysis to model the impact of parameter mappings onto the solar cell efficiency. Measured local or global parameters such as the saturation current densities of the diodes, the series resistance and the shunt resistance can be fed into this *local impact analysis* (LIA). Based on these parameters, LIA calculates a new light-IV characteristics and thus determines a new global energy conversion efficiency. All parameters (including the parameter mappings) can be manipulated virtually and fed into LIA again to determine the impact of specific lateral variations onto η.

8.1 Introduction

8.1.1 Global solar cell characterization

The characterization technique most often applied to solar cells is the measurement of the global current-voltage (IV) characteristics under one-sun illumination (light-IV). The analysis of this characteristics yields fundamental solar cell parameters such as the energy conversion efficiency η, the open circuit voltage V_{oc}, the short circuit current density J_{sc} and the fill factor FF. If additionally the J_{sc}-V_{oc} characteristics[118] is analyzed, parameters of the two-diode model[105] such as the saturation current densities of the first (J_{01}) and second diode (J_{02}), the series resistance[119] R_{ser} and the shunt resistance R_{sh} are extracted.[120] Figure 8.1 exemplarily shows

solar cell A:

parameter	**value**
η	16.0 %
J_{sc}	35.5 mA/cm^2
V_{oc}	620 mV
FF	72.8 %
Pseudo-FF	81.5 %
$R_{ser,FF}$	1.85 Ωcm^2
J_{01}	900 fA/cm^2
J_{02}	33000 pA/cm^2
R_{sh}	7400 Ωcm^2

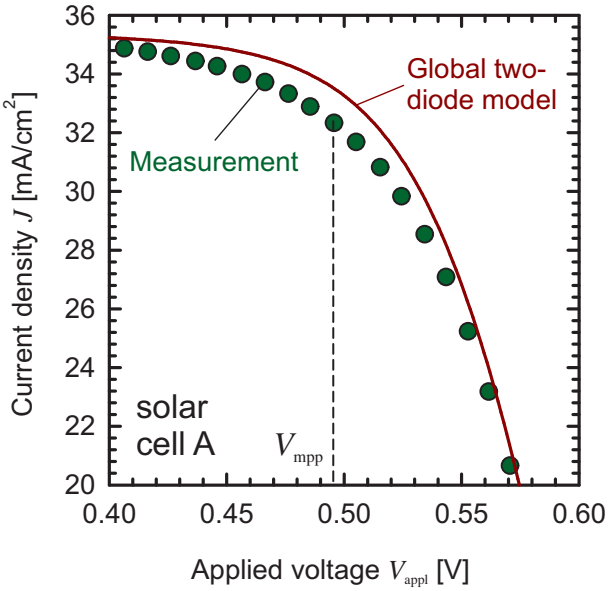

Figure 8.1: *Light-IV characteristics of solar cell A and its fundamental parameters extracted from the light-IV and J_{sc}-V_{oc} characteristic.*

the light-IV characteristics of a poorly processed industrial screen-printed monocrystalline silicon solar cell (named solar cell A in the following) and its fundamental parameters.

The comparison of the measured parameters to the parameters expected from simulation or from previous experiments may allow to identify the efficiency-limiting parameter. Solar cell A (see Fig. 8.1) seems to suffer from a high series resistance. However, without any further analysis, it remains unclear where this high series resistance stems from. In addition, the analysis of global parameters alone is often not sufficient, since the description of the IV characteristics is inconsistent. This inconsistency becomes obvious in Fig. 8.1 where the measured and a simulated light-IV characteristics is shown. For the simulated light-IV characteristics the parameters J_{01}, J_{02} and R_{sh} were determined with a least-square regression of the two-diode model to the measured data of the J_{sc}-V_{oc} characteristics, the series resistance $R_{ser,FF}$ followed from the light-IV and J_{sc}-V_{oc} characteristics and J_{sc} directly from the measured light-IV characteristics. The comparison of the simulated to the measured light-IV characteristic in Fig. 8.1 demonstrates, that the global two-diode model does not describe well this solar cell.

8.1.2 Spatially resolved characterization techniques

Solar cells are large-area devices and thus lateral variations of recombination and resistance parameters play an essential role and can affect substantially the global power conversion efficiency.

The local series resistance (see chapter 7), for example, varies for every solar cell, since the generated electrons have to be transported from the place of generation to the terminals. On this way, the electrons suffer from different series resistance contributions like the emitter sheet resistance, contact resistances and the finger resistance. For multicrystalline silicon solar

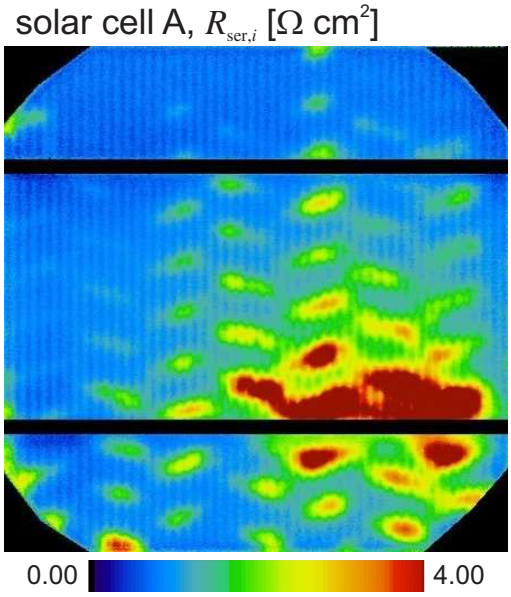

Figure 8.2: *Series resistance image of solar cell A.*

cells another lateral inhomogeneity comes into play: The recombination of carriers within the bulk varies strongly from grain to grain and thus leads to lateral inhomogeneous recombination currents.

Several solar cell characterization techniques exist to characterize lateral variations of specific solar cell parameters. Among them are scanning and camera-based techniques which for example determine local effective diffusion lengths,[121] local shunt resistances[122] and local series resistances.[16–20,99] Based on these techniques one can localize material or process induced faults. However, the determined local values do not allow a direct and quantified insight into the impact of the local values onto the global performance of the solar cell.

Figure 8.2 shows the series resistance mapping of the solar cell A. Using this mapping, it becomes clear that the origin of the high series resistance stems from a high contact resistance induced by an inhomogeneous firing temperature. However, it remains unclear, in which amount these high local series resistances decrease the global energy conversion efficiency.

To overcome this limitation I propose in this chapter a simple two-dimensional analysis, the *local impact analysis* (LIA).

8.2 Local impact analysis

8.2.1 Mathematical description

For the local impact analysis (LIA) the model of independent diodes as introduced in Sec. 7.2.3 is used. Within this model the solar cell is split up laterally in many small local elements which are connected with an independent series resistance to the terminals. The local voltage [see

Eq. (7.27)]

$$V_i = V_{\mathrm{appl}} + R_{\mathrm{ser},i} \cdot I_{\mathrm{extr},i} \tag{8.1}$$

of each local element directly follows with the voltage V_{appl}, applied to the solar cell terminals, and the local series resistance $R_{\mathrm{ser},i}$. In the latter equation, $I_{\mathrm{extr},i}$ gives the local current which is extracted from the local element i.

In the following, I use the local two-diode model for parameterizing the local IV characteristics of a local element i, as discussed in more detail in Sec. 7.2.1. The local two-diode model includes a local saturation current density $J_{01,i}$ of the first diode describing the emitter, the base and the rear surface recombination, a local second diode current density $J_{02,i}$ which considers defects within the space charge region and a local shunt resistance $R_{\mathrm{sh},i}$ in parallel to the diodes. A local photo current $I_{\mathrm{ph},i}$ accounts for the generation of excess carriers due to the absorption of photons within the solar cell base and is the maximum extractable current of that specific region. The local voltage V_i is the junction voltage of the local element and fully describes the current losses

$$I_{\mathrm{rec},i}(V_i) = A_{\mathrm{loc}}\, J_{01,i} \exp\left(\frac{V_i}{V_{\mathrm{T}}}\right) + A_{\mathrm{loc}}\, J_{02,i} \exp\left(\frac{V_i}{2V_{\mathrm{T}}}\right) + A_{\mathrm{loc}}\, \frac{V_i}{R_{\mathrm{sh},i}} \tag{8.2}$$

within the local element, where A_{loc} is the size of the local element. The current

$$I_{\mathrm{extr},i}(V_i) = I_{\mathrm{ph},i} - I_{\mathrm{rec},i} \tag{8.3}$$

is extracted from the local element i.

Within the model of independent diodes all locally extracted currents $I_{\mathrm{extr},i}$ add up to the global current

$$I(V_{\mathrm{appl}}) = \sum_i I_{\mathrm{extr},i}(V_{\mathrm{appl}}) \tag{8.4}$$

extracted at the terminals (see Sec. 7.2) and thus gives a light-IV characteristics which can be further analyzed.

8.2.2 Application schema of LIA

To calculate the global IV characteristics as indicated in Eq. (8.4) and Eq. (8.2), all parameters have to be determined first. Parameters, which are available as mappings, have to be matched by means of scaling, rotation and translation. Note that A_{loc} is limited by the measurement technique having the lowest resolution. Since Eq. (8.2) is given implicitly for V_{appl} I apply Newton-Raphson's method. Already after a few iterations a value for the local current $I_{\mathrm{extr},i}(V_{\mathrm{appl}})$ follows with a very high precision. As indicated in Eq. (8.4) the local currents from all local elements are consequently added up to the global current. Thus, one IV data pair of the global IV characteristics is obtained.

The analysis scheme carried out in this work is shown in Fig. 8.3. At first, all needed measurements (series resistance mapping, J_{sc}-V_{oc} and light-IV characteristics) are obtained from measurements or from simulation. These data is then analyzed separately to extract J_{01}, J_{02},

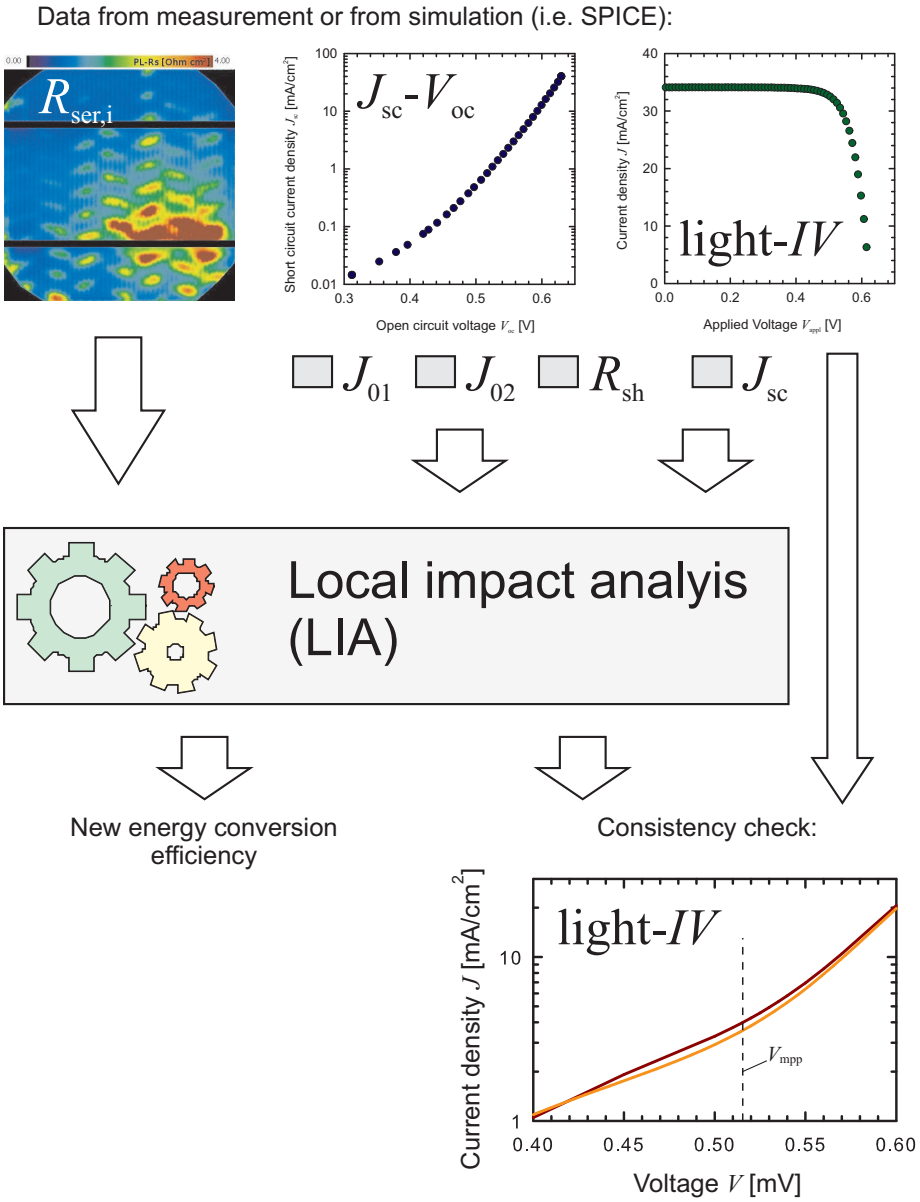

Figure 8.3: *Schematic for the analysis of monocrystalline silicon solar cells which suffer from high local series resistances.*

R_{sh} and J_{ph}. Consequently, the resulting values and the series resistance mapping is fed into Eq. (8.4). As a result a new IV curve is obtained. As a consistency check, this new IV curve is compared to the measured light-IV curve.

I calculate IV data pairs in 2 mV steps around the maximum power point. It is sufficient for LIA to analyze only voltages at and around the maximum power point voltage. Moreover, due to injection dependent parameters, it is not possible to calculate the complete IV characteristics in general. Consequently, for a reliable LIA calculations, all measured parameters have to correspond to the injection conditions at the maximum power point.

8.2.3 Parameter determination

The presented analysis can be performed with all parameters given as local parameters in a parameter mapping. However, in this work, my focus lies on industrial monocrystalline silicon solar cells which suffer from high local series resistances. Consequently, a parameter mapping of the effective series resistance $R_{\mathrm{ser},i}$ is of mayor interest. For all other parameters like $J_{\mathrm{ph},i}$, $J_{01,i}$, $J_{02,i}$ and $R_{\mathrm{sh},i}$ global (lateral homogeneous) parameters are sufficient in a good approximation.

Series resistance mapping

A series resistance mapping is crucial for the application of LIA. This mapping is extracted from PL imaging as discussed in detail in Sec. 7.5.

Light-IV characteristics

From the global light-IV characteristics the short circuit current density J_{sc} is determined which in good approximation equals the photo current density J_{ph} for moderate series resistance values.

Jsc-Voc characteristics

The global J_{sc}-V_{oc}-characteristics is used to determine the saturation current densities of the first and the second diodes, J_{01} and J_{02}, and the shunt resistance R_{sh}. Since the J_{sc}-V_{oc}-characteristics is not affected by moderate series resistances values a least-square regression of the two-diode model results in physically realistic values for standard industrial solar cells.

8.2.4 Physical validity

The resulting light-IV characteristics from LIA [see Eq. (8.4)] has to be compared to the experimentally measured light-IV characteristics around the maximum power point voltage. I take a good agreement of the model data with the experimental data as a strong indication for:

1. The physical validity of the used parameters and
2. the applicability of the model of independent diodes.

A good agreement therefore is important to rely on the determined values of the power loss analysis and to be able to virtually manipulate the data.

8.3 Verifying the applicability of LIA

To verify the applicability of LIA I first carry out network simulations. The focus of this verification lies on monocrystalline solar cells which suffer from a high local series resistance, which i. e. might be the result of a broken finger. For a realistic network simulation of the solar cell device I use the interconnected diode model which is solved by SPICE (see Sec. 7.4).

8.3.1 Simulated symmetry element

The simulations are carried out with the same symmetry element as already used in Sec. 7.4. It consists of $31 \cdot 17 = 527$ interconnected local elements. A sketch of this symmetry element is shown in Fig. 7.2. The parameters of the simulation and of the symmetry element are summarized in Tab. 7.1 and Fig. 7.6 shows a top-view of the used geometry. The symmetry element of the SPICE simulation is modified in this section to account for high local series resistances. Therefore, a finger cut is simulated at various distances from the busbar. The symmetry element thus exhibits globally and locally higher series resistance values.

The simulation is carried out for different voltages and illumination intensities to obtain the light-IV and the J_{sc}-V_{oc} characteristics. At the maximum power point voltage a series resistance image is extracted. The analysis of the light-IV and the J_{sc}-V_{oc} characteristics yield the global parameters needed for LIA (see previous section). The series resistance image and the determined parameters are consequently fed into LIA as indicated in the application schema in Fig. 8.3 and determines a new light-IV characteristics and consequently a new energy conversion efficiency.

8.3.2 Network simulations with varying local series resistances

Figure 8.4 shows the resulting energy conversion efficiencies of the analysis of the light-IV characteristics obtained from SPICE directly (x-axis) and obtained from LIA (y-axis). It can be seen in Fig. 8.4, that both results are in agreement for the analyzed range of series resistances. However, small series resistance values ($< 1.2\ \Omega\mathrm{cm}^2$) are in better agreement than higher values. This is consistent to the simulations carried out in chapter 7, where I observed that the use of just the absolute series resistance approximation is not sufficient at the maximum power point for solar cells exhibiting high local series resistance.

For the highest global series resistance value of $R_{\mathrm{ser,FF}} = 2.3\ \Omega\mathrm{cm}^2$ Fig. 8.5 shows the light-IV characteristics of LIA and SPICE in linear and logarithmic (small inset) scale. The light-IV characteristics obtained from LIA is in good agreement with the light-IV curve directly obtained with SPICE. Note that the global one or two-diode model is not able to reproduce the recombination properties (see Fig. 8.1) and would thus lead to wrong conclusions.

I conclude that LIA can be applied to solar cells with small and moderate series resistance values ($R_{\mathrm{ser,FF}} < 1.2\ \Omega\mathrm{cm}^2$).

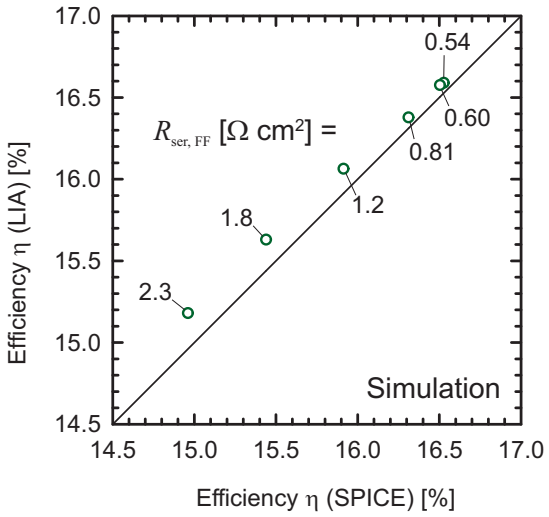

Figure 8.4: *Simulation carried out with SPICE to demonstrate the LIA approach. The x-axis gives the efficiency obtained from SPICE and the y-axis the efficiencies calculated with LIA. For LIA I used a series resistance image and global parameters determined from the light-IV and the J_{sc}-V_{oc} characteristics.*

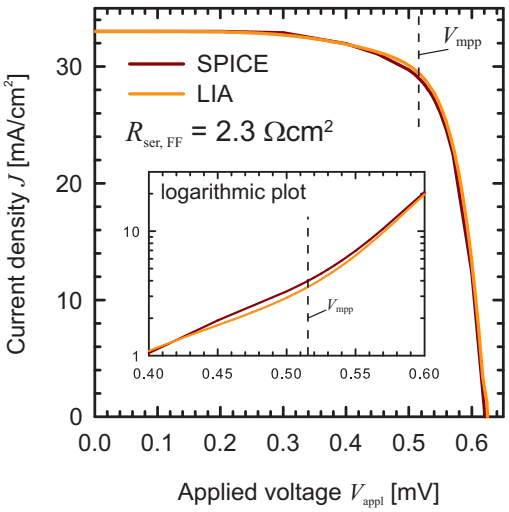

Figure 8.5: *Light-IV curves calculated with LIA and SPICE for one symmetry element of a monocrystalline silicon solar cell. The inset shows the data around the maximum power point voltage in a logarithmic scaling.*

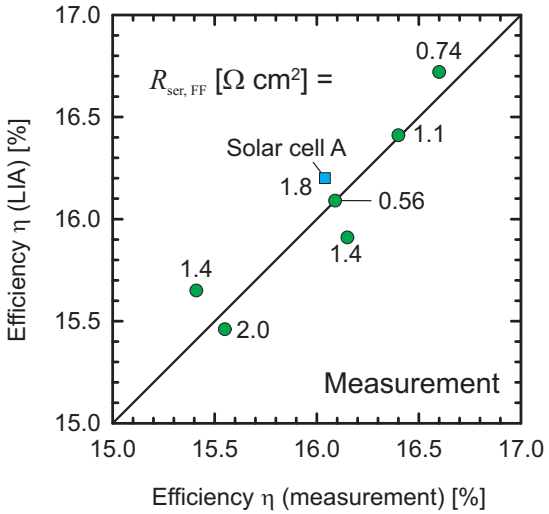

Figure 8.6: *Comparison of efficiencies obtained from the light-IV characteristics to efficiencies calculated using the approach presented in this work. The series resistance image of solar cell A (marked with a blue square) is shown in Fig. 8.2.*

8.4 Measurements

To demonstrate the applicability of LIA for the analysis of series resistance images of silicon solar cells I carry out different measurements in this section.

8.4.1 LIA for monocrystalline silicon solar cells

I analyze seven monocrystalline silicon solar cells which suffer from locally high series resistances. To apply the LIA application schema I carry out light-IV, J_{sc}-V_{oc} and PL-Rs measurements[16] and compare the solar cell efficiency which follows directly from measurement to the efficiency which follows from LIA.

The result of this comparison is shown in Fig. 8.6. For the investigated solar cells the measured efficiencies are in good agreement to the values obtained with LIA, even for high series resistances.

8.4.2 LIA applied to solar cell A

I apply the LIA application schema on solar cell A, which was already introduced in Fig. 8.1 and in Fig. 8.2. I extract the LIA IV characteristics, compare resulting efficiencies to the measured efficiencies and demonstrate the virtual modification of the series resistance image.

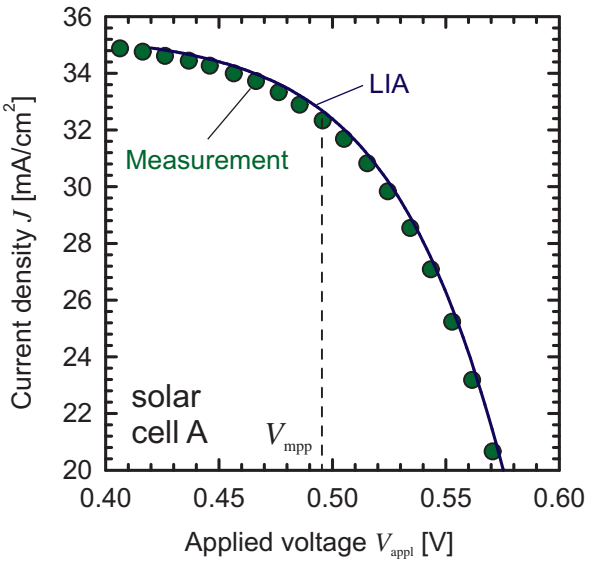

Figure 8.7: *Light-IV characteristics of solar cell A and of LIA. For the LIA calculations a series resistance mapping and as global parameters* J_{ph}, J_{01}, J_{02} *and* R_{sh} *are used.*

IV characteristics

The measured IV characteristics and the IV characteristics obtained from LIA of solar cell A is shown in Fig. 8.7. Both curves are in good agreement. For this solar cell, LIA results in a more realistic IV characteristics than the two-diode model, which was shown in Fig. 8.1.

As a result of LIA an efficiency of $16.18\ \%$ is obtained which is in good agreement to the measured value of $16.04\ \%$.

Virtual manipulation

I virtually manipulate the series resistance mapping to a value of $0.7\ \Omega\mathrm{cm}^2$, as shown in Fig. 8.8, and feed the data again into LIA. Due to the virtual manipulation a total power loss reduction of $0.27\ \mathrm{mW/cm}^2$ is obtained and a new efficiency of $16.2\ \%$.

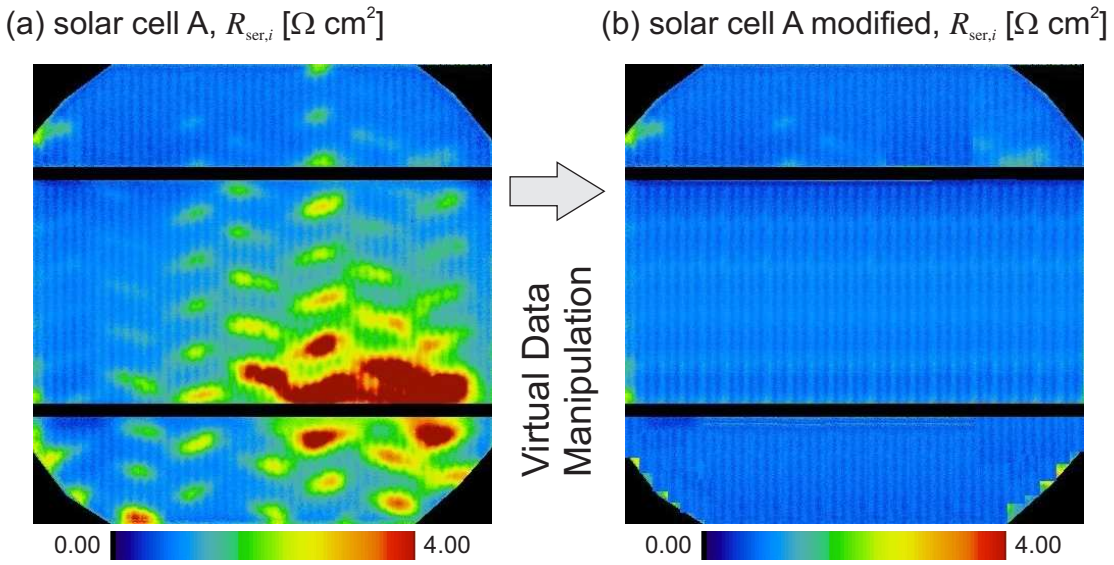

Figure 8.8: *Original (a) and virtually modified (b) data of the series resistance mapping. The data of (b) is fed into LIA again. It thus determines the impact of the high local series resistance to total power loss reduction of 0.27* $\mathrm{mW/cm^2}$.

8.5 Discussion

The presented simulations and experiments demonstrate the applicability of LIA, where the focus laid on industrial monocrystalline silicon solar cells suffering from high local series resistances. For these solar cells, specific process induced faults might be inhomogeneous contact firing, as shown in the example, or broken fingers, which are usually introduced by a broken screen within the screen-printing process of the front-side grid.

8.5.1 Limitations

LIA does not hold for any parameter ranges and for any solar cell structures. In this work, I only analyzed high local series resistances. Similar simulations as presented here has to be carried out to demonstrate the applicability of LIA if different solar cell types, failures, or measurements are involved. In principle, it is possible to simulate with LIA the whole IV characteristics of the solar cell. But due to injection dependences, most of the determined parameters are not correct for each voltage. To get a reliable information about the power losses at the maximum power point, all measurements have to be determined at this voltage.

8.5.2 Rule of thumb

The independent diode model interprets each local inhomogeneity as a separate region with a proprietary IV characteristics. The impact of a local inhomogeneity onto the global solar cell efficiency doesn't depend on the severity of the local parameter only but also of the corresponding region size. As a rule of thumb, one might split the solar cell into two regions A and B, where region A covers a fraction of f and region B a fraction of $1 - f$. Thus, the resulting IV characteristics is

$$J_{\mathrm{total}}(V_{\mathrm{appl}}) = f \cdot J_{\mathrm{A}}(V_{\mathrm{appl}}) + (1 - f) \cdot J_{\mathrm{B}}(V_{\mathrm{appl}}), \tag{8.5}$$

where $J_{\mathrm{A}}(V_{\mathrm{appl}})$ and $J_{\mathrm{B}}(V_{\mathrm{appl}})$ are the IV characteristics of each region, respectively.

8.5.3 Outlook

Possible extensions are the usage of mappings of the effective diffusion length, as obtained by spectrally resolved light beam induced current[121] (SR-LBIC), mappings of the saturation current densities, as obtained by the coupled determination of the dark saturation current and the series resistance[20] (C-DCR), and shunt resistance images, as obtained by dark lock-in thermography[122] (DLIT). In principle, the saturation current density of the emitter and of the second diode can be fed into LIA as local parameters as well. However, until now, no methods have been introduced to determine reliable parameter mappings of these parameters.

8.5.4 Median value of parameter mappings

For solar cell operation, a median value for any parameter variation is usually well sought after. This median value should describe the inhomogeneous parameter of the solar cell with just one

global parameter, which gives the same result on a homogeneous cell. The presented approach in this work demonstrates easily with Eq. (8.2) that such a global median value exists only for $J_{\mathrm{sc},i}$ at I_{sc} conditions:

$$J_{\mathrm{sc}} = \sum_i J_{\mathrm{sc},i}. \tag{8.6}$$

For all other parameters a global median value does not exist as no parameter scales linearly with I. Even often applied rules of thumb $R_{\mathrm{sh}}^{-1} = \sum_i R_{\mathrm{sh},i}^{-1}$ or $J_{0\mathrm{b}} = \sum_i J_{0\mathrm{b},i}$ and thus $L_{\mathrm{eff}}^{-1} = \sum_i L_{\mathrm{eff},i}^{-1}$ do *not* hold in general.

8.6 Short summary

In this chapter, I proposed a simple local impact analysis to calculate the impact of local parameters onto the global solar cell efficiency. Measured parameter mappings can be fed into this approach easily and computation time is fairly low. LIA is based on the independent diode model which was verified for solar cells with high local series resistances by means of simulations and experiment. Parameter mappings can be virtually manipulated to determine the impact of specific local regions onto the global energy conversion efficiency.

APPENDIX A

Parameters of the used optical model

For the final result of the luminescence photon emission probability [see Eq. (5.24)], I used an optical model, which was originally developed for the absorption of impinging light by Brendel et al. in Ref. 70. In the following, I will explain in more detail the different parameters and whose determination using measured reflectance data as examplarily shown in Fig. A.2. More details are also given in Ref. 70. Figure A.1 shows a scheme of the optical model.

- T_1 is the transmittance of a light ray passing the base under an angle θ_1:

$$T_1 = \exp\left(-\alpha\, W/\cos\theta_1\right). \tag{A.1}$$

- T_2 similarily follows to

$$T_2 = \exp\left(-\alpha\, W/\cos\theta_2\right). \tag{A.2}$$

- R_f is assumed to equal the measured reflectance for strong absorption ($\alpha^{-1} \ll W$) and is extrapolated for weak absorption ($\alpha^{-1} > W$).

- θ_1 is determined by the geometry of the surface. For a chemically textured (100)-oriented silicon, an angle of $41.8°$ follows for a wavelength of $900\ \mathrm{nm}$.[69]

- R_b1 and R_bn are assumed equal as a first approximation: $R_\mathrm{b1} = R_\mathrm{bn} = R_\mathrm{b}$.

- R_b is a weighted average reflectance of the specularly and diffusely reflecting rear surface, R_bs and R_bd:

$$R_\mathrm{b} = (1-\Lambda)\, R_\mathrm{bs} + \Lambda\, R_\mathrm{bd}, \tag{A.3}$$

  where Λ is the weighting-factor.

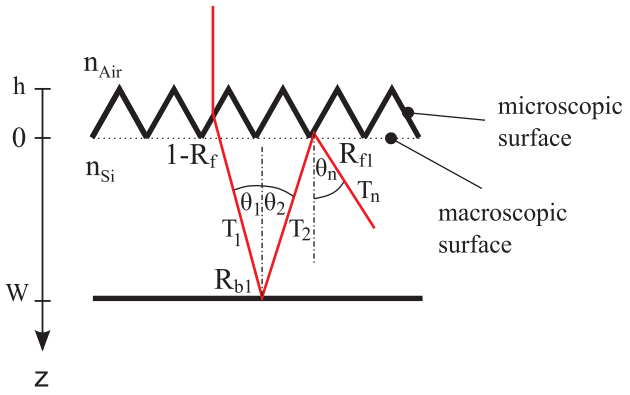

Figure A.1: *Parameters of the optical model used for the luminescence photon emission probability in Eq.* (5.24).

- R_{bs} and R_{bd} are assumed equal as a first approximation: $R_{\mathrm{bs}} = R_{\mathrm{bd}} = R_{\mathrm{b}}$.
- θ_2 follows as the solution of Eq. (A.2) with

$$T_2 = \frac{\Lambda\, R_{\mathrm{bd}}\, T_n + (1-\Lambda)\, R_{\mathrm{bs}}\, T_{2,\mathrm{s}}}{\Lambda\, R_{\mathrm{bd}} + (1-\Lambda)\, R_{\mathrm{bs}}}, \tag{A.4}$$

  where

$$T_{2,\mathrm{s}} = \exp\left(-\alpha\, W/\cos\theta_1\right). \tag{A.5}$$

- T_n is given by

$$T_n = \exp\left(-\alpha\, W\right) \cdot (1-\alpha\, W) + (\alpha\, W)^2 \cdot E_1(\alpha\, W), \tag{A.6}$$

  where

$$E_1(z) = \int_z^\infty dt\, t^{-1}\, \exp(-t) \tag{A.7}$$

  is the exponential integral function. With T_n given by Eq. (A.6), the angle θ_n follows as the solution of

$$T_n = \exp\left(-\alpha\, W/\cos\theta_n\right). \tag{A.8}$$

  θ_n becomes $60°$ for long-wavelength light ($\alpha \to 0$), as also calculated by Campbell and Green,[123] who described the absorption properties of pyramidally textured surfaces.

- R_{fn} was determined by Brendel et al.[70] using a raytracing simulation at a wavelength of 1000 nm:

$$R_{\mathrm{fn}} = 0.928 \pm 0.001. \tag{A.9}$$

  It is assumed to be independent of wavelength.

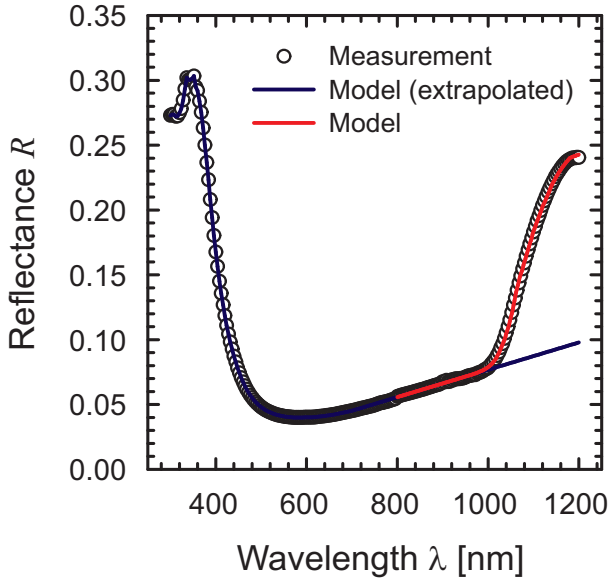

Figure A.2: *Measured reflectance (data) and model (line) of Eq.* (A.12) *fitted to the data.*

- R_{f1} is calculated using

$$R_{\mathrm{f1}} = \frac{\Lambda\, R_{\mathrm{bd}}\, T_n\, R_{\mathrm{fn}} + (1-\Lambda)\, R_{\mathrm{bs}}\, T_{2,\mathrm{s}}\, R_{\mathrm{fs}}}{\Lambda\, R_{\mathrm{bd}}\, T_n + (1-\Lambda)\, R_{\mathrm{bs}}\, T_{2,\mathrm{s}}}, \tag{A.10}$$

  where

$$R_{\mathrm{fs}} = 0.62 \tag{A.11}$$

  was determined using raytracing simulations.[70]

The remaining parameters Λ and R_{b} are determined by a least-square fit to the measured reflectance of[69]

$$R = 1 - (1 - R_{\mathrm{f}}) \left[1 - T_1\, R_{\mathrm{b1}}\, T_2\, (1 - R_{\mathrm{f1}}) - \frac{T_1\, R_{\mathrm{b1}}\, T_2\, R_{\mathrm{f1}}\, R_{\mathrm{bn}}\, (1 - R_{\mathrm{fn}})\, T_n^2}{1 - R_{\mathrm{bn}}\, R_{\mathrm{fn}}\, T_n^2} \right]. \tag{A.12}$$

Fig. A.2 shows exemplarily a measured reflectance spectrum of a silicon solar cell and the model of Eq. (A.12) fitted to the measured data.

APPENDIX B

Optical reciprocity theorem

B.1 Luminescence photon emission probability for EL

The luminescence photon emission probability can also be obtained for the case of electroluminescence using the optical reciprocity theorem

$$\phi_{\mathrm{EL}}(\lambda,\phi,\theta) = Q_{\mathrm{EQE}}(\lambda,\phi,\theta)\,\phi_{\mathrm{bb}}(\lambda,\phi,\theta)\,\exp\left(\frac{V_i}{V_{\mathrm{T}}}\right) \tag{B.1}$$

introduced by Rau.[86] This theorem connects the electroluminescence emission ϕ_{EL} per spherical angle with the external quantum efficiency

$$Q_{\mathrm{EQE}}(\lambda,\phi,\theta) = \int dz\, g_{\mathrm{eh}}(z,\lambda,\phi,\theta)\, f_{\mathrm{c}}(z), \tag{B.2}$$

where f_{c} is the collection efficiency. ϕ_{EL} and Q_{EQE} as defined in Eq. (B.1) send (ϕ_{EL}) and receive (Q_{EQE}) photons from and into the direction given by ϕ and θ.

In the following, f_{c} in Eq. (B.2) is expressed using Donolato's theorem[87]

$$f_{\mathrm{c}}(z) = \frac{\Delta n_{\mathrm{drk}}(z)}{n_1}, \tag{B.3}$$

which connects the collection efficiency to the normalized dark carrier distribution Δn_{drk}. In the latter equation,

$$n_1 = \frac{n_{\mathrm{i}}^2}{N_{\mathrm{A}}} \cdot \exp\left(\frac{V_i}{V_{\mathrm{T}}}\right) \tag{B.4}$$

is the minority carrier concentration at the beginning of the base, with the base dopant concentration N_{A}, the local voltage V_i and the thermal voltage V_{T}.

Rau's reciprocity theorem [see Eq. (B.1)] holds, if the emission of luminescence goes into the solid angle (with respect to ϕ and θ) of illumination for the quantum efficiency case. In an experiment, the detector collects photons from a certain solid angle Ω, as shown for example in Fig. 5.1. The measurable photon flux then follows by integrating Eq. (B.1),

$$\begin{aligned}\varphi(\lambda)\,d\lambda &= d\lambda \int d\Omega\,\phi_{\mathrm{EL}}(\lambda,\phi,\theta) \\ &= d\lambda\,\Omega\,Q_{\mathrm{EQE}}(\lambda)\,\phi_{\mathrm{bb}}(\lambda)\,\exp\left(\frac{V_i}{V_{\mathrm{T}}}\right).\end{aligned} \tag{B.5}$$

Again a solid angle $\Omega \ll 4\pi$ was assumed since the electroluminescence emission ϕ_{EL} depends in general on the direction of emission.[81]

I apply Rau's reciprocity theorem by inserting Eq. (B.2) into Eq. (B.5) and obtain

$$\varphi(\lambda)\,d\lambda = d\lambda\,\Omega\,\phi_{\mathrm{bb}}\,\frac{N_{\mathrm{A}}}{n_{\mathrm{i}}^2}\int dz\,g_{\mathrm{eh}}(z,\lambda)\,\Delta n_{\mathrm{drk}}. \tag{B.6}$$

Comparing the result of Eq. (B.6) to Eq. (3.10),[a]

$$\varphi(\lambda)\,d\lambda = d\lambda\,\phi_{\mathrm{bb}}\int dz\,f_{\mathrm{out}}\,4\pi\,\frac{n_{\mathrm{Si}}^2}{n_{\mathrm{i}}^2}\,\alpha\,\Delta n_{\mathrm{drk}}\,N_{\mathrm{A}}, \tag{B.7}$$

I obtain

$$f_{\mathrm{out}}(z,\lambda) = \frac{\Omega}{4\pi\,n_{\mathrm{Si}}^2}\cdot\frac{g_{\mathrm{eh}}(z,\lambda)}{\alpha}, \tag{B.8}$$

which is the same result as already deduced in Eq. (5.24).

B.2 Reciprocity of EL and QE: Experimental demonstration

To demonstrate the relationship of Φ_{EL} and Q_{EQE}, I measure the electroluminescence spectrum $\Phi_{\mathrm{EL,meas}}$ and the external quantum efficiency Q_{EQE} of a monocrystalline silicon solar cell. Consequently, the measured $\Phi_{\mathrm{EL,meas}}(\lambda)$ data is transformed using Eq. (B.1) into an external quantum efficiency Q_{EL}. However, as already described in Eq. (6.7), the EL measurement is not calibrated,

$$\Phi_{\mathrm{EL,meas}} = C_{\mathrm{opt}}\cdot\Phi_{\mathrm{EL}}, \tag{B.9}$$

and determines only relative values. I thus vary C_{opt} until a good overlap of Q_{EQE} and Q_{EL} is achieved in the wavelength range from $1050\ \mathrm{nm}$ to $1170\ \mathrm{nm}$.

Figure B.1 shows the resulting Q_{EQE} and Q_{EL} for this solar cell. For a wide wavelength-range a good qualitative overlap is achieved. For wavelengths shorter than $1060\ \mathrm{nm}$ the measurement of the EL spectrum becomes too noisy, which also occurs for quantum efficiency measurements at wavelengths larger than $1150\ \mathrm{nm}$. Both measurements thus complement one another: While the quantum efficiency measurement gives the quantum efficiency with high accuracy for wavelengths shorter than $1050\ \mathrm{nm}$, EL is much more sensitive for larger wavelengths.

[a] I used $p = N_{\mathrm{A}}$, $n = \Delta n_{\mathrm{drk}}$, $C_{\mathrm{eh}} = 1$ and b_{low} as given in Eq. (3.8).

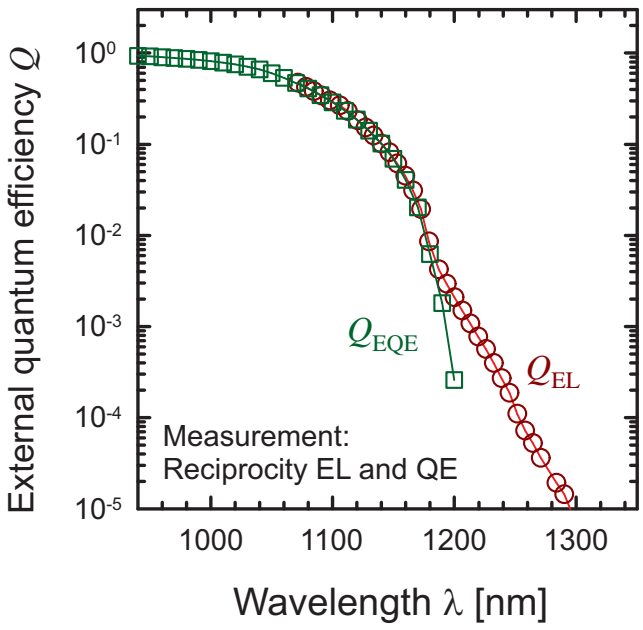

Figure B.1: *Reciprocity between electroluminescence and quantum efficiency.*

Bibliography

[1] I. Uchida: *Observation of the recombination radiation from silicon p-n junction*. Japanese Journal of Applied Physics, 2(9):561–564, 1963. http://dx.doi.org/10.1143/JJAP.2.561. 1

[2] K. Penner: *Electroluminescence from silicon devices -a tool for device and material characterization-*. Journal de Physique, 49(9):C4–797–C4–800, 1988. http://dx.doi.org/10.1051/jphyscol:19884167. 1

[3] G. Livescu, M. Angell, and J. Filipe: *A real-time photoluminescence imaging system*. Journal of Electronic Materials, 19(9):937–942, 1990. http://dx.doi.org/10.1007/BF02652919. 1

[4] T. Fuyuki, H. Kondo, Y. Kaji, T. Yamazaki, Y. Takahashi, and Y. Uraoka: *One shot mapping of minority carrier diffusion length in polycrystalline silicon solar cells using electroluminescence*. In *Proceedings of the 31st Photovoltaic Specialists Conference, Lake Buena Vista, FL*, pages 1343–1345. IEEE, New York, 2005. 1

[5] T. Trupke, R.A. Bardos, M.D. Abbott, F.W. Chen, J.E. Cotter, and A. Lorenz: *Fast photoluminescence imaging of silicon wafers*. In *Proceedings of the 4th World Conference on Photovoltaic Energy Conversion, Waikoloa, Hawaii*, pages 928–931. IEEE, New York, 2006. http://dx.doi.org/10.1109/WCPEC.2006.279608. 1, 14

[6] M.D. Abbott, J.E. Cotter, F.W. Chen, T. Trupke, R.A. Bardos, and K.C. Fisher: *Application of photoluminescence characterization to the development and manufacturing of high-efficiency silicon solar cells*. Journal of Applied Physics, 100:114514, 2006. http://dx.doi.org/10.1109/WCPEC.2006.279399. 1

[7] K. Bothe, P. Pohl, J. Schmidt, T. Weber, P. Altermatt, B. Fischer, and R. Brendel: *Electroluminescence imaging as an in-line characterisation tool for solar cell production*. In *Proceedings of the 21st European Photovoltaic Solar Energy Conference, Dresden, Germany*, pages 597–600. WIP, Munich, 2006. 1, 30, 83

[8] T. Fuyuki, Y. Kaji, A. Ogane, and Y. Takahashi: *Analtic findings in the photographic characterization of crystalline silicon solar cells using electroluminescence*. In *Proceedings of the 4th World Conference on Photovoltaic Energy Conversion, Waikoloa, Hawaii*, volume 1, pages 905–907. IEEE, New York, 2006. http://dx.doi.org/10.1109/WCPEC.2006.279602. 1

[9] T. Fuyuki, H. Kondo, Y. Kaji, A. Ogane, and Y. Takahashi: *Analytic findings in the electroluminescence characterization of crystalline silicon solar cells*. Journal of Applied Physics, 101:023711, 2007. http://dx.doi.org/10.1063/1.2431075. 1

[10] Y. Takahashi, Y. Kaji, A. Ogane, Y. Uraoka, and T. Fuyuki: *-"luminoscopy"-novel tool for the diagnosis of crystalline silicon solar cells and modules utilizing electroluminescence*. In *Proceedings of the 4th World Conference on Photovoltaic Energy Conversion, Waikoloa, Hawaii*, volume 1, pages 924–927. IEEE, New York, 2006. http://dx.doi.org/10.1109/WCPEC.2006.279607. 1

[11] Y. Takahashi, H. Kondo, T. Yamazaki, Y. Uraoka, and T. Fuyuki: *Novel characterization of rear surface passivation effect in thin monocrystalline silicon solar cells by photographic surveying*. In *Proceedings of the 31st Photovoltaic Specialists Conference, Lake Buena Vista, FL*, pages 1349–1352. IEEE, New York, 2005. 1

[12] Y. Augarten, M.D. Abbott, T. Trupke, R. Bardos, H.P. Hartmann, R. Gupta, J. Bauer, and O. Breitenstein: *Detection and isolation of localised shunts in industrial silicon solar cells using pl imaging*. In *Proceedings of the 22nd European Photovoltaic Solar Energy Conference, Milan, Italy*, pages 1220–1223. WIP, Munich, 2007. 1

[13] O. Breitenstein, J. Bauer, T. Trupke, and R.A. Bardos: *On the detection of shunts in silicon solar cells by photo- and electroluminescence imaging*. Progress in Photovoltaics: Research and Applications, 16:325–330, 2008. http://dx.doi.org/10.1002/pip.803. 1

[14] M. Kasemann, W. Kwapil, M.C. Schubert, H. Habenicht, B. Walter, M. The, S. Kontermann, S. Rein, O. Breitenstein, J. Bauer, A. Lotnyk, B. Michl, H. Nagel, A. Schütt, J. Carstensen, H. Föll, T. Trupke, Y. Augarten, H. Kampwerth, R.A. Bardos, S. Pingel, J. Berghold, W. Warta, and S.W. Glunz: *Spatially resolved silicon solar cell characterization using infrared imaging methods*. In *Proceedings of the 33rd Photovoltaic Specialists Conference, San Diego, CA*. IEEE, New York, 2008. http://link.aip.org/link/?APL/89/224102/1. 1

[15] M. Glatthaar, J. Haunschild, R. Zeidler, M. Demant, J. Greulich, B. Michl, W. Warta, S. Rein, and R. Preu: *Evaluating luminescence based voltage images of silicon solar cells*. Journal of Applied Physics, 108:014501, 2010. http://dx.doi.org/10.1063/1.3443438. 1, 70, 77, 83, 85, 100

[16] T. Trupke, E. Pink, R.A. Bardos, and M.D. Abbott: *Spatially resolved series resistance of silicon solar cells obtained from luminescence imaging*. Applied Physics Letters,

90:093506, 2007. http://dx.doi.org/10.1063/1.2709630. 1, 14, 43, 70, 83, 85, 89, 92, 100, 105, 111

[17] K. Ramspeck, K. Bothe, D. Hinken, B. Fischer, J. Schmidt, and R. Brendel: *Recombination current and series resistance imaging of solar cells by combined luminescence and lock-in thermography*. Applied Physics Letters, 90:153502, 2007. http://dx.doi.org/10.1063/1.2721138. 89

[18] D. Hinken, K. Ramspeck, K. Bothe, B. Fischer, and R. Brendel: *Series resistance imaging of solar cells by voltage dependent electroluminescence*. Applied Physics Letters, 91:182104, 2007. http://dx.doi.org/10.1063/1.2804562. 100

[19] H. Kampwerth, T. Trupke, J. W. Weber, and Y. Augarten: *Advanced luminescence based effective series resistance imaging of silicon solar cells*. Applied Physics Letters, 93(20):202102, 2008. http://link.aip.org/link/?APL/93/202102/1. 92, 100

[20] M. Glatthaar, J. Haunschild, M. Kasemann, J. Giesecke, W. Warta, and S. Rein: *Spatially resolved determination of dark saturation current and series resistance of silicon solar cells*. Physica Status Solidi (RRL), 4(1):13–15, 2010. http://dx.doi.org/10.1002/pssr.200903290. 1, 83, 92, 100, 105, 114

[21] P. Würfel, T. Trupke, T. Puzzer, E. Schaffer, W. Warta, and S.W. Glunz: *Diffusion lengths of silicon solar cells from luminescence images*. Journal of Applied Physics, 101(12):123110, 2007. http://link.aip.org/link/?JAP/101/123110/1. 1, 54, 68

[22] K. Bothe, D. Hinken, K. Ramspeck, B. Fischer, and R. Brendel: *Combined quantitative analysis of electroluminescence images and lbic mappings*. In *Proceedings of the 22nd European Photovoltaic Solar Energy Conference, Milan, Italy*, pages 1673–1677. WIP, Munich, 2007. 69

[23] A. Helbig, T. Kirchartz, and U. Rau: *Quantitative information of electroluminescence images*. In *Proceedings of the 23rd European Photovoltaic Solar Energy Conference, Valencia, Spain*, pages 426–429. WIP, Munich, 2008. http://dx.doi.org/10.4229/23rdEUPVSEC2008-1CV.1.59. 68

[24] J.A. Giesecke, M. Kasemann, and W. Warta: *Determination of local minority carrier diffusion lengths in crystalline silicon from luminescence images*. Journal of Applied Physics, 106:014907, 2009. http://dx.doi.org/10.1002/pip.868. 2, 68

[25] D. Hinken, K. Bothe, K. Ramspeck, S. Herlufsen, and R. Brendel: *Determination of the effective diffusion length of silicon solar cells from photoluminescence*. Journal of Applied Physics, 105(10):104516, 2009. http://link.aip.org/link/?JAP/105/104516/1. 1

[26] D. Hinken, K. Bothe, K. Ramspeck, S. Herlufsen, and R. Brendel: *Determination of the emitter saturation current density of silicon solar cells using photoluminescence and*

quantum efficiency analysis. In *Proceedings of the 24th European Photovoltaic Solar Energy Conference, Hamburg, Germany*, pages 1082–1085. WIP Munich, September 2009. http://dx.doi.org/10.4229/24thEUPVSEC2009-2CO.3.5. 1

[27] M. Kasemann, D. Grote, B. Walter, W. Kwapil, T. Trupke, Y. Augarten, R.A. Bardos, E. Pink, M.D. Abbott, and W. Warta: *Luminescence imaging for the detection of shunts on silicon solar cells*. Progress in Photovoltaics: Research and Applications, 16(16):297–305, 2008. http://dx.doi.org/10.1002/pip.812. 1

[28] Y. Augarten, T. Trupke, M. Lenio, J. Bauer, O. Breitenstein, J. Weber, and R.A. Bardos: *Luminescence shunt imaging: Qualitative and quantitative shunt images using photoluminescence imaging*. In *Proceedings of the 24th European Photovoltaic Solar Energy Conference, Hamburg, Germany*, pages 27–31. WIP, Munich, 2009. http://dx.doi.org/10.4229/24thEUPVSEC2009-1AO.4.2. 1

[29] M. Bail, J. Kentsch, R. Brendel, and M. Schulz: *Lifetime mapping of si wafers by an infrared camera*. In *Proceedings of the 28th IEEE Photovoltaic Specialists Conference, Anchorage, AK*, pages 99–103. IEEE, New York, 2000. http://dx.doi.org/10.1109/PVSC.2000.915763. 2

[30] M. The, M.C. Schubert, and W. Warta: *Quantitative lifetime measurements with photoluminescence imaging*. In *Proceedings of the 22nd European Photovoltaic Solar Energy Conference, Milan, Italy*, pages 354–359. WIP, Munich, 2007. 2

[31] T. Trupke, R.A. Bardos, M.C. Schubert, and W. Warta: *Photoluminescence imaging of silicon wafers*. Applied Physics Letters, 89(4):044107, 2006. http://link.aip.org/link/?APL/89/044107/1. 2, 5

[32] T. Trupke, R.A. Bardos, and M.D. Abbott: *Self-consistent calibration of photoluminescence and photoconductance lifetime measurements*. Applied Physics Letters, 87(18):184102, 2005. http://link.aip.org/link/?APL/87/184102/1. 2

[33] R. Sinton and A. Cuevas: *Contactless determination of current–voltage characteristics and minority-carrier lifetimes in semiconductors from quasi-steady-state photoconductance data*. Applied Physics Letters, 69(17):2510, 1996. http://dx.doi.org/10.1063/1.117723. 2

[34] D. Macdonald, J. Tan, and T. Trupke: *Imaging interstitial iron concentrations in boron-doped crystalline silicon using photoluminescence*. Journal of Applied Physics, 103:073710, 2008. http://dx.doi.org/10.1063/1.2903895. 2

[35] T. Trupke and R.A. Bardos: *Photoluminescence characterization of silicon wafers and silicon solar cells*. In *Proceedings of the 18th Workshop on Crystalline Silicon Solar Cells & Modules, Vail, USA*. NREL, Golden, 2008.

[36] S. Herlufsen, J. Schmidt, D. Hinken, K. Bothe, and R. Brendel: *Photoconductance-calibrated photoluminescence lifetime imaging of crystalline silicon*. Physica Status Solidi

(RRL), 1–3:245–247, 2008. http://dx.doi.org/10.1002/pssr.200802192. 2, 14, 16

[37] S. Herlufsen, K. Ramspeck, D. Hinken, A. Schmidt, J. Müller, K. Bothe, J. Schmidt, and R. Brendel: *Dynamic lifetime imaging based on photoluminescence measurements*. In *Proceedings of the 25th European Photovoltaic Solar Energy Conference, Valencia, Spain*, pages 2369–2373. WIP Munich, September 2010. http://dx.doi.org/10.4229/25thEUPVSEC2010-2CV.3.84. 2

[38] D. Kiliani, G. Micard, B. Raabe, and G. Hahn: *Time resolved photoluminescence imaging for carrier lifetime mapping of silicon wafers*. In *Proceedings of the 25th European Photovoltaic Solar Energy Conference, Valencia, Spain*, pages 1363–1366. WIP Munich, September 2010. http://dx.doi.org/10.4229/25thEUPVSEC2010-2CO.4.2.

[39] S. Herlufsen, K. Ramspeck, D. Hinken, A. Schmidt, J. Müller, K. Bothe, J. Schmidt, and R. Brendel: *Dynamic photoluminescence lifetime imaging for the characterisation of silicon wafers*. Physica Status Solidi (RRL), 5(1):25–27, 2011. http://dx.doi.org/10.1002/pssr.201004426. 2

[40] T. Trupke, R.A. Bardos, M.D. Abbott, and J.E. Cotter: *Suns-photoluminescence: Contactless determination of current-voltage characteristics of silicon wafers*. Applied Physics Letters, 87(9):093503, 2005. http://link.aip.org/link/?APL/87/093503/1. 5

[41] J.A. Giesecke, M. The, M. Kasemann, and W. Warta: *Spatially resolved characterization of silicon as-cut wafers with photoluminescence imaging*. Progress in Photovoltaics: Research and Applications, 17(4):217–225, 2008. http://dx.doi.org/10.1002/pip.868. 5

[42] K. Bothe, K. Ramspeck, D. Hinken, C. Schinke, J. Schmidt, S. Herlufsen, R. Brendel, J. Bauer, J. M. Wagner, N. Zakharov, and O. Breitenstein: *Luminescence emission from forward- and reverse-biased multicrystalline silicon solar cells*. Journal of Applied Physics, 106(10):104510–1–104510–8, 2009. http://dx.doi.org/10.1063/1.3256199. 8

[43] J. Giesecke, M. Kasemann, M.C. Schubert, B. Michl, M. The, W. Warta, and P. Würfel: *Determination of minority carrier diffusion lengths in silicon solar cells from photoluminescence images*. In *Proceedings of the 23th European Photovoltaic Solar Energy Conference, Valencia, Spain*, pages 453–457. WIP Munich, September 2008. http://dx.doi.org/10.4229/23rdEUPVSEC2008-1CV.2.4. 11

[44] K.S. Bindra, R. Chari, V. Shukla, A. Singh, S. Ida, and S.M. Oak: *Two-photon absorption and nonlinear refraction in commercial colour glass filters*. Journal of Optics A: Pure and Applied Optics, 1:73–76, 1999. http://dx.doi.org/10.1088/1464-4258/1/1/010. 11

[45] M.D. Abbott, R.A. Bardos, T. Trupke, K.C. Fisher, and E. Pink: *The effect of diffusion-limited lifetime on implied current voltage curves based on photoluminescence data*. Journal of Applied Physics, 102:044502, 2007. http://dx.doi.org/10.1063/1.2756529. 14

[46] M. Seibt, R. Khalil, V. Kveder, and W. Schröter: *Electronic states at dislocations and metal silicide precipitates in crystalline silicon and their role in solar cell materials*. Applied Physics A, 96:235–253, 2009. http://dx.doi.org/10.1007/s00339-008-5027-8. 16

[47] J.R. Janesick: *Scientific charge-coupled devices*, volume PM83. SPIE–Society of Photo-Optical Instrumentation Engineering, 2001, ISBN 978-0819436986. 17

[48] J. Hynecek and T. Nishiwaki: *Excess noise and other important characteristics of low light level imaging using charge multiplying ccds*. IEEE Transactions on Electron Devices, 50(1):239–245, January 2003, ISSN 0018-9383. http://dx.doi.org/10.1109/TED.2002.806962. 18

[49] M.S. Robbins and B.J. Hadwen: *The noise performance of electron multiplying charge-coupled devices*. IEEE Transactions on Electron Devices, 50(5):1227–1232, May 2003, ISSN 0018-9383. http://dx.doi.org/10.1109/TED.2003.813462. 18

[50] P.P. Altermatt, F. Geelhaar, T. Trupke, X. Dai, A. Neisser, and E. Daub: *Injection dependence of spontaneous radiative recombination in crystalline silicon: Experimental verification and theoretical analysis*. Applied Physics Letters, 88:261901–261901–3, 2006. http://dx.doi.org/10.1063/1.2218041. 25, 29, 31

[51] van W. Roosbroeck and W. Shockley: *Photon-radiative recombination of electrons and holes in germanium*. Physical Review, 94:1558–1560, June 1954. http://link.aps.org/doi/10.1103/PhysRev.94.1558. 25, 56, 57

[52] P. Würfel: *The chemical potential of radiation*. Journal of Physics C: Solid State Physics, 15:3967–3985, 1982. http://dx.doi.org/10.1088/0022-3719/15/18/012. 26, 56

[53] M. Planck: *Vorlesungen über die Theorie der Wärmestrahlung*. Leipzig, 1906. http://books.google.com/books?id=RDlWAAAAMAAJ. 26

[54] M.A. Green and M. Keevers: *Optical properties of intrinsic silicon at 300 k*. Progress in Photovoltaics, 3(3):189–192, 1995. http://dx.doi.org/10.1002/pip.4670030303. 27

[55] M.A. Green: *Silicon Solar Cells, Advanced Principles & Practice*. Centre for Photovoltaic Devices and Systems, University of New South Wales, Sydney, N. S. W. 2052, 1995, ISBN 0733409946. 27, 43, 66, 94

[56] A. Wolf: *Sintered Porous Silicon - Physical Properties and Applications for Layer-Transfer Silicon Thin-Film Solar Cells*. PhD thesis, Leibniz Universität Hannover, Germany, 2007. 27

[57] M. J. Keevers and M. A. Green: *Absorption edge of silicon from solar cell spectral response measurements*. Applied Physics Letters, 66(2):174–176, 1995. http://link.aip.org/link/?APL/66/174/1. 27, 28

[58] G.G. MacFarlane, T.P. MacLean, J.E. Quarrington, and V. Roberts: *Fine structure in the absorption-edge spectrum of si*. Physical Review, 111:1245–1254, 1958. http://dx.doi.org/10.1103/PhysRev.111.1245.

[59] R. Corkish and M.A. Green: *Band edge optical absorption in intrinsic silicon: Assessment of the indirect transition and disorder models*. Journal of Applied Physics, 73:3988, 1993. http://dx.doi.org/10.1063/1.352864. 27

[60] T. Trupke, M.A. Green, P. Würfel, P.P. Altermatt, A. Wang, J. Zhao, and R. Corkish: *Temperature dependence of the radiative recombination coefficient of intrinsic crystalline silicon*. Journal of Applied Physics, 94(8):4930–4937, October 2003. http://dx.doi.org/10.1063/1.1610231. 29

[61] H. Schlangenotto, H. Maeder, and W. Gerlach: *Temperature dependence of the radiative recombination coefficient in silicon*. Physica Status Solidi (RRL), A21:357–367, 1974. http://dx.doi.org/10.1002/pssa.2210210140. 29

[62] Y.P. Varshni: *Band-to-band radiative recombination in groups iv, vi, and iii-v semiconductors (i)*. Phys. Stat. Sol., 19:459–514, 1967.

[63] W. Michaelis and M.H. Pilkuhn: *Radiative recombination in silicon*. Physica Status Solidi (a), 36:311–319, 1969.

[64] M. Ruff, M. Fick, R. Lindner, U. Rössler, and R. Helbig: *The spectral distribution of the intrinsic radiative recombination in silicon*. Journal of Applied Physics, 74(1):267–274, 1993. http://link.aip.org/link/?JAP/74/267/1. 29

[65] P.P. Altermatt, F. Geelhaar, T. Trupke, X. Dai, A. Neisser, and E. Daub: *Injection dependence of spontaneous radiative recombination in c-si: experiment, theoretical analysis, and simulation*. In *Proceedings of the 5th International Conference on Numerical Simulation of Optoelectronic Devices, 2005. NUSOD '05*, pages 47 – 48, sept. 2005. 29

[66] R. Brendel: *Sunrays: A versatile ray tracing program for the photovoltaic community*. In *Proceedings of the 12th European Photovoltaic Solar Energy Conference, Amsterdam*, volume II, pages 1339–1342. H.S. Stephens & Associates, April 1994. 30

[67] J.E. Cotter: *Raysim 6.0 - a free geometrical ray tracing program for silicon solar cells*. In *Proceedings of the 31st Photovoltaic Specialists Conference, Lake Buena Vista, FL*, pages 1165–1168. IEEE, New York, 2005. 30

[68] W. Shockley: *The theory of p-n junctions in semiconductors and p-n junction transistors*. Bell System Technical Journal, 28:435–489, 1949. 35, 84

[69] P.A. Basore: *Extended spectral analysis of internal quantum efficiency*. In *Proceedings of the 23rd Photovoltaic Specialists Conference, Louisville, KY*, pages 147–152. IEEE, New York, 1993. http://dx.doi.org/10.1109/PVSC.1993.347063. 38, 41, 66, 69, 77, 117, 119

[70] R. Brendel, M. Hirsch, R. Plieninger, and J.H. Werner: *Quantum efficiency analysis of thin-layer silicon solar cells with back surface fields and optical confinement*. IEEE Transactions on Electron Devices, 43(7):1104–1113, 1996. http://dx.doi.org/10.1109/16.502422. 38, 39, 56, 57, 58, 59, 117, 118, 119

[71] R. Brendel and U. Rau: *Effective diffusion lengths for minority carriers in solar cells as determined from internal quantum efficiency analysis*. Journal of Applied Physics, 85(7):3634–3637, 1999. http://dx.doi.org/10.1063/1.369726. 41

[72] D.A. Clugston and P.A. Basore: *Pc1d version 5: 32-bit solar cell modeling on personal computers*. In *Proceedings of the 26th Photovoltaic Specialists Conference, Anaheim, CA*, pages 207–210. IEEE, New York, 1997. http://dx.doi.org/10.1109/PVSC.1997.654065. 41, 44

[73] F.A. Lindholm, J.G. Fossum, and E.L. Burgess: *Application of the superposition principle to solar-cell analysis*. IEEE Transactions on Electron Devices, 26(3):165–171, March 1979, ISSN 0018-9383. http://dx.doi.org/10.1109/T-ED.1979.19400. 42, 62, 79

[74] N.G. Tarr and D.L. Pulfrey: *An investigation of dark current and photocurrent superposition in photovoltaic devices*. Solid-State Electronics, 22(3):265–270, 1979, ISSN 0038-1101. http://www.sciencedirect.com/science/article/B6TY5-46VC216-DR/2/94fd02594f214780939428f221efac9d. 79

[75] S. J. Robinson, A. G. Aberle, and M. A. Green: *Departures from the principle of superposition in silicon solar cells*. Journal of Applied Physics, 76(12):7920–7930, 1994. http://link.aip.org/link/?JAP/76/7920/1. 42, 62, 79

[76] R. Duggan and G.B. Scott: *The efficiency of photoluminescence of thin epitaxial semiconductors*. Journal of Applied Physics, 52(1):407–411, 1981. http://dx.doi.org/10.1063/1.328464. 42

[77] M. Bass and Optical Society of America: *Handbook of Optics: Fundamentals, techniques, and design*. Number Bd. 1 in *Handbook of Optics*. McGraw-Hill, 1995, ISBN 9780070477407. 49

[78] J. Chaves: *Introduction to Nonimaging Optics*. CRC Press, 2008, ISBN 9781420054293. 49

[79] B. Edlén: *The refractive index of air*. Metrologia, 2(2):71–80, 1966. 49

[80] P.E. Ciddor: *Refractive index of air: new equations for the visible and near infrared*. Appl. Opt., 35(9):1566–1573, Mar 1996. http://ao.osa.org/abstract.cfm?URI=ao-35-9-1566. 49

[81] K. Schick, E. Daub, S. Finkbeiner, and P. Würfel: *Verification of a generalized planck law for luminescence radiation from silicon solar cells*. Applied Physics A, 54:109–114, 1992. http://dx.doi.org/10.1007/BF00323895. 54, 122

[82] R. Brüggemann: *Kirchhoff's generalised law applied to amorphous silicon/crystalline silicon heterostructures*. Philosophical Magazine, 89(28–30):2519–2529, 2009. http://dx.doi.org/10.1080/14786430903074805. 54

[83] T. Kirchartz, A. Helbig, and U. Rau: *Note on the interpretation of electroluminescence images using their spectral information*. Solar Energy Materials and Solar Cells, 92:1621–1627, 2008. http://dx.doi.org/10.1016/j.solmat.2008.07.013. 56, 57, 68

[84] G. Kirchhoff: *Ueber das verhältniss zwischen dem emissionsvermögen und dem absorptionsvermögen der körper für wärme und licht*. Annalen der Physik, 185(2):275–301, 1860, ISSN 1521-3889. http://dx.doi.org/10.1002/andp.18601850205. 56

[85] T. Kirchartz. Private communication, September 2011. 56

[86] U. Rau: *Reciprocity relation between photovoltaic quantum efficiency and electroluminescent emission of solar cells*. Physical Review B, 76:025303, 2007. http://dx.doi.org/10.1103/PhysRevB.76.085303. 56, 57, 66, 77, 121

[87] C. Donolato: *A reciprocity theorem for charge collection*. Applied Physics Letters, 46(3):270–272, 1985. http://link.aip.org/link/?APL/46/270/1. 56, 121

[88] J.A. Giesecke, M. Kasemann, M.C. Schubert, P. Würfel, and W. Warta: *Separation of local bulk and surface recombination in crystalline silicon from luminescence reabsorption*. Progress in Photovoltaics: Research and Applications, 18(1):10–19, 2009. http://dx.doi.org/10.1002/pip.927. 68

[89] R. Brendel and U. Rau: *Injection and collection diffusion lengths of polycrystalline thin film solar cells*. Solid State Phenomena, 67–68:81–86, 1999. http://dx.doi.org/10.4028/www.scientific.net/SSP.67-68.81. 69

[90] C. Schinke, D. Hinken, K. Bothe, C. Ulzhöfer, A. Milsted, J. Schmidt, and R. Brendel: *Determination of the collection diffusion length by electroluminescence imaging*. In *Energy Procedia 8*, volume 8, pages 147–152. Elsevier, 2011. http://dx.doi.org/10.1016/j.egypro.2011.06.116. 69

[91] T. Fuyuki, H. Kondo, T. Yamazaki, Y. Takahashi, and Y. Uraoka: *Photographic surveying of minority carrier diffusion length in polycrystalline silicon solar cells by electroluminescence*. Applied Physics Letters, 86(26):262108–262108–3, 2005. http://dx.doi.org/10.1063/1.1978979. 77, 100

[92] J. Haunschild, M. Glatthaar, M. Kasemann, S. Rein, and E.R. Weber: *Fast series resistance imaging for silicon solar cells using electroluminescence*. Physica Status Solidi (RRL), 3(7–8):227–229, 2009. http://dx.doi.org/10.1002/pssr.200903175. 77, 83, 100

[93] O. Breitenstein, A. Khanna, Y. Augarten, J. Bauer, J.M. Wagner, and K. Iwig: *Quantitative evaluation of electroluminescence images of solar cells*. Physica Status Solidi (RRL), 4(1):7–9, 2010. http://dx.doi.org/10.1002/pssr.200903304. 77, 92, 100

[94] M. Glatthaar, J. Haunschild, R. Zeidler, J. Rentsch, S. Rein, O. Breitenstein, D. Hinken, and K. Bothe: *Luminescence imaging for quantitative solar cell material and process characterization*. In *Proceedings of the 25th European Photovoltaic Solar Energy Conference, Valencia, Spain*, pages 1825–1827. WIP Munich, September 2010. http://dx.doi.org/10.4229/25thEUPVSEC2010-2CV.2.34. 77

[95] N.D. Arora, S.G. Chamberlain, and D.J. Roulston: *Diffusion length determination in p-n junction diodes and solar cells*. Applied Physics Letters, 37:325–327, 1980. http://dx.doi.org/10.1063/1.91891. 77

[96] A. Metz and R. Hezel: *Record efficiencies above 21% for mis-contacted diffused junctionsilicon solar cells*. In *Proceedings of the 26th Photovoltaic Specialists Conference, Anaheim, CA*, pages 283–286. IEEE, New York, 1997. http://dx.doi.org/10.1109/PVSC.1997.654084. 79

[97] T. Trupke, R.A. Bardos, M.D. Abbott, P. Würfel, E. Pink, Y. Augarten, F.W. Chen, K. Fisher, J.E. Cotter, M. Kasemann, M. Rüdiger, S. Kontermann, M.C. Schubert, M. The, S.W. Glunz, W. Warta, D. Macdonald, J. Tan, A. Cuevas, J. Bauer, R. Gupta, O. Breitenstein, T. Buonassisi, G. Tarnowski, A. Lorenz, H.P. Hartmann, D.H. Neuhaus, and J.M. Fernandez: *Progress with luminescence imaging for the characterisation of silicon wafers and solar cells*. In *Proceedings of the 22nd European Photovoltaic Solar Energy Conference, Milan, Italy*, pages 22–31, 2007. 83

[98] A.S.H. van der Heide, J.H. Bultman, J. Hoornstra, and A. Schönecker: *Error diagnosis and optimisation of c-si solar cell processing using contact resistances determined with the corescanner*. Solar Energy Materials and Solar Cells, 74:43–50, 2002. http://dx.doi.org/10.1016/S0927-0248(02)00046-6. 83

[99] J. Carstensen, G. Popkirov, J. Bahr, and H. Föll: *Cello: an advanced lbic measurement technique for solar cell local characterization*. Solar Energy Materials and Solar Cells, 76(4):599–611, 2003. http://dx.doi.org/10.1016/S0927-0248(02)00270-2. 83, 105

[100] U. Rau and M. Schmidt: *Electronic properties of zno/cds/cu(in,ga) se2 solar cells - aspects of heterojunction formation*. Thin Solid Films, 387:141–146, 2001. http://dx.doi.org/10.1016/S0040-6090(00)01737-5. 83, 86, 89

[101] V. G. Karpov, A. D. Compaan, and Diana Shvydka: *Effects of nonuniformity in thin-film photovoltaics*. Applied Physics Letters, 80(22):4256–4258, 2002. http://link.aip.org/link/?APL/80/4256/1.

[102] P.O. Grabitz, U. Rau, and J.H. Werner: *A multi-diode model for spatially inhomogeneous solar cells*. Thin Solid Films, 487(1-2):14–18, September 2005. http://dx.doi.org/10.1016/j.tsf.2005.01.027. 89

[103] P.O. Grabitz, U. Rau, and J.H. Werner: *Modeling of spatially inhomogeneous solar cells by a multi-diode approach*. Physica Status Solidi (a), 202, No. 15:2920—2927, 2005. http://dx.doi.org/10.1002/pssa.200521205. 83, 86, 89

[104] K. Ramspeck, K. Bothe, D. Hinken, J. Schmidt, and R. Brendel: *Recombination current and series resistance imaging of multicrystalline silicon solar cells*. In *Proceedings of the 17th International Photovoltaic Science and Engineering Conference, Fukuoka, Japan*, page 265, 2007. 85

[105] Goetzberger: *Sonnenenergie: Photovoltaik*. B. G. Teubner, 1994, ISBN 0471971448. 86, 87, 89, 103

[106] G. Heiser, P. Altermatt, and J. Litsios: *Combining 2d and 3d device simulation with circuit simulation for optimising high-efficiency silicon solar cells*. Simulation of Semiconductor Devices and Processes, 6:348–351, 1995. 86

[107] C.T. Sah, R.N. Noyce, and W. Shockley: *Carrier generation and recombination in p-n junctions and p-n junction characteristics*. Proceedings of the IRE, 45(9):1228–1243, September 1957, ISSN 0096-8390. http://dx.doi.org/10.1109/JRPROC.1957.278528. 86

[108] Peter Würfel: *Physik der Solarzelle*, volume 2. Spektrum Akademischer Verlag, 2000. 86

[109] B. Fischer: *Loss Analysis of Crystalline Silicon Solar Cells using Photoconductance and Quantum Efficiency Measurements*. PhD thesis, University of Konstanz, 2003. 86

[110] G.L. Araujo, A.C. Cuevas, and J.M. Ruiz: *The effect of distributed series resistance on the dark and illuminated current-voltage characteristics of solar cells*. IEEE Transactions on Electron Devices, ED-33(3):391–401, 1986. http://dx.doi.org/10.1109/T-ED.1986.22500. 89

[111] J. Carstensen, A. Schütt, and H. Föll: *Cello local solar cell resistance maps: Modeling of data and correlation to solar cell efficiency*. In *Proceedings of the 22nd European Photovoltaic Solar Energy Conference, Milan, Italy*, pages 337–340. WIP Munich, 2007. 89

[112] J. Dicker, J. Isenberg, and W. Warta: *Effect of shunt distribution on the overall solar cell performance investigated by circuit simulation*. In *Proceedings of the 17th European Photovoltaic Solar Energy Conference*, pages 1567–1570. WIP Munich, 2001. 89

[113] J.M. Rabaey: *The spice home page*. EECS Department of the University of California at Berkeley, 2010. http://bwrc.eecs.berkeley.edu/classes/icbook/spice/. 89, 93

[114] Paolo Nenzi: *Ngspice circuit simulator*, 2010. http://ngspice.sourceforge.net/. 89, 93

[115] D. Grote, M. Kasemann, M. Hermle, and W. Warta: *Analysing lateral inhomogeneities of silicon solar cells using a quasi 3d circuit simulation tool based on spice*. In *Proceedings of the 22nd European Photovoltaic Solar Energy Conference, Milan, Italy*, pages 305–310, 2007. 93

[116] B. Michl, M. Kasemann, J. Giesecke, M. Glatthaar, A. Schütt, J. Carstensen, H. Föll, S. Rein, W. Warta, and H. Nagel: *Application of luminescence imaging based series resistance measurement methods in an industrial environment*. In *Proceedings of the 23rd European Photovoltaic Solar Energy Conference, Valencia, Spain*, pages 1176–1182. WIP, Munich, 2008. 93, 100

[117] A.G. Aberle, S.R. Wenham, and M.A. Green: *A new method for accurate measurements of the lumped series resistance of solar cells*. In *Proceedings of the 23rd Photovoltaic Specialists Conference, Louisville, KY*, pages 133–139. IEEE, New York, 1993. http://dx.doi.org/10.1109/PVSC.1993.347065. 94

[118] M. Wolf and H. Rauschenbach: *Series resistance effects on solar cell measurements*. Advanced Energy Conversion, 3:455–479, 1963. http://dx.doi.org/10.1016/0365-1789(63)90063-8. 103

[119] M.A. Green: *Solar Cells, Operating Principles, Technology and System Applications*. The University of New South Wales, 1998. 103

[120] O. Kunz, R. Brüggemann, A.B. Sproul, and A.G. Aberle: *Determination of the two-diode model parameters of non-ideal solar cells*. In *Proceedings of the 20th European Photovoltaic Solar Energy Conference, Barcelona, Spain*. WIP Munich, June 2005. 103

[121] W. Warta, J. Sutter, B.F. Wagner, and R. Schindler: *Impact of diffusion length distribution on the performance of mc-silicon solar cells*. In *Proceedings of the 2nd World Conference and Exhibition on Photovoltaic Solar Energy Conversion, Vienna, Austria*, pages 1650–1653. EC Joint Research Center, Ispra, 1998. 105, 114

[122] O. Breitenstein, J.P. Rakotoniaina, M.H. Al Rifai, and M. Werner: *Shunt types in crystalline silicon solar cells*. Progress in Photovoltaics: Research and Applications, 12:529–538, 2004. http://dx.doi.org/10.1002/pip.544. 105, 114

[123] P. Campbell and M.A. Green: *Light trapping properties of pyramidally textured surfaces*. Journal of Applied Physics, 62:243, 1987. http://dx.doi.org/10.1063/1.339189. 118

Symbols and acronyms

Latin Letters

SNR . .	Signal-to-noise ratio, see Eq. (2.7)	
A_1 . . .	Area of volume element one, see Fig. 5.1	cm^2
A_2 . . .	Area of volume element two, see Fig. 5.1	cm^2
A_{cell} . .	Area of the solar cell	cm^2
A_{loc} . .	Area of one local element	cm^2
A_E . . .	Surface element of luminescence photon emission, see Fig. 5.1	cm^2
A_i . . .	Area of volume element i, see Fig. 5.1	cm^2
B_{low} . .	Integral (in terms of wavelength) coefficient of radiative recombination obtained at low carrier densities, see Eq. (3.3)	$\mathrm{cm}^3\mathrm{s}^{-1}$
b_{low} . .	Spectral (in terms of wavelength) coefficient of radiative recombination obtained at low carrier densities, see Eq. (3.3)	$\mathrm{cm}^2\mathrm{s}^{-1}$
B_{rad} . .	Integral (in terms of wavelength) coefficient of radiative recombination at an arbitrary carrier density, see Eq. (3.2)	$\mathrm{cm}^3\mathrm{s}^{-1}$
c_0 . . .	Velocity of light in vacuum	$\mathrm{m/s}$
C_{conv} . .	Camera conversion factor from generated electron-hole pairs in the pixel to digital units or counts	counts/eh
C_{eh} . .	Coulomb enhancement factor of radiative recombination, see Eq. (3.2)	
C_i . . .	Calibration constant for the local junction voltage determination from luminescence imaging, see Eq. (7.7)	$\mathrm{counts/s}$

$C_{i,\mathrm{EL}}$ . .	Calibration constant for the local junction voltage determination from electroluminescence images, see Eq. (7.10)	$\mathrm{counts/s}$
$C_{i,\mathrm{PL}}$ . .	Calibration constant for the local junction voltage determination from photoluminescence images, see Eq. (7.9)	$\mathrm{counts/s}$
D . . .	Diffusion constant, see Eq. (4.5)	$\mathrm{cm^2 s^{-1}}$
E_{Fn} . .	Quasi-Fermi level of the electrons, see Eq. (7.2)	eV
E_{Fp} . .	Quasi-Fermi level of the holes, see Eq. (7.2)	eV
f_{c} . . .	Collection efficiency of the solar cell base, see Eq. (B.3)	
$f_{\mathrm{out,lg}}$.	One-dimensional luminescence photon emission probability for long-wavelength photons, see Eq. (6.9)	
$f_{\mathrm{out,sh}}$.	One-dimensional luminescence photon emission probability for short-wavelength photons, see Eq. (6.16)	
f_{out} . .	One-dimensional luminescence photon emission probability, see Sec. 5.1.1	
G_{eh} . .	One-dimensional generation rate of excess charge carriers, see Eq. (4.6)	$\mathrm{cm^{-3} s^{-1}}$
g_{eh} . . .	Normalized, one-dimensional generation profile of excess charge carriers, see Eq. (4.6)	$\mathrm{cm^{-1}}$
G_{ph} . .	Integral (in terms of wavelength) generation rate of luminescence photons, see Eq. (3.1)	$\mathrm{cm^{-3} s^{-1}}$
g_{ph} . . .	Generation rate density of luminescence photons of wavelength λ, see Eq. (3.4)	$\mathrm{cm^{-4} s^{-1}}$
$g_{\mathrm{eh},1}$ . .	Normalized, one-dimensional generation profile of excess charge carriers of the first impinging photon pass, see Eq. (4.17)	$\mathrm{cm^{-1}}$
I	Current which is extracted from or fed into the solar cell at the terminals	A
I_{sc} . . .	Short-circuit current of the solar cell	A
$I_{\mathrm{extr},i,0}$.	Current used to develop the dependence of the local voltage drop from the extracted local current in a taylor series, see Eq. (7.21)	mA
$I_{\mathrm{extr},i}$.	Current which is extracted from the local element i, see Eq. (7.11)	mA
$I_{\mathrm{loss},i}$ . .	Current which is extracted from the local element i but consequently lost in any another element due to the interaction of all local elements, see Eq. (7.13)	mA
$I_{\mathrm{ph},i}$ . .	Photo-current of the local element i, see Eq. (7.11)	mA

$I_{\mathrm{rec},i}$ . .	Recombination current of the local element i, see Eq. (7.11)	mA
$I_{\mathrm{term},i}$.	Current of a local element i, which is extracted at the terminals, see Eq. (7.13)	mA
J_{01} . . .	Saturation current density of the first diode	$\mathrm{fAcm^{-2}}$
J_{02} . . .	Saturation current density of the second diode	$\mathrm{fAcm^{-2}}$
$J_{0\mathrm{b}}$ . . .	Base saturation current density	$\mathrm{fAcm^{-2}}$
$J_{0\mathrm{e}}$ . . .	Emitter saturation current density	$\mathrm{fAcm^{-2}}$
J_0 . . .	Saturation current density	$\mathrm{fAcm^{-2}}$
J_{sc} . . .	Short circuit current density of the solar cell	$\mathrm{mAcm^{-2}}$
J_i . . .	Current density of the local element i, see Eq. (6.28)	$\mathrm{mAcm^{-2}}$
$J_{01,i}$ . .	Saturation current density of the first diode at the local element i	$\mathrm{fAcm^{-2}}$
$J_{02,i}$ . .	Saturation current density of the second diode at the local element i	$\mathrm{fAcm^{-2}}$
$J_{0\mathrm{b},i}$ . .	Base saturation current density of the local element i	$\mathrm{fAcm^{-2}}$
$J_{0,i}$ . .	Total saturation current density of the local element i	$\mathrm{fAcm^{-2}}$
J_{cpij} . .	Local current density within the j-th current path of the i-th local element, see Eq. (7.17)	$\mathrm{mAcm^{-2}}$
$J_{\mathrm{ph},i}$ . .	Photo current density of the local element i, see Eq. (7.12)	$\mathrm{mAcm^{-2}}$
J_{ph} . .	Photo current density of the solar cell	$\mathrm{mAcm^{-2}}$
$J_{\mathrm{sc},i}$ . .	Short circuit current density of the local element i, see Eq. (8.6)	$\mathrm{mAcm^{-2}}$
L_α . . .	Absorption length of light in silicon	$\mu\mathrm{m}$
L_b . . .	Diffusion length of minority charge carriers within the bulk of the solar cell, see Eq. (4.5)	$\mu\mathrm{m}$
L_C . . .	Collection length of the solar cell base, see Eq. (6.11)	$\mu\mathrm{m}$
L_{eff} . .	Effective diffusion length of the solar cell base, see Eq. (4.19)	$\mu\mathrm{m}$
$L_{\mathrm{eff},i}$ . .	Local effective diffusion length of the local element i of the solar cell	$\mu\mathrm{m}$
n . . .	Total excess electron concentration, see Eq (3.12)	$\mathrm{cm^{-3}}$
n_0 . . .	Thermically generated excess electron concentration, see Eq (3.12)	$\mathrm{cm^{-3}}$
n_1 . . .	Total excess electron concentration at the beginning of the base, see Eq. (4.8)	$\mathrm{cm^{-3}}$
n_{Air} . .	Refractive index of air	

N_A . . .	Dopant concentration of the acceptors	cm^{-3}
N_drk . .	Number of dark electrons generated within one pixel, see Eq. (2.10)	
N_FW . .	Full-well capacity of the camera's pixels, see Eq. (2.16)	
n_i . . .	Intrinsic carrier concentration, $8.3 \times 10^9\ \mathrm{cm}^{-3}$ at 25 °C	cm^{-3}
n_i^2 . . .	Square of intrinsic carrier concentration	cm^{-6}
N_ph . .	Number of photons which enter one pixel of the camera, see Eq. (2.8)	
n_Si . . .	Refractive index of silicon	
N_s . . .	Number of signal electrons generated within one pixel, see Eq. (2.9)	
$N_{\mathrm{s},i}$ . .	Number of signal electrons within one pixel of measurement i, see Eq. (2.4)	
p. . . .	Total excess hole concentration, see Eq (3.12)	cm^{-3}
p_0 . . .	Thermically generated excess hole concentration, see Eq (3.12)	cm^{-3}
P_max . .	Maximum output power of the solar cell	W
Q_cam . .	Spectral quantum efficiency of the detector (i. e. the camera).	
Q_EL . .	External quantum efficiency calculated from an EL spectrum, see Sec. B.2	
Q_EQE .	External quantum efficiency, see Sec. B.2	
R_b1 . .	Internal reflectance at the rear surface at the first internal hit, see Eq. (4.15)	
R_bd . .	Internal diffuse rear reflectance, see Eq. (A.3)	
R_bn . .	Internal reflectance at the rear surface for the second and all subsequent hits, see Eq. (4.15)	
R_bs . .	Internal specular rear reflectance, see Eq. (A.3)	
R_b . . .	Internal rear surface reflectance, is a weighted average of the specular back reflectance R_bs of flat regions and the diffuse reflectance R_rd of the rough back surface, see Eq. (A.3)	
R_f1 . . .	Internal reflectance of the front surface at the first internal hit, see Eq. (4.15)	
R_fn . .	Internal reflectance of the front surface at the second and all subsequent hits, see Eq. (4.15)	
R_fs . . .	Internal specular reflectance of the front surface	

R_f . . .	Direct reflectance of the outer front surface, see Sec. A	
r_ph . . .	Distance travelled by a photon	$\mu\mathrm{m}$
R_rad . .	Radiative recombination rate, see Eq. (3.1)	$\mathrm{cm}^{-3}\mathrm{s}^{-1}$
R_rd . .	Internal reflectance of diffuse light at the rear surface, see Eq. (A.3)	
$R_\mathrm{ser,FF}$.	Series resistance of the solar cell which represents the power losses in the fillfactor compared to the pseudo-fillfactor	$\Omega\mathrm{cm}^2$
R_ser . .	Global series resistance of the solar cell	$\Omega\mathrm{cm}^2$
R_sh . .	Shunt resistance of the solar cell	$\Omega\mathrm{cm}^2$
$R_{\mathrm{abs},i}$.	Absolute local series resistance of the i-th element, see Eq. (7.23)	$\Omega\mathrm{cm}^2$
R_cpij . .	Ohmic resistance along the j-th current path of the i-th element, see Eq. (7.14)	$\Omega\mathrm{cm}$
$R_{\mathrm{diff},i}$.	Differential local series resistance of the i-th element, see Eq. (7.24)	$\Omega\mathrm{cm}^2$
$R_{\mathrm{ser},i}$ . .	Local effective series resistance of the local element i of the solar cell	$\Omega\mathrm{cm}^2$
$R_{\mathrm{sh},i}$ . .	Local shunt resistance of the local element i of the solar cell	$\Omega\mathrm{cm}^2$
S_eff . .	Effective surface recombination velocity lumping all parasitic current losses into one value which acts at the beginning of the base, see Eq. (4.10)	$\mathrm{cm/s}$
S_em . .	Effective emitter surface recombination velocity which follows from the emitter saturation current density	$\mathrm{cm/s}$
S_front . .	Surface recombination velocity at the front of the solar cell	$\mathrm{cm/s}$
S_rear . .	Surface recombination velocity at the rear of the solar cell	$\mathrm{cm/s}$
T_1 . . .	Transmittance through the bulk at the first photon pass, see Eq. (A.1)	
T_2 . . .	Transmittance through the bulk at the second photon pass, see Eq. (A.2)	
t_exp . .	Exposure time of the camera	s
T_optics .	Transmittance of all optics in-between the sample and the detector itself, including filters and lenses.	
$T_\mathrm{2,s}$ . .	Transmittance through the bulk at the second photon pass for specularly reflected light, see Eq. (A.5)	
T_n . . .	Transmittance through the base at the third and all subsequent photon passes, see Eq. (A.6)	

V_{appl} . .	Applied voltage at the solar cell	mV
V_{mpp} . .	Maximum power point voltage of the solar cell	mV
V_{oc} . . .	Open circuit voltage of the solar cell	mV
V_{T} . . .	Thermal voltage, 25.7 mV at 25 $^\circ$	mV
V_{loc} . .	Local voltage, see Eq. (7.2)	mV
$V_{i,\mathrm{EL}}$ . .	Local junction voltage at EL measurements, see Eq. (6.29)	mV
$V_{i,\mathrm{PL}}$ . .	Local junction voltage at PL measurements, see Eq. (6.29)	mV
V_i . . .	Local junction voltage, refers to the junction voltage at the element i of the solar cell, see Eq. (7.6)	mV
W_{b} . . .	Thickness of base region	$\mu\mathrm{m}$
W_{e} . . .	Thickness of emitter region	nm
z	Distance to the front surface	$\mu\mathrm{m}$

GREEK LETTERS

α_{b2b} . .	Absorption coefficient of band-to-band recombination	cm^{-1}
α_{imp} . .	Absorption coefficient in silicon of impinging photons	cm^{-1}
α_{lum} . .	Absorption coefficient in silicon of luminescence photons	cm^{-1}
ΔE_{F} . .	Quasi-Fermi level splitting, see Eq. (7.2)	eV
Δn . . .	Externally generated excess electron concentration, see Eq (3.12)	cm^{-3}
Δn_{drk} .	Externally generated excess electron concentration in the dark, see Eq. (4.18)	cm^{-3}
Δn_{oc} . .	Externally generated excess electron concentration at open-circuit conditions, see Eq. (4.24)	cm^{-3}
Δn_{sc} . .	Externally generated excess electron concentration at short circuit conditions, see Eq. (4.20)	cm^{-3}
Δn_{wp} .	Externally generated excess electron concentration at working-point conditions, see Eq. (4.23)	cm^{-3}
Δp . . .	Externally generated excess hole concentration, see Eq (3.12)	cm^{-3}
ΔV_{cpi} .	Voltage drop between the local and the applied voltage over the current path of the i-th local element, see Eq. (7.14)	mV
Λ . . .	Lambertian factor, an areal fraction Λ of the back surface behaves like an ideal lambertian reflector while a fraction $1-\Lambda$ is ideally flat, see Eq. (A.4)	

λ_{imp} ..	Wavelength of impinging photons	nm
λ_{lum} ..	Wavelength of luminescence photons	nm
ϕ_{bb} ..	Planck's black body photon flux density per volume, time and solid angle, see Eq. (3.7)	$\mathrm{cm^{-3}s^{-1}sr^{-1}}$
Φ_{drk} ..	Thermally generated electron flux of each camera pixel, see Eq. (2.10)	$\mathrm{s^{-1}}$
$\Phi_{\mathrm{EL,lg}}$.	Flux of electrically stimulated long-wavelength luminescence photons (EL) emitted from the sample's front surface, see Eq. (6.10)	$\mathrm{cm^{-2}s^{-1}}$
$\Phi_{\mathrm{EL,sh}}$.	Flux of electrically stimulated short-wavelength luminescence photons (EL) emitted from the sample's front surface, see Eq. (6.17)	$\mathrm{cm^{-2}s^{-1}}$
Φ_{EL} ..	Flux of electrically stimulated luminescence photons (EL) emitted from the sample's front surface	$\mathrm{cm^{-2}s^{-1}}$
ϕ_{EL} ..	Flux per solid angle of electrically stimulated luminescence photons (EL) emitted from the sample's front surface	$\mathrm{cm^{-2}s^{-1}sr^{-1}}$
$\Phi_{\mathrm{imp,0}}$.	Flux of impinging photons at the outer solar cell front surface, see Eq. (4.5)	$\mathrm{cm^{-2}s^{-1}}$
Φ_{imp} ..	One-dimensional photon flux of impinging photons along the z-axis of the sample, see Eq. (5.17)	$\mathrm{cm^{-2}s^{-1}}$
Φ_{lum} ..	Flux of luminescence photons emitted from the sample's surface, see Eq. (3.11)	$\mathrm{cm^{-2}s^{-1}}$
$\Phi_{\mathrm{oc,lg}}$.	Flux of long-wavelength luminescence photons emitted from the sample's front surface at PL-oc conditions, see Eq. (6.15)	$\mathrm{cm^{-2}s^{-1}}$
$\Phi_{\mathrm{oc,sh}}$.	Flux of short-wavelength luminescence photons emitted from the sample's front surface at PL-oc conditions, see Eq. (6.21)	$\mathrm{cm^{-2}s^{-1}}$
Φ_{oc} ..	Flux of luminescence photons emitted from the sample's front surface at PL-oc conditions	$\mathrm{cm^{-2}s^{-1}}$
$\Phi_{\mathrm{sc,lg}}$ ..	Flux of long-wavelength luminescence photons emitted from the sample's front surface at PL-sc conditions, see Eq. (6.12)	$\mathrm{cm^{-2}s^{-1}}$
$\Phi_{\mathrm{sc,sh}}$.	Flux of short-wavelength luminescence photons emitted from the sample's front surface at PL-sc conditions, see Eq. (6.19)	$\mathrm{cm^{-2}s^{-1}}$
Φ_{sc} ...	Flux of luminescence photons emitted from the sample's front surface at PL-sc conditions	$\mathrm{cm^{-2}s^{-1}}$

Φ_{sub} ..	Flux of luminescence photons which results from a subtraction of the fluxes at PL-wp and EL conditions, see Eq. (6.27)	$\mathrm{cm}^{-2}\mathrm{s}^{-1}$
Φ_{s} ...	Signal electron flux of each camera pixel, see Eq. (2.9)	s^{-1}
Φ_{wp} ..	Flux of luminescence photons emitted from the sample's front surface at PL-wp conditions	$\mathrm{cm}^{-2}\mathrm{s}^{-1}$
Φ_i ...	Flux of luminescence photons emitted from the front surface of the local element i	$\mathrm{cm}^{-2}\mathrm{s}^{-1}$
$\Phi_{i,\mathrm{EL}}$ ..	Flux of luminescence photons of the local element i from the sample at short-circuit conditions, see Eq. (7.10)	$\mathrm{cm}^{-2}\mathrm{s}^{-1}$
$\Phi_{i,\mathrm{oc}}$ ..	Flux of luminescence photons of the local element i from the sample at open-circuit conditions, see Eq. (7.9)	$\mathrm{cm}^{-2}\mathrm{s}^{-1}$
$\Phi_{i,\mathrm{sc}}$ ..	Flux of luminescence photons of the local element i from the sample at short-circuit conditions, see Eq. (7.9)	$\mathrm{cm}^{-2}\mathrm{s}^{-1}$
σ_{df} ...	Standard deviation of dark-frame subtracted values, see Eq. (2.11)	
σ_{drk} ..	Standard deviation of the dark electrons, see Eq. (2.10)	
σ_{ro} ...	Standard deviation of the read-out noise, see Eq. (2.11)	
σ_{s} ...	Standard deviation of the signal electrons, see Eq. (2.9)	
σ_{tmp} ..	Standard deviation of temperature fluctuations, see Eq. (2.11)	
θ_1 ...	Angle of photon propagation, first pass for impinging photons, last pass for luminescence photons, see Fig. 5.2	
θ_2 ...	Effective mean angle of specular and diffuse photon propagation, second pass for impinging photons, last but one pass for luminescence photons, see Fig. 5.2	
θ_i ...	i-th angle of photon propagation	
θ_n ...	Effective mean angle of diffusely reflected photon propagation, more than two passes for impinging photons, less than last but two passes for luminescence photons, see Fig. 5.2	
φ ...	Flux of luminescence photons emitted from the sample's surface per wavelength interval, see Eq. (3.10)	$\mathrm{cm}^{-3}\mathrm{s}^{-1}$
$\widehat{\Phi}_{\mathrm{EL}}$ ..	Modified electroluminescence photon flux to demonstrate the relation to the external quantum efficiency, see Eq. (6.23)	$\mathrm{cm}^{-2}\mathrm{s}^{-1}$
$N_{\mathrm{imp},0}$.	Number of impinging photons at the surface element A_E	
N_{imp} ..	Number of impinging photons	

N_{lum} .. Number of luminescence photons

TEXTUAL REPLACEMENTS

γ_{imp} .. Abbreviation for an impinging photon

γ_{lum} .. Abbreviation for a luminescence photon

e^- ... Abbreviation for an electron

J_{sc}-V_{oc} Characteristics consisting of J_{sc} and V_{oc} data pairs obtained at equal illumination intensities

p-n .. Junction of p-type and n-type semiconductors

p^+ ... Abbreviation for a hole

EL .. Electroluminescence

FF ... Fill-factor of the illuminated current-voltage characteristics of the solar cell.

i. e. .. For example

IV ... Current voltage

P-V .. Photovoltaic

PL-oc . Photoluminescence at open-circuit conditions

PL-sc . Photoluminescence at short-circuit conditions

PL-wp . Photoluminescence at working point conditions

PL ... Photoluminescence

QE .. Quantum efficiency

SR-LBIC Spectrally resolved light beam induced current

VECTORS

$\hat{t}_{\mathrm{imp},0}$ .. Direction of impinging photons at the outer front surface, see Eq. (5.11)

$\hat{t}_{\mathrm{imp},N}$. Direction of impinging photons within the N-th pass, see Eq. (5.11)

$\hat{t}_{\mathrm{lum},0}$ .. Normalized vector pointing from the place of generation to the direction the photon is sent into, see Eq. (5.11)

$\hat{t}_{\mathrm{lum},N}$. Direction of luminescence photons after N-th surface hit, see Eq. (5.11)

$\vec{t}_{\mathrm{imp}}$ .. Impinging photon path inside the solar cell or wafer, see Sec. 5.2.1

$\vec{t}_{\mathrm{lum}}$ .. Luminescence photon path inside the solar cell or wafer, see Sec. 5.2.1

List of publications

Publications arising from the work in this thesis:

REFEREED PAPERS AS FIRST AUTHOR

[A1]D. Hinken, C. Schinke, S. Herlufsen, A. Schmidt, K. Bothe, and R. Brendel: *Experimental setup for camera-based measurements of electrically and optically stimulated luminescence of silicon solar cells and wafers*. Review of Scientific Instruments, 82(3):033706–1–033706–9, March 2011. http://link.aip.org/link/?RSI/82/033706.

[A2]D. Hinken, A. Milsted, R. Bock, B. Fischer, K. Bothe, M. Schütze, J. Isenberg, A. Schulze, and M. Wagner: *Determination of the base-dopant concentration of large-area crystalline silicon solar cells*. IEEE Transactions on Electron Devices, 57(11):2831–2837, November 2010, ISSN 0018-9383. http://dx.doi.org/10.1109/TED.2010.2064777.

[A3]D. Hinken, K. Bothe, K. Ramspeck, S. Herlufsen, and R. Brendel: *Determination of the effective diffusion length of silicon solar cells from photoluminescence*. Journal of Applied Physics, 105(10):104516, 2009. http://link.aip.org/link/?JAP/105/104516/1.

[A4]D. Hinken, K. Ramspeck, K. Bothe, B. Fischer, and R. Brendel: *Series resistance imaging of solar cells by voltage dependent electroluminescence*. Applied Physics Letters, 91:182104, 2007. http://dx.doi.org/10.1063/1.2804562.

CONFERENCE PAPERS AS FIRST AUTHOR

[B5]D. Hinken, K. Bothe, and R. Brendel: *Impact of lateral variations on the solar cell efficiency*. In *Proceedings of the 25th European Photovoltaic Solar Energy Conference, Valencia, Spain*, pages 1367–1372. WIP Munich, September 2010. http://dx.doi.org/10.4229/25thEUPVSEC2010-2CO.4.3.

[B6]D. Hinken, A. Milsted, R. Bock, B. Fischer, K. Bothe, M. Wagner, M. Schütze, J. Isenberg, and A. Schulze: *Determination of the base dopant concentration of large area crystalline silicon solar cells*. In *Proceedings of the 25th European Photovoltaic Solar Energy Conference, Valencia, Spain*, pages 2528–2533. WIP Munich, September 2010. http://dx.doi.org/10.4229/25thEUPVSEC2010-2DV.1.30.

[B7]D. Hinken, K. Bothe, K. Ramspeck, S. Herlufsen, and R. Brendel: *Determination of the emitter saturation current density of silicon solar cells using photoluminescence and quantum efficiency analysis*. In *Proceedings of the 24th European Photovoltaic Solar Energy Conference, Hamburg, Germany*, pages 1082–1085. WIP Munich, September 2009. http://dx.doi.org/10.4229/24thEUPVSEC2009-2CO.3.5.

[B8]D. Hinken, K. Ramspeck, K. Bothe, B. Fischer, and R. Brendel: *Series resistance imaging of solar cells by voltage dependent electroluminescence*. In *Proceedings of the 17th International Photovoltaic Science and Engineering Conference, Fukuoka, Japan*, page 263, 2007.

REFEREED PAPERS AS CO-AUTHOR

[C9]O. Breitenstein, J. Bauer, K. Bothe, D. Hinken, J. Müller, W. Kwapil, M.C. Schubert, and W. Warta: *Can luminescence imaging replace lock-in thermography on solar cells?* Journal of Photovoltaics, in press, 2011.

[C10]M. Schütze, D. Hinken, A. Milsted, M. Koentopp, and K. Bothe: *Extended analysis of capacitance-voltage curves for the determination of bulk dopant-concentrations of textured silicon solar cells*. IEEE Transactions on Electron Devices, 58(11):3759–3770, 2011. http://dx.doi.org/10.1109/TED.2011.2164079.

[C11]S. Herlufsen, K. Ramspeck, D. Hinken, A. Schmidt, J. Müller, K. Bothe, J. Schmidt, and R. Brendel: *Dynamic photoluminescence lifetime imaging for the characterisation of silicon wafers*. Physica Status Solidi (RRL), 5(1):25–27, 2011. http://dx.doi.org/10.1002/pssr.201004426.

[C12]T. Potthoff, K. Bothe, U. Eitner, D. Hinken, and M. Köntges: *Detection of the voltage distribution in photovoltaic modules by electroluminescence imaging*. Progress in Photovoltaics: Research and Applications, 18(2):100–106, 2010. http://dx.doi.org/10.1002/pip.941.

[C13]K. Bothe, K. Ramspeck, D. Hinken, C. Schinke, J. Schmidt, S. Herlufsen, R. Brendel, J. Bauer, J. M. Wagner, N. Zakharov, and O. Breitenstein: *Luminescence emission from forward- and reverse-biased multicrystalline silicon solar cells*. Journal of Applied Physics, 106(10):104510–1–104510–8, 2009. http://dx.doi.org/10.1063/1.3256199.

[C14]K. Bothe, K. Ramspeck, D. Hinken, and R. Brendel: *Imaging techniques for the analysis of silicon wafers and solar cells*. ECS Transactions, 16(6):63–78, 2008. http://link.aip.org/link/abstract/ECSTF8/v16/i6/p63/s1.

[C15]S. Herlufsen, J. Schmidt, D. Hinken, K. Bothe, and R. Brendel: *Photoconductance-calibrated photoluminescence lifetime imaging of crystalline silicon*. Physica Status Solidi (RRL), 1–3:245–247, 2008. http://dx.doi.org/10.1002/pssr.200802192.

[C16]K. Ramspeck, K. Bothe, D. Hinken, B. Fischer, J. Schmidt, and R. Brendel: *Recombination current and series resistance imaging of solar cells by combined luminescence and lock-in thermography*. Applied Physics Letters, 90:153502, 2007. http://dx.doi.org/10.1063/1.2721138.

CONFERENCE PAPERS AS CO-AUTHOR

[D17]O. Breitenstein, J. Bauer, K. Bothe, D. Hinken, J. Müller, W. Kwapil, M.C. Schubert, and W. Warta: *Luminescence imaging versus lock-in thermography on solar cells and wafers*. In *Proceedings of the 26th European Photovoltaic Solar Energy Conference*. WIP Munich, 2011.

[D18]O. Breitenstein, J. Bauer, K. Bothe, D. Hinken, J. Müller, W. Kwapil, M.C. Schubert, and W. Warta: *Can luminescence imaging replace lock-in thermography on solar cells?* In *Proceedings of the 37th Photovoltaic Specialists Conference, Seattle, Washington*. IEEE, New York, 2011.

[D19]C. Schinke, D. Hinken, K. Bothe, C. Ulzhöfer, A. Milsted, J. Schmidt, and R. Brendel: *Determination of the collection diffusion length by electroluminescence imaging*. In *Energy Procedia 8*, volume 8, pages 147–152. Elsevier, 2011. http://dx.doi.org/10.1016/j.egypro.2011.06.116.

[D20]M. Glatthaar, J. Haunschild, R. Zeidler, J. Rentsch, S. Rein, O. Breitenstein, D. Hinken, and K. Bothe: *Luminescence imaging for quantitative solar cell material and process characterization*. In *Proceedings of the 25th European Photovoltaic Solar Energy Conference, Valencia, Spain*, pages 1825–1827. WIP Munich, September 2010. http://dx.doi.org/10.4229/25thEUPVSEC2010-2CV.2.34.

[D21]S. Herlufsen, K. Ramspeck, D. Hinken, A. Schmidt, J. Müller, K. Bothe, J. Schmidt, and R. Brendel: *Dynamic lifetime imaging based on photoluminescence measurements*. In *Proceedings of the 25th European Photovoltaic Solar Energy Conference, Valencia, Spain*, pages 2369–2373. WIP Munich, September 2010. http://dx.doi.org/10.4229/25thEUPVSEC2010-2CV.3.84.

[D22]M. Köntges, M. Siebert, D. Hinken, U. Eitner, K. Bothe, and T. Potthof: *Quantitative analysis of pv-modules by electroluminescence images for quality control*. In *Proceedings of the 24th European Photovoltaic Solar Energy Conference, Hamburg, Germany*, pages 3226–3231. WIP Munich, September 2009. http://dx.doi.org/10.4229/24thEUPVSEC2009-4CO.2.3.

[D23]S. Herlufsen, J. Schmidt, D. Hinken, K. Bothe, and R. Brendel: *Camera-based photoluminescence lifetime imaging of crystalline silicon wafers*. In *Proceedings of the 24th European Photovoltaic Solar Energy Conference, Hamburg, Germany*, pages

913–917. WIP Munich, September 2009. http://dx.doi.org/10.4229/24thEUPVSEC2009-2AO.1.3.

[D24]K. Bothe, D. Hinken, K. Ramspeck, S. Herlufsen, J. Schmidt, R. Brendel, J. Bauer, J.M. Wagner, N. Zakharov, and O. Breitenstein: *Imaging and analysis of pre-breakdown sites in multicrystalline silicon solar cells*. In *Proceedings of the 24th European Photovoltaic Solar Energy Conference, Hamburg, Germany*, pages 918–924. WIP Munich, September 2009. http://dx.doi.org/10.4229/24thEUPVSEC2009-2AO.1.4.

[D25]K. Bothe, D. Hinken, K. Ramspeck, B. Fischer, and R. Brendel: *Combined quantitative analysis of electroluminescence images and lbic mappings*. In *Proceedings of the 22nd European Photovoltaic Solar Energy Conference, Milan, Italy*, pages 1673–1677. WIP, Munich, 2007.

[D26]K. Ramspeck, K. Bothe, D. Hinken, J. Schmidt, and R. Brendel: *Recombination current and series resistance imaging of multicrystalline silicon solar cells*. In *Proceedings of the 17th International Photovoltaic Science and Engineering Conference, Fukuoka, Japan*, page 265, 2007.

[D27]K. Bothe, D. Hinken, K. Ramspeck, A. Kitiyanan, and T. Fuyuki: *Temperature-dependent electroluminescence imaging of silicon solar cells*. In *Proceedings of the 17th International Photovoltaic Science and Engineering Conference, Fukuoka, Japan*, page 261, 2007.

Acknowledgment

Ein herzliches Dankeschön an alle, die zum Gelingen dieser Arbeit beigetragen haben:

Prof. Dr. Rolf Brendel für die Möglichkeit am ISFH meine Dissertation durchführen zu können, für seine wertvollen Anregungen während der Erstellung und dem Freiraum beim Ausgestalten dieser Arbeit;

Prof. Dr. Jörg Osten für die bereitwillige Übernahme des Korreferats;

Dr. Karsten Bothe für die gute wissenschaftliche Betreuung während meiner Arbeit am ISFH;

Carsten Schinke für die gute Arbeit als Diplomand und für die vielen Diskussionen bezüglich der optischen Modelle;

Sandra Herlufsen und Jens Müller für die vielen Diskussionen und der guten Büro-Atmosphäre;

Arne Schmidt und Martin Wolf für wertvolle Hilfen beim Aufbau der Messplätze;

allen Mitarbeitern des ISFH für das sehr angenehme und freundliche Arbeitsklima und die zahllosen Tipps und Anregungen.

CURRICULUM VITAE

DAVID HINKEN

PERSÖNLICHE DATEN

David Hinken
Hauptstr. 53
30457 Hannover
Deutschland

Verheiratet, deutsch
Geboren am 27. November 1981 in Hannover

STUDIUM

09/2007	*Diplom Physik*, Leibniz Universität Hannover
09/2005–03/2006	Fortsetzung des Studiums in Spanien (Erasmus-Programm), Facultad de Física, Universidad de La Laguna (ULL)
10/2002	Beginn des Studiums der Physik (Diplom), Leibniz Universität Hannover

ANSTELLUNG

seit 08/2007	Wissenschaftlicher Mitarbeiter, Charakterisierung von Solarzellen, Institut für Solarenergieforschung (ISFH)

ERSATZDIENST

07/2001–04/2002	Johanneshof Wettbergen, Hannover

SCHULBILDUNG

07/1994–06/2001	Gymnasium Humboldtschule, Hannover/Linden
07/1992–06/1994	Orientierungsstufe Martensplatz, Hannover/Ricklingen
07/1988–06/1992	Grundschule, Hannover/Wettbergen
07/1987–06/1988	Vorschule, Hannover/Wettbergen